JRC Scientific and Technical Reports

Uncertainties and covariances for inelastic scattering data

A status report

A. Plompen, A. Negret, editors

EUR 25208 EN - 2011

JRC
EUROPEAN COMMISSION

Institute for Reference Materials and Measurements

The mission of the JRC-IRMM is to promote a common and reliable European measurement system in support of EU policies.

European Commission
Joint Research Centre
Institute for Reference Materials and Measurements

Contact information
Address: A. Plompen, Retieseweg 111, 2440 Geel, Belgium
E-mail: Arjan.Plompen@ec.europa.eu
Tel.: +31-14-571381
Fax:

http://irmm.jrc.ec.europa.eu/
http://www.jrc.ec.europa.eu/

JRC 68708

EUR 25208 EN
ISBN 978-92-79-23072-1
ISSN 1831-9424
doi:10.2787/58803

Luxembourg: Publications Office of the European Union, 2011

Uncertainties and covariances for inelastic scattering data

A status report

Contents

1. Summary

In the present report we collect several contributions concerning the correctness, uncertainties and covariances of data obtained with the Germanium Array for Inelastic Neutron Scattering (GAINS) which is installed at the GELINA neutron time-of-flight facility. Both inelastic scattering cross sections [1] and uncertainties and covariances for nuclear data [2] are of great current interest as they feature prominently in uncertainty estimates for key parameters of reactor systems [3]. It is for this reason that a task of the European Collaborative Project Accurate Nuclear Data for nuclear Energy Sustainability (ANDES [4]) is devoted to uncertainties and covariances of inelastic scattering data obtained with GAINS. This report is written in evidence of a milestone (M1.6) of that project. It also provides evidence for a deliverable (6.04) of the work programme 2011 of Action 51402 Nuclear data for radioactive waste management and safety of new reactor developments (ND MINWASTE) of the JRC-IRMM [5].

Inelastic scattering cross sections using the so-called (n,n'g)-technique are obtained using two different measurement setups at IRMM. The first, GAINS, is located at 200 m from the GELINA neutron source and optimizes the resolution of the incident neutron energy for studies of structural materials and coolants. Today it consists of 12 high purity coaxial germanium (HPGe) detectors with a nominal crystal size of 8 cm diameter and 8 cm length. The method of data taking and the expressions used in the data analysis were published [6], as were a number of data sets obtained with the array and its predecessors [7-10]. The second setup, GRAPHEME, was built by a team from CNRS/IN2P3/IPHC (Institut Pluridisciplinair Hubert Currien) and is located at 30 m from the GELINA neutron source [11-13]. It optimizes neutron flux and detection efficiency to study thin samples of actinides. GRAPHEME presently consists of four planar high purity germanium detectors. The teams involved from IRMM, IFIN-HH and CNRS/IN2P3/IPHC work together closely.

The data from both setups are analysed following a very similar methodology to obtain inelastic cross sections from measurements of gamma-ray yields and the neutron fluence. This method was first detailed in reference [6] and the expressions summarised there are also the basis for the correctness, uncertainty and covariance analyses with which we are concerned here.

Concerning the measurements of the gamma-ray yields an important aspect is the determination of the detection efficiency. Monte Carlo simulations are made using as-built models for the detectors. These models are fine-tuned to accurately reproduce calibration data obtained with a ^{152}Eu source placed in the setup at the location of (and replacing) the sample under study. These simulations were performed with MCNP5 and GEANT4 to cross check against code dependence, to study the sensitivity of the model parameters and to generally assess the accuracy of such calculations. It was concluded that an uncertainty of about 2% should be assigned to efficiencies estimated with such calculations [14].

For measurements of the neutron fluence an important parameter is the efficiency for the detection of a fission event in the ^{235}U-based ionisation chamber. Here, we recently made important corrections to the procedure reported in reference [6]. These corrections concern the estimate of the fraction of fission events depositing charge in the ionisation chamber but resulting in signal amplitudes below the threshold and the fraction of fission events with fragments stopped entirely in the ^{235}U layer, thus leaving no charge in the detector. This procedure was corrected based on two publications dealing with fission fragments lost in the deposit [15,16] and on extensive modelling and experimental work to understand the pulse height distribution in fission ionisation chambers at low amplitude [17,18]. The corrected procedure was tested successfully in an inter-comparison exercise taking place at PTB [19] establishing that the new procedure allows determining neutron fluence within the stated uncertainty of 2.3%. The new corrected procedures were first applied for sodium [20], using a detection efficiency for a fission event of 83(1)% determined according to the new, validated evaluation procedure. In

contrast, this efficiency was estimated to be 98.4(1.6)% in reference [6]. Although the difference is somewhat affected by the choice of threshold it is still very substantial.

The present report consists of five contributions besides the present summary.
In the first, we delineate a method for covariance generation that is under development. It entices the stochastic determination of the covariance matrix associated with the current updated and corrected measurement methodology by using a Monte Carlo technique.
The second contribution serves as an introduction to the studies of the efficiency of the fission chamber. It starts with a section on fission fragments not depositing charge in the counter gas, as they are stopped in the deposit or backing. Here, it is shown that modern stopping data [22] overestimate the effective range of fission fragments in $^{235}UF_4$ layers, in agreement with the finding of reference [16]. This shows that state-of-the-art simulation tools implementing the best available stopping powers for low energy heavy ions will underestimate the fraction of fission fragments stopped in a UF_4 deposit by 50%.
In the second part of the contribution the pulse height distribution is introduced on the basis of a simple model, to set the stage. The difficulties in obtaining truly quantitative pulse height spectra with modern simulation tools like GEANT4 are illustrated in [17], a work that triggered the re-investigation of our efficiency estimate for fission chambers. The simplified model helps understand the pulse height spectrum in an ionisation chamber. It is evaluated by a Monte Carlo simulation and by analytical expressions derived in the contribution. Of particular importance is the pulse height spectrum for low amplitudes. It is nonzero at zero amplitudes, a feature that initially appears to be rather counter intuitive. Since this feature emerges from Monte Carlo studies [17], our intuition must be misleading, and this conclusion was the starting point for the development of the simple model. The results of this model were already given in reference [18]. A dedicated simulation tool was developed at PTB for fission ionisation chambers. Results obtained with this tool are shown in reference [19] and clearly show a similar behaviour of the pulse height spectra at low amplitude. This work also confirms the need for shorter ranges of fission fragments in the deposit material to obtain quantitative agreement between measured and calculated pulse height spectra (in this case for painted uranium oxide deposits [21]).
The third, fourth and fifth contribution concern measurement reports from tests at the IRMM van de Graaff laboratory with various ^{235}U-based fission ionisation chambers. These tests were instrumental in developing our understanding of the pulse height distributions in these chambers and unambiguously determined that a reliable fluence inter-comparison can only be obtained using the time-of-flight technique. It was later found that the latter finding re-established a conclusion that is tersely presented also in reference [21].
The third contribution also clearly states the correction factor needed to compensate for the wrong fission chamber efficiency used in the data published for ^{52}Cr, ^{208}Pb and ^{209}Bi [7-9].

Together with published work [11, 14, 18, 19] the contributions collected in this report document in detail the major steps that were made in improving the correctness of our measurement and data analysis procedures. Also the way forward towards determining covariances for our (n,xng)-data is outlined and laid down in data analysis routines. It remains to thoroughly test the approach and apply it to data of interest.

References

[1] M. Salvatores and R. Jacqmin, editors, Uncertainty and target accuracy assessment for innovative systems using recent covariance data evaluations, International Evaluation Co-operation, Volume 26, Nuclear Science, NEA/WPEC-26, NEA No. 6410, ISBN 978-92-64-99053, Nuclear Energy Agency, Organisation for Economic Development and Co-operation (2008).

[2] P. Obložinský, editor, Special Issue on Workshop on Neutron Cross Section Covariances, June 24-28, 2008, Port Jefferson, NY, USA, Nuclear Data Sheets, volume 109, number 12 (2008).

[3] The High Priority Request List for Nuclear Data, www.oecd-nea.org/dbdata/hprl, International Evaluation Co-operation, Nuclear Science, Nuclear Energy Agency, Organisation for Economic Development and Co-operation (consulted 2011).

[4] ANDES - Accurate Nuclear Data for Nuclear Energy Sustainability, www.andes-nd.eu (2010).

[5] JRC Project Browser, European Commission, http://projects.jrc.ec.europa.eu (2011).

[6] L.C. Mihailescu, L. Oláh, C. Borcea, and A.J.M. Plompen, A new HPGe setup at GELINA for measurement of gamma-ray production cross sections form inelastic neutron scattering, Nucl. Instrum. Method. A 531 (2004) 375.

[7] L.C. Mihailescu, C. Borcea, A.J. Koning, A.J.M. Plompen, High resolution measurement of neutron inelastic scattering and (n,2n) cross-sections for ^{52}Cr, Nuclear Physics A 786 (2007) 1.

[8] L.C. Mihailescu, C. Borcea, A.J. Koning, A. Pavlik, A.J.M. Plompen, High resolution measurement of neutron inelastic scattering and (n,2n) cross-sections for ^{209}Bi, Nuclear Physics A 799 (2008) 1.

[9] L.C. Mihailescu, C. Borcea, P. Baumann, Ph. Dessagne, E. Jericha, H. Karam, M. Kerveno, A.J. Koning, N. Leveque, A. Pavlik, A.J.M. Plompen, C. Quétel, G. Rudolf, I. Tresl, A measurement of (n,xng) cross sections for ^{208}Pb from threshold up to 20 MeV, Nuclear Physics A 811 (2008) 1.

[10] A. Negret, C. Borcea, A.J.M. Plompen, Cross sections for neutron inelastic scattering on ^{28}Si, J. Korean Physical Society, 59 (2011) 1765.

[11] J.C. Thiry, C. Borcea, P. Dessagne, J.C. Drohé, E. Jericha, H. Karam, M. Kerveno, A.J. Koning, A. Pavlik, A. Plompen, C. Rouki, G. Rudolf, M. Stanoiu, Measurement of (n,xng) reactions of interest for the new nuclear reactors, J. Korean Physical Society, 59 (2011) 1880.

[12] M. Kerveno, C. Borcea, Ph. Dessagne, J.C. Drohé, E. Jericha, H. Karam, A.J. Koning, A. Negret, A. Pavlik, A.J.M. Plompen, C. Rouki, G. Rudolf, M. Stanoiu, J.C. Thiry, Measurement of (n,nxng) reactions of interest to new nuclear reactors, Proceedings of the workshop NEMEA-6 Nuclear Measurements Evaluations and Applications, 25-28 October 2010, Kraków, Poland, Nuclear Science, NEA/NSC/DOC(2011)4, Nuclear Energy Agency, Organisation for Economic Co-operation and Development (2011).

[13] J.C. Thiry, C. Borcea, Ph. Dessagne, J.C. Drohé, E. Jericha, H. Karam, M. Kerveno, A.J. Koning, A. Negret, A. Pavlik, A.J.M. Plompen, C. Rouki, G. Rudolf, M. Stanoiu, Measurement of (n,nxng) reactions at high precision, Proceedings of the workshop NEMEA-6 Nuclear Measurements Evaluations and Applications, 25-28 October 2010, Kraków, Poland, Nuclear Science, NEA/NSC/DOC(2011)4, Nuclear Energy Agency, Organisation for Economic Co-operation and Development (2011).

[14] D. Deleanu, C. Borcea, Ph. Dessagne, A. Negret, A.J.M. Plompen, J.C. Thiry, The gamma-efficiency of the GAINS spectrometer, Nucl. Instrum. Meth. A 624 (2010) 130

[15] G.W. Carlson, The effect of fission fragment anisotropy on fission-chamber efficiency, Nucl. Instrum. Meth. 119 (1974) 97.

[16] C. Budtz-Jørgensen, H.H. Knitter and G. Bortels, Assaying of targets for nuclear measurements with a gridded ionisation chamber, Nucl. Instrum. Meth. A 236 (1985) 630.

[17] J.C. Thiry, PhD thesis, University of Strasbourg (2010).

[18] A. Plompen, N. Nankov, C. Rouki, M. Stanoiu, C. Borcea, D. Deleanu, A. Negret, P. Dessagne, M. Kerveno, G. Rudolf, J.C. Thiry, M. Mosconi, R. Nolte, Measurement of (n,xng) reactions of interest for the new nuclear reactors, J. Korean Physical Society, 59 (2011) 1581.

[19] M. Mosconi, Ph. Dessagne, M. Kerveno, R. Nolte, A.J.M. Plompen, C. Rouki, J.C. Thiry, Characterisation of fission ionisation chambers using monoenergetic neutrons, Proceedings of the final scientific EFNUDAT workshop, 30 August – 02 September 2010, CERN, Geneva, editor E. Chiaveri, ISBN 978-92-9083-365-9, (2010) 99.
[20] C. Rouki, S. Kopecky, N. Nankov, A.J.M. Plompen, M. Stanoiu, C. Borcea, A. Negret, Neutron inelastic cross section measurements for sodium, J. Korean Physical Society, 59 (2011) 1660; C. Rouki, J.C. Drohé, A. Moens, N. Nankov, A. Plompen, M. Stanoiu, Neutron inelastic scattering cross section measurements for ^{23}Na, JRC Scientific and Technical Reports, EUR 24871 EN, ISBN 978-92-79-19842-7, DOI 10.2787/42712, European Union (2011).
[21] D.B. Gayther, International intercomparison of fast neutron fluence-rate measurements using fission chamber transfer instruments, Metrologia 27 (1990) 221.
[22] J.F. Ziegler, J.P. Biersack, M.D. Ziegler, SRIM The stopping and range of ions in matter, www.srim.org, SRIM Co., Chester, MD 21619, USA, ISBN 0-9654207-1-X (2008)

2. Uncertainty limits and covariances of the (n,n') cross sections determined using the gamma spectroscopy technique at GELINA

A. Negret[1], C. Borcea[1], D. Deleanu[1], and A.J.M. Plompen[2]

[1] *"Horia Hulubei" National Institute for Physics and Nuclear Engineering, 077125 Bucharest-Măgurele, Romania*
[2] *European Commission, Joint Research Center, Institute for Reference Materials and Measurements, B-2440 Geel, Belgium*

December 19, 2011

Abstract

The present report addresses the analysis procedure used for the determination of the neutron inelastic cross sections using the GAINS setup at the GELINA neutron source of EC-JRC-IRMM. The various sources of uncertainty and correlations are investigated. A procedure used to determine the experimental covariances is described.

1 Introduction

A detailed study of the uncertainty limits and covariances of the (n,n') cross sections determined using the gamma spectroscopy technique at GELINA is ongoing under the frame of the ANDES project. As it was emphasized many times, the current reaction databases contain experimental data that are either contradictory or have a large uncertainty compared to that required by the development of a new generation of nuclear reactors. Moreover, the databases are often missing the covariance matrices of the experimentally determined cross sections.

The main goal of the ANDES project is to make a qualitative step further in the knowledge of the nuclear data necessary for the development of the future nuclear systems. This implies both a sustained experimental and theoretical effort.

Under these circumstances, the present report addresses the investigation of covariances as they arise from the specific analysis procedure used for the determination of the (n,n') cross sections using the gamma spectroscopy technique at the GELINA neutron source using the GAINS setup.

2 Methodology for the investigation of covariances

A detailed overview of the experimental technique and of the present analysis procedure was already given elsewhere [1, 2, 3, 4, 5]. The (n,n'γ) method is based on the detection of the gamma rays emitted by the nucleus under investigation excited following the inelastic scattering of the neutrons. Combining the information from each of the eight HPGe detectors of the GAINS spectrometer with that recorded by the ^{235}U fission chamber used for beam monitoring, one can first deduce the differential gamma production cross sections at 110° and 150°. The choice of the two angles representing the nodes of the fourth degree Legendre polynomial allows the angular integration of the cross section. Additional corrections are necessary for multiple scattering processes. Using the levels scheme of the nucleus under investigation one can compute the level production cross sections and the total inelastic cross section. The procedure is rather powerful allowing the precise determination of the cross sections with very good neutron energy resolution.

The experimental result of the (n,n') measurements consist of cross sections: gamma production cross sections, level cross sections and total inelastic cross sections. A large number of data are produced: for each gamma ray or level, the cross section is calculated for about 2000 different values of the neutron energy. A simple estimate: if we calculate the cross section for 20 gammas and 20 levels in a nucleus, this means about (20+20)*2000 = 80000 numbers. Correlations occur between any of these experimental cross sections.

We propose a straightforward approach to the investigation of covariances, based on formula 7. According to this formula, in order to check if there are correlations between any two cross sections (out of the 80000 measured) we should repeat the measurement n times. Then we can compute average values for the two cross sections and, using formula 7, we can estimate the covariances.

Of course, repeating the measurement n times and performing the full data analysis n times is not possible. Instead, we will only perform the data analysis n times. In order to obtain slightly different results, we will vary the input observables. This variation of the input observables is performed within their uncertainty limits, applying the correct distribution and the correlations among these parameters.

Fig. 1 shows the parameters that are varied:

- the HPGe yield,
- the HPGe efficiency,
- the FC yield and
- the FC efficiency.

Finally, a serious difficulty of our investigation is that the correlation matrix is much too large. As a simple solution to this issue we consider limiting the number of neutron energy bins.

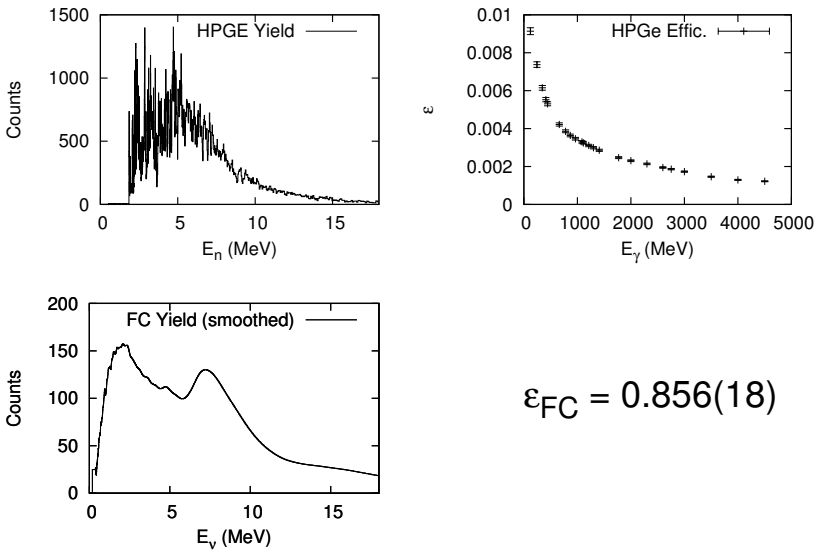

Figure 1: The experimentally determined observables that are varied in order to deduce the correlations among the final cross sections.

2.1 The HPGe yields

GAINS consists of eight HPGe detectors. Each of them produces the yield for each of the 20 gammas and for each of the 2000 neutron energies. There is one file per gamma ray and per detector and each file has one line for each neutron energy.

The number of counts in each channel is computed by integrating the counts in the peak and subtracting the background. We consider that the number of counts in one channel is independent from the number of counts in other channels.

For each channel the n "measurements" are generated by considering a Gauss distribution with x_0 equal to the number of counts and the σ given by the uncertainty of the number of counts in that channel. As an example, the channel corresponding to E_n=2000 keV for the yield of the gamma of 1779 keV from ^{28}Si recorded by detector 1 contains 127±11 counts. Fig. 2 displays in red a Gaussian with x_0=127 and σ=11. The green points represent a histogram of the number of counts generated for this particular channel in order to "simulate" the n measurements.

2.2 HPGe efficiency

The efficiencies of the HPGe detectors for the geometrically extended sample are generated through a complicated procedure involving precise MCNP sim-

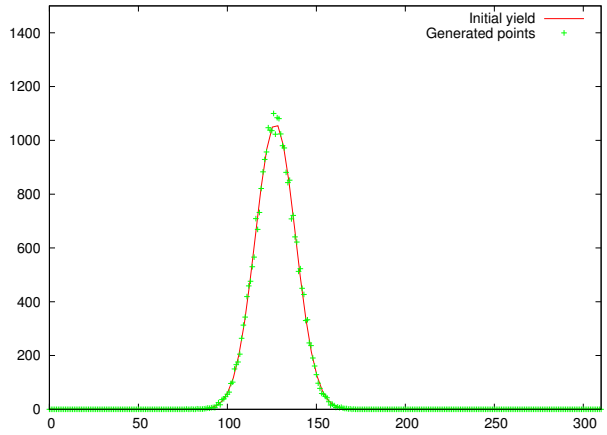

Figure 2: The distribution of the number of counts generated for a certain neutron energy channel from a HPGe yield.

ulations of the detection array [6]. The procedure consists basically of fitting each detector parameter using experimental efficiencies determined with a ^{152}Eu calibration source followed by the use of the simulation for the generation of efficiencies for the real sample. An overall relative uncertainty of 2% is associated with this procedure, this value being based on the following arguments:

- The uncertainty of the calibration source is 0.7%.
- The precision of the determination of the area of each of the peaks used for the determination of the experimental efficiency is of the order of 2%.
- The agreement between each experimentally determined efficiency and the fitted value is of the order of 2%.

A detailed analysis of the procedure used to determine the HPGe efficiency is presented in Ref. [6]. Two well known simulation packages - MCNP and GEANT4 - were used and the results were compared. A good agreement was found between the two approaches. The result of variation of a the most important parameters on the detector efficiencies is also given there.

The generation of the n sets of efficiencies is done following a Bayesian approach. The likelihood function is chosen to constrain the model to reproduce the measured efficiencies determined with a calibrated point source. This approach implies extensive calculations that make use of the model evaluated for large sets of parameter values. Considering that the model is a sophisticated Monte Carlo simulation, the adequate practical choice is to linearize the model. In a second stage, the linearized model is used to generate the required sets of efficiencies following a Markov chain Monte Carlo prescription.

This procedure was partially tested and is currently under implementation. It requires very intensive Monte Carlo calculations for the linearization of the

simulated model of each of the germanium detectors and for a large number of gamma energies.

2.3 FC yield

In order to allow an accurate determination of the detection efficiency the ^{235}U deposits are limited to 0.4 mg/cm^2. Eight such deposits are combined in one fission chamber providing about 3 mg/cm^2 of ^{235}U effectively and maximizing the efficiency. To minimize attenuation the backings for these deposits are 20 μm aluminum. Nevertheless, the number of counts accumulated by the acquisition system connected to the fission chamber is very small: during one experiment, a channel corresponding to a certain neutron energy counts about 100 pulses. The statistical uncertainties are therefore very large.

In order to reduce this uncertainty we use the physical argument that, during the production of the neutron yield no resonant process is involved: The electron beam hits the GELINA production target and produces Bremsstrahlung. Then the gamma rays with various energies, mainly through (γ,n) reactions, produce the white neutron flux [7]. Moreover, the FC setup remains unchanged from one experiment to another.

Therefore, we performed the following procedure: we summed the FC spectra from several measurements. Then we applied a smoothing procedure on the summed spectrum. For each individual measurement we integrate the FC spectrum. Then we replace the real FC spectrum (that has big relative uncertainties) with the smoothed spectrum previously generated and scaled to the real integral. This way, the uncertainties introduced by the FC data are not larger than 2%.

However, the above procedure introduces strange correlations in the data due to smoothing procedure: each channel becomes partially correlated with the neighbors, but this correlation is less pronounced for points that are further apart.

Generating the FC data n times for the purpose of the covariance analysis involved the reproduction of the procedure described above n times. In each case we vary the number of counts from each channel of the summed FC spectrum taking into account the uncertainty limits and a Gauss distribution. Then we apply the smoothing procedure in order to generate one instance of the FC Yield file.

2.4 FC efficiency

Generating n values for the FC efficiency is a simple task as this is a single number for the whole experiment. The FC efficiency is calculated following a rather complicated analysis, with several corrections. A detailed description of this procedure is given in Ref. [8].

All values are included in the $[x_0 - \sigma, x_0 + \sigma]$ range, distributed following a constant distribution.

We note here already that the FC efficiency, being a fixed number (it does not depend on the neutron energy and of course not on the gamma energy), introduces a complete correlation of all the cross sections generated in a measurement.

3 Conclusions

In conclusion, we present an overview of our specific procedure for the generation of covariances for the neutron inelastic cross section data obtained with the GAINS spectrometer using the gamma spectroscopy techniques. It is based on a Monte Carlo approach, relying on the consistent variation of the most important experimental observables.

The procedure is currently under implementation. Various codes and procedures are developed for generation of "multiple experimental sets" starting from one real experimental result and for the combination of the final data into correlation matrices.

Appendices

A Errors and uncertainties

We will start with a short review of the terms defined in the Guide to the expression of uncertainty in measurement issued by the Working Group 1 of the Joint Committee for Guides and Metrology [9].

Ref. [9] makes a clear distinction between *error* and *uncertainty*. The *errors* represent mistakes in the measurements. There are two types of errors:

- *random errors*, due to unknown effects; they can be minimized by multiple measurements and
- *systematic errors*, due to recognizable effects, that can be corrected.

After all error corrections are applied, there is still the *uncertainty* of a measurement that expresses the lack of precision of that measurement. There are two kinds of uncertainties:

- it Type A uncertainties, that are evaluated using statistical methods. Measuring n times the best estimates of the value Q is

$$\bar{q} = \frac{1}{n}\sum_{i=1}^{n} q_k, \tag{1}$$

and of the variance σ^2

$$s^2(q_k) = \frac{1}{n-1}\sum_{j=1}^{n}(q_j - \bar{q})^2. \tag{2}$$

- it Type B uncertainties, that are evaluated using scientific thinking or any other methods that are not statistical. If, in this case, only an interval can be determined $[a_-, a_+]$ then one can assume a constant distribution and then

$$x_i = \frac{a_- + a_+}{2}, \tag{3}$$

$$u^2(x_i) = \frac{(a_+ - a_-)^2}{\sqrt{(12)}}. \tag{4}$$

The result of the combination of several uncertainties (using a propagation formula) is *the combined standard uncertainty*. In case of uncorrelated input variables the propagation formula is

$$u_c^2(y) = \sum_{i=1}^{N} \left(\frac{\partial f}{\partial x_i} \right)^2 u^2(x_i) \tag{5}$$

while for correlated input variables it is

$$u_c^2(y) = \sum_{i=1}^{N} \left(\frac{\partial f}{\partial x_i} \right)^2 u^2(x_i) + 2 \sum_{i=1}^{N-1} \sum_{j=i+1}^{N} \frac{\partial f}{\partial x_i} \frac{\partial f}{\partial x_j} u(x_i, x_j). \tag{6}$$

$u(x_i, x_j)$ is the covariance of the two input parameters. An estimation of the covariance of two random variables measured n times is

$$s(\bar{q}, \bar{r}) = \frac{1}{n(n-1)} \sum_{k=1}^{n} (q_k - \bar{q})(r_k - \bar{r}) \tag{7}$$

Finally, the correlation coefficient is defined as

$$r(x_i, x_j) = \frac{u(x_i, x_j)}{u(x_i) u(x_j)} \tag{8}$$

References

[1] A. Negret, C. Borcea, J.C. Drohe, L.C. Mihailescu, A.J.M. Plompen and R. Wynants, Proceedings of the International Conference on Nuclear Data for Science and Technology ND2007, April 22-27 2007, Nice, France (2008).

[2] L.C. Mihailescu, L. Olah, C. Borcea and A.J.M Plompen, Nucl. Instrum. Meth. Phys. Research A531, 375 (2004).

[3] L.C. Mihailescu, C. Borcea, A.J. Koning and A.J.M Plompen, Nucl. Phys. A786, 1 (2007).

[4] L.C. Mihailescu, C. Borcea, A.J. Koning, A. Pavlik and A.J.M Plompen, Nucl. Phys. A799, 1 (2008).

[5] L.C. Mihailescu, C. Borcea, P. Baumann, Ph. Dessagne, E. Jericha, H. Karam, M. Kerveno, A.J. Koning, N. Leveque, A. Pavlik, A.J.M. Plompen, C. Quetel, G. Rudolf and I Tresl, Nucl. Phys. A811, 1 (2008).

[6] D. Deleanu, C. Borcea, Ph. Dessagne, M. Kerveno, A. Negret, A.J.M. Plompen, J.C. Thiry, Nucl. Instrum. Methods Phys. Res. A624, 130 (2010).

[7] D. Ene, C. Borcea, S. Kopecky, W. Mondelaers, A. Negret, A.J.M. Plompen, Nucl. Instrum. Methods Phys. Res. A618, 54 (2010).

[8] A.J.M. Plompen *et al.*, J. Korean Phys. Soc. 59, 1581 (2011).

[9] JCGM 100:2008 report produced by the Working Group 1 of the Joint Committee for Guides and Metrology (JCGM/WG1).

3. Fission ionisation chambers, loss in the deposit and the pulse height spectrum

A. Plompen

December 19, 2011

1 Loss of fission fragments in the deposit

Due to the finite thickness of the deposit and the range of a fragment some will not deposit energy in the counting gas. Since these fragments do not contribute to the pulse height distribution of the counter, they lower the efficiency of the ionization chamber.

Estimates for these effect should take account of the angular distribution of the emitted fragments [1] and to a lesser extent the recoil energy of the fissioning system [2]. The angular distribution can be taken as $W(\theta) = 1 + c_2 P_2(\cos\theta)$ where θ is the angle with the normal to the surface. The normalization is $\int_{4\pi} W d\Omega = 4\pi$. Straede et al. [3] confirm this for ^{235}U in the range $0.15 \leq \cos\theta \leq 0.94$ and E_n=0.5-6 MeV and for thermal neutrons. The anisotropy $b = \frac{W(0^\circ)}{W(90^\circ)} - 1$ was evaluated by Kapoor in the context of the 1983 standards file [4] and is in good agreement with the more recent reference [3].

The energy dependence of the anisotropy is somewhat complex (Figure 1). It rises from 0 to 0.17(3) for E_n=0.1 to 1.5, remains constant to 5.5 MeV, rises to a maximum of 0.4 at 8 MeV and then decreases to about 0.27(4) at 12 MeV remaining approximately constant to 20 MeV. The relation between b and c_2 is

$$c_2 = \frac{2b}{3+b} \quad \text{and} \quad b = \frac{3c_2}{2-c_2},$$

showing that c_2 is approximately two thirds of b.

1.1 Anisotropy

It is instructive to first discuss the case while neglecting the recoil effect. A simple geometric estimate may be made. Assume a layer with thickness t and a fission

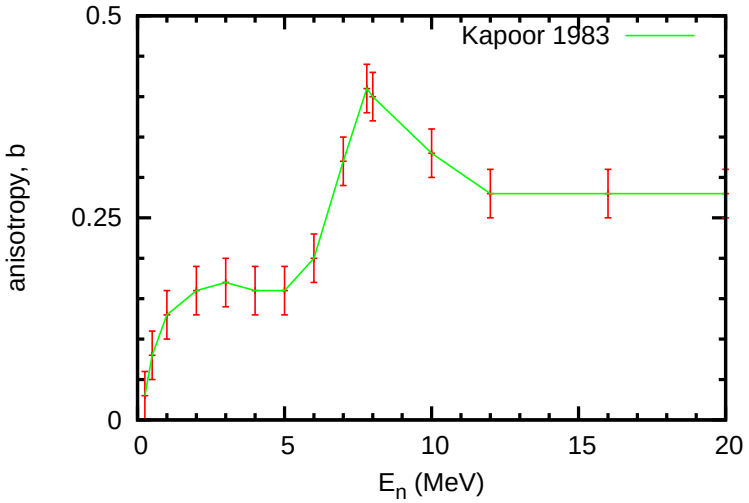

Figure 1: Anisotropy for ^{235}U according to reference [4].

fragment with range R in the deposit. Furthermore, say that fission takes place at a height z into the deposit measured from the interface with the counter gas. For the purpose of deriving the number of fragments stopped in the deposit it is convenient to take θ to be the angle of a fission fragment with the negative z-axis. The deposit is perpendicular to the z-axis. The fraction $m_1(z)$ of unobserved fissions because the fragment is stopped in the deposit is (fission at z)

$$m_1(z) = \frac{1}{2\pi}\int_0^{2\pi} d\phi \int_0^{z/R} du\; W = \int_0^{z/R} du \left[1 - \frac{c_2}{2} + \frac{3c_2}{2}u^2\right] = \left[1 - \frac{c_2}{2}\right]\frac{z}{R} + \frac{c_2}{2}\frac{z^3}{R^3}$$

This must be averaged over the layer thickness

$$m_1 = \frac{1}{t}\int_0^t dz\, m_1(z) = \left[1 - \frac{c_2}{2}\right]\frac{t}{2R} + \frac{c_2}{8}\frac{t^3}{R^3}.$$

Considering neutron-induced fission of ^{235}U a typical light fragment is ^{96}Rb and the accompanying heavy fragment is ^{140}Cs. In $^{235}UF_4$ the range of the first is 8.8 mg/cm^2 (113 MeV) and the range of the second is 6.6 mg/cm^2 (78 MeV) [3, 5]. For a layer thickness of $422 \times (235 + 4 \times 19)/235 = 558\mu$g/cm^2 this implies that $\frac{t}{2R} = 0.032$ and 0.042 for the light and heavy fragment. Of course for each mass split one must take the average over light and heavy fragment (0.037 for this case). In any case, the second term for m_1 is almost 4000 times smaller than the

first term and may be neglected. We then have very nearly

$$m_1 = \left[1 - \frac{c_2}{2}\right]\frac{t}{2R} = \frac{t}{2R}\frac{1}{1 + b/3},$$

which is the expression used by Gayther [1].

It is important to see that the angular distribution correction is a correction on the correction: The unobserved fraction due to full energy release in the deposit is basically t/2R and the anisotropy reduces this to 0.95(1)t/2R. For energies in the range from 6 to 20 MeV the anisotropy is larger, peaking at 0.40(5). For the peak value we have 0.88(1)t/2R (Figure 2).

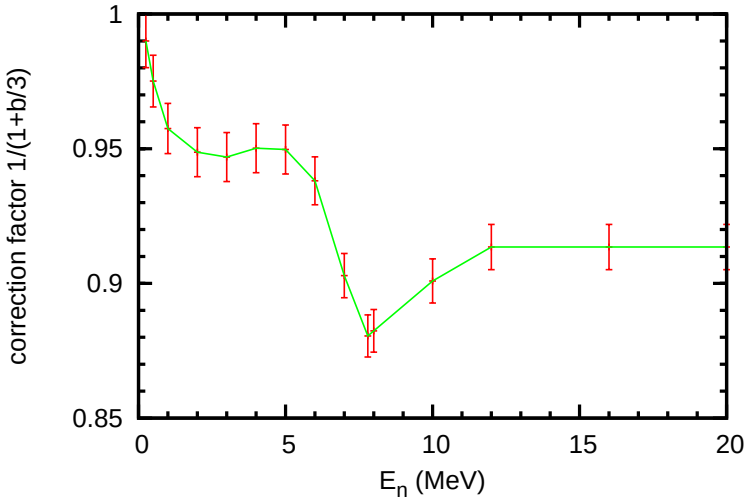

Figure 2: The correction factor to t/2R due to anisotropy for ^{235}U according to references [1, 4].

Of course the extremes of the distribution contain still heavier fragments combined with a lighter fragment. This in combination with a reduced TKE (total kinetic energy) may lead to an even shorter range. Using Straede an extreme combination would be ^{86}Se+^{150}Ce with 113 and 65 MeV and ranges 8.6 and 5.2 mg/cm^2. Then t/2R is 0.032 and 0.053 resp., and on average 0.043. Also, the distributions are incident neutron energy dependent. Thus, a simulation would tell us about the proper average correction and the energy dependence of such a correction. Here I have used the thermal neutron induced fission fragment mass distribution [3]. The two cases mentioned are summarised in the table.

Budtz-Jörgensen et al. [6] found α=10.5(7)% cm^2/mg, experimentally. The experimental value suggests a substantially larger loss of fragments in a deposit

Table 1: Total kinetic energy and range data for a typical and an extreme mass split (HF=heavy fragment, LF=light fragment, R is range in UF_4 according to SRIM2008 [5], $\frac{1}{\overline{R}} = 0.5(\frac{1}{R_{LF}} + \frac{1}{R_{HF}})$). The data for thermal neutron fission of ^{235}U from Straede et al. [3] were used. Energies in MeV, ranges in mg/cm^2, $\alpha = \frac{1}{2\overline{R}}$ in cm^2/mg.

TKE	LF	E	R	HF	E	R	$\overline{R}$	α
192	^{96}Rb	114	8.8	^{140}Cs	78	6.6	7.5	0.066
178	^{86}Se	113	8.6	^{150}Ce	65	6.0	7.1	0.071

than is given by the SRIM2008 program. The reason for this is not fully understood. It may be that fission fragments of 0.5 to 1 MeV/u have velocities for which there is no Bragg-peak in the energy deposition as function of the distance traveled. Thus, the energy deposited per unit length (Figure 3) near the end of the track is well below the average, thereby reducing the charge deposition in the gas for tracks barely entering the counter gas (in relative terms and compared to faster ions that do exhibit a Bragg peak in their energy deposition).

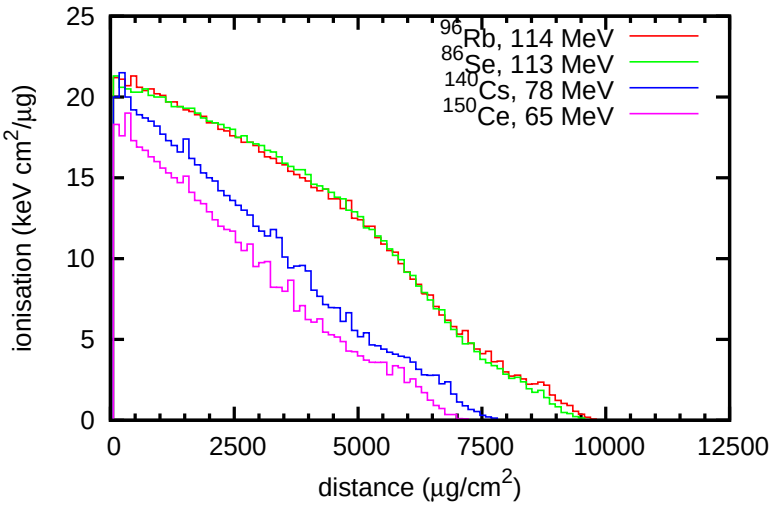

Figure 3: Energy release to ionisation for four fission fragments according to the SRIM code [5].

In any case, the value for α found in reference [6] corresponds to an effective range of R_{eff}=4.8(3) mg/cm^2. For the GAINS fission chamber this gives 5.3(3)% for t/2R_{eff}. For the deposits made in 2008 with a typical U-235 thickness of 0.422 mg/cm2, the fractional loss is 6.0(3)%.

1.2 The recoil effect.

Reference [2] considers the combined effect of the anisotropy and the recoiling fissioning nucleus. The recoil effect is governed by the parameter η given by

$$\eta = \frac{1}{1+A}\sqrt{\frac{E_n}{E_F/A_F}},$$

where A is the target mass, A_F the fission fragment mass and E_F its energy. Note that on average E_F/A_F is 1 MeV/u for the light and 0.5 MeV/u for the heavy fragment, so that $0.0035E_n \leq \eta \leq 0.0043E_n$ for neutron energy E_n in MeV.

For the angular distribution in the center of mass, as specified above, the angular distribution in the laboratory is to lowest order in η given by

$$W(\theta) = 1 + \left(2 - \frac{3}{2}a_2\right)\eta P_1(\cos\theta) + a_2 P_2(\cos\theta).$$

Several cases can be distinguished. For a fission chamber perpendicular to the beam and with an equal number of deposits facing the beam and looking away from it the inefficiency is given by

$$m_G^A = \frac{t}{2R}\left(1 - \frac{c_2}{2}\right)\left(1 + \frac{\eta^2}{8(t/2R)^2}\right).$$

This case is the appropriate one for the fission chamber used in the GAINS setup (Figure 4. From the figure it is clear that the fraction of fragments lost in the

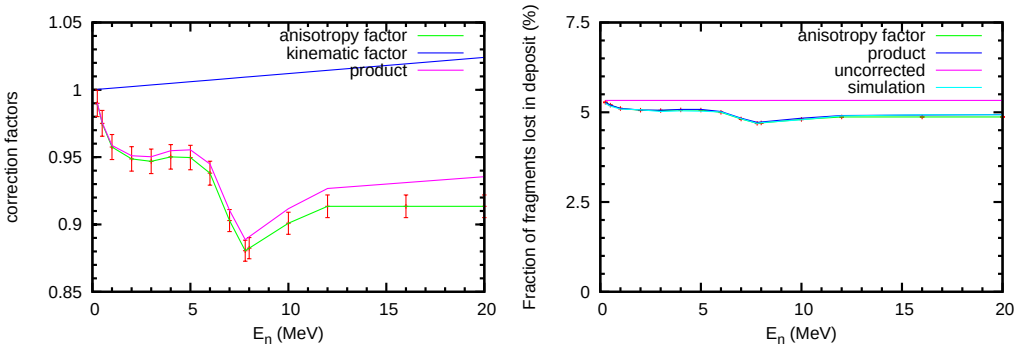

Figure 4: Carlson correction factors (left) and impact on fragments lost in the deposit for the GAINS chamber (right). The anisotropy factor is the same as that of Gaythe r.

deposit varies from 4.7 to 5.3% in case of the GAINS chamber. Clearly, both

anisotropy and the recoil effect are of minor consequence for the GAINS chamber, and so far we did not correct for these effects in the analysis.

The correctness of Carlson's approach was verified by a simple Monte Carlo program and the result is shown in the same figure.

Finally, it is shown that the kinematic effect is more dramatic when only foils are used that face the beam (foils facing backwards), or when only foils are used that face away from the beam. An additional 2% change in the loss of fragments may result from the kinematic effect. It is therefore advantageous to have an equal number of deposits facing both ways.

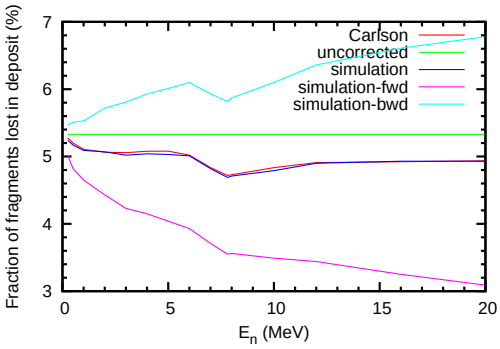

Figure 5: Impact of using only forward or only backward facing foils, compared with an equal number in both directions. GAINS deposits taken as example.

2 A simple model for the pulse height distribution

For a qualitative understanding of the pulse height distribution in a parallel plate ionization chamber, the following simple model will be used. Assume that all fission fragments are emitted isotropically starting with the same energy E_0, that the range in the deposit is $R_d(E) = R_d E/E_0$ and that the range in the counter gas is $R_g(E) = R_g E/E_0$. Furthermore assume that the charge is deposited uniformly along the track in the gas.

The deposit thickness is t, the parallel plate distance is d and the plates have infinite area. Measured from the deposit-gas interface fission takes place at a distance z. The fission fragment has cosine u with the normal of the deposit-gas interface. The distance to the interface is therefore $\frac{z}{u}$. If $R_d < \frac{z}{u}$ then the fragment will not leave the deposit and the fragment will not contribute to the pulse height distribution. If $R_d > \frac{z}{u}$ then the fragment enters the gas with energy

$E_g(z,u) = E_0(1 - \frac{z}{R_d u})^+$ and its range in the gas will be

$$R_g(z,u) = R_g\left(1 - \frac{z}{R_d u}\right)^+ .$$

Denote by Q_0 the charge that a fragment of energy E_0 would deposit in the gas if no energy would be lost in the deposit and the fragment would not strike the opposite electrode. Then the amount of charge deposited for the fragment is

$$Q(z,u) = \begin{cases} Q_0 \frac{d}{R_g u} & R_g(z,u) > \frac{d}{u} \\ Q_0(1 - \frac{z}{R_d u})^+ & R_g(z,u) < \frac{d}{u} \end{cases}$$

For signal formation we assume that the positive ions do not move, so that the voltage induced is due exclusively to the collection of the electrons. Two configurations are possible. The collecting electrode is opposite to the deposit (1), or it is the one that carries the deposit (2). Denote the maximum voltage that may be obtained from a single track by V_0. It corresponds to a track in the gas parallel to and just outside of the deposit with the collecting electrode on the opposite side of the chamber (configuration 1). We now have

$$V_1 = \begin{cases} \frac{1}{2}\frac{V_0}{Q_0} Q(z,u) & R_g(z,u) > \frac{d}{u} \\ \left(1 - \frac{uR_g(z,u)}{2d}\right)\frac{V_0}{Q_0} Q(z,u) & R_g(z,u) < \frac{d}{u} \end{cases}$$

$$V_2 = \begin{cases} \frac{1}{2}\frac{V_0}{Q_0} Q(z,u) & R_g(z,u) > \frac{d}{u} \\ \frac{uR_g(z,u)}{2d}\frac{V_0}{Q_0} Q(z,u) & R_g(z,u) < \frac{d}{u} \end{cases} .$$

With a few substitutions:

$$V_1/V_0 = \begin{cases} \frac{1}{2}\frac{d}{R_g u} & R_g(z,u) > \frac{d}{u} \\ \left(1 - \frac{uR_g(z,u)}{2d}\right)\left(1 - \frac{z}{R_d u}\right)^+ & R_g(z,u) < \frac{d}{u} \end{cases}$$

$$V_2/V_0 = \begin{cases} \frac{1}{2}\frac{d}{R_g u} & R_g(z,u) > \frac{d}{u} \\ \frac{uR_g(z,u)}{2d}\left(1 - \frac{z}{R_d u}\right)^+ & R_g(z,u) < \frac{d}{u} \end{cases} .$$

Using some typical numbers a simulation was made that uses the above expressions while sampling uniformly over the location in the deposit z and the cosine u of the angle of the fission fragment. This is shown in the figure (the right panel highlights the low amplitudes). For the purpose of estimates of fission fragments lost below some threshold amplitude, the two configurations are quite different. For configuration 1, the behavior for low amplitudes is nearly flat with a small increasing slope and a definite offset for zero amplitude. For configuration 2 a much larger contribution is shown at low amplitudes that increases progressively towards zero amplitude. It is interesting to see the large diffference in the

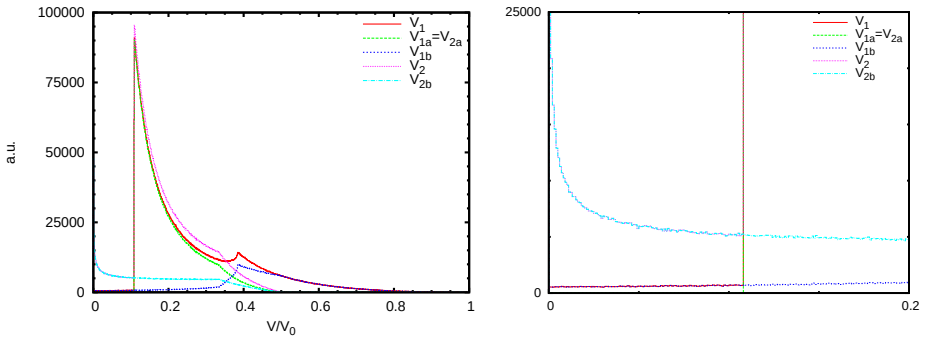

Figure 6: Pulse height distributions from a simplified model for a parallel plate ionization chamber (t=0.5 mg/cm^2, d=6.5 mm, R_d=4.7 mg/cm^2, R_g=30 mm).

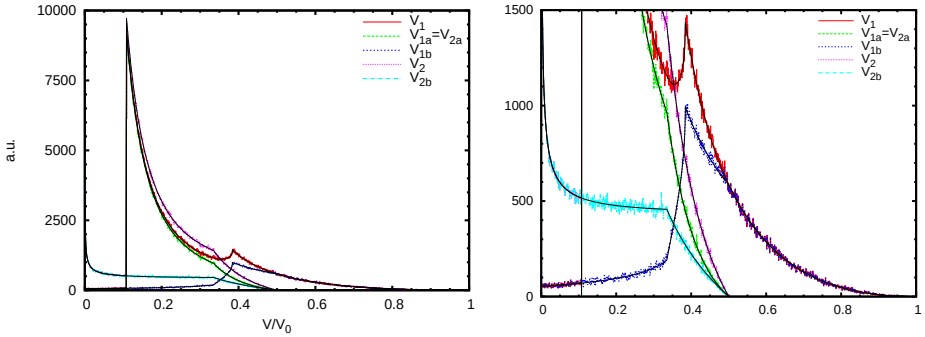

Figure 7: Analytic forms for the pulse height distributions from a simplified model for a parallel plate ionization chamber compared with the simulations (t=0.5 mg/cm^2, d=6.5 mm, R_d=4.7 mg/cm^2, R_g=30 mm). The thin black lines are the various analytic forms given in the text.

b-contributions, the contributions for $R_g(z,u) < \frac{d}{u}$, for the configurations 1 and 2. For configuration 1 the b-contribution is responsible for the highest ($V/V_0 > 0.4$) and for the lowest amplitudes. Here most of the strength is for high amplitudes. For configuration 2, the b-contribution is all at low amplitudes ($V/V_0 < 0.4$), which accounts for the much higher level in the plateau. The precise reason for the zero amplitude behavior of both configurations is not directly clear from the above expressions. The same is true for the pronounced maximum in V_{1b} that leads to a second maximum in V_1.

2.1 An analytic form for the pulse height distribution?

For the model of the present section the probability distribution for z and u is given by $P(z,u) = 1/t$. The condition that fragments enter the gas volume is $u > z/R_d$ and the corresponding probability $P(u > z/R_d) = 1 - \frac{t}{2R_d}$, as deduced above. More

precisely, this is correct for thin layers, that is for layers with $t < R_d$.

Fragments striking the opposite electrode: configurations 1 and 2. Consider now first the pulse height distribution due to fragments striking the opposite electrode. The condition is $R_g(z,u) > \frac{d}{u}$ or $u > \frac{d}{R_g} + \frac{z}{R_d}$ and the probability that an event strikes the opposite electrode is $P(u > \frac{d}{R_g} + \frac{z}{R_d}) = 1 - \frac{d}{R_g} - \frac{t}{2R_d}$. Here, only conditions are considered for which $\frac{d}{R_g} + \frac{t}{R_d} < 1$, so the layer is thin, and the combination of layer and counter thickness may not prevent that a number of fragments strike the opposite electrode. One observes that there are two ranges for which the probability distribution is given by ($\hat{V}_1 = V_1/V_0$)

$$p(\hat{V}_1)d\hat{V}_1 = \begin{cases} du & \frac{d}{R_g} + \frac{t}{R_d} < u \leq 1 \\ \frac{R_d}{t}\left(u - \frac{d}{R_g}\right)du & \frac{d}{R_g} < u \leq \frac{d}{R_g} + \frac{t}{R_d} \end{cases}$$

$$u = \frac{d}{2R_g\hat{V}_1}$$

This may be developed further to give

$$p(\hat{V}_1) = \begin{cases} \frac{d}{2R_g\hat{V}_1^2} & \frac{d}{2R_g} \leq \hat{V}_1 < \frac{1}{2\left(1+\frac{R_g}{d}\frac{t}{R_d}\right)} \\ \frac{R_d}{t}\left(\frac{d}{2R_g\hat{V}_1} - \frac{d}{R_g}\right)\frac{d}{2R_g\hat{V}_1^2} & \frac{1}{2\left(1+\frac{R_g}{d}\frac{t}{R_d}\right)} \leq \hat{V}_1 < \frac{1}{2} \\ 0 & \hat{V}_1 < \frac{d}{2R_g} \quad \wedge \quad \hat{V}_1 \geq \frac{1}{2} \end{cases}$$

A comparison between this analytic form and the simulation shows perfect agreement.

Fragments that do not strike the opposite electrode: charge collected on the electrode with the deposit, configuration 2. As the next case, take $\hat{V}_{2b}$. To simplify notation introduce $z' = z/R_d$, $t' = t/R_d$, $d' = d/R_g$. The condition that $u > z/R_d$ for the track to enter the gas is $u > z'$ and the condition that $R_g(z,u) < d/u$ is $u < z' + d'$. So, together the cosine has to respect

$$z' < u < z' + d'.$$

Consider $P(\hat{V}_{2b} < v)$, the probability that an event for configuration 2, category b has amplitude less than v. The condition is

$$\frac{u}{2d'}\left(1 - \frac{z'}{u}\right)^2 < v \implies (u - z')^2 < 2d'vu \implies u^2 - 2(z' + d'v)u + z'^2 < 0$$

It follows that

$$u_- < u < u_+ \quad \text{for} \quad u_\pm = z' + vd' \pm \sqrt{2vd'z' + v^2d'^2}.$$

Clearly $u_+ \geq z'$, and with some work one finds that $u_- < z'$. Furthermore $u_+ < z' + d'$ may only hold if $v < \frac{1}{2}\frac{d'}{z'+d'}$. Again we need to distinguish domains. Take $v < \frac{1}{2}\frac{d'}{t'+d'}$.

$$\begin{aligned} P(\hat{V}_{2b_1} < v) &= \frac{1}{t'}\int_0^{t'} dz' \left[vd' + \sqrt{2vd'z' + v^2d'^2}\right] \\ &= vd' + \frac{1}{3}\frac{v^2d'^2}{t'}\left[\left(1 + \frac{2t'}{vd'}\right)^{3/2} - 1\right] \end{aligned}$$

For the pulse height distribution this must be differentiated

$$p_{2b_1}(v) = d'\left(1 - \sqrt{1 + \frac{2t'}{vd'}}\right) + \frac{2}{3}\frac{d'^2}{t'}v\left[\left(1 + \frac{2t'}{vd'}\right)^{3/2} - 1\right].$$

The above expression for the pulse height distribution was verified against the simulation. The point at $v = \frac{1}{2}\frac{d'}{t'+d'}$ coincides with the point of discontinuity of the derivative seen in the figure. The match between expression and simulation below this point is exact.

For pulse amplitudes larger than $\frac{1}{2}\frac{d'}{t'+z'}$ the condition that $u_+ < z' + d'$ translates to $z' < d'(\frac{1}{2v} - 1)$. There are now two constributions, the second arising for $d'(\frac{1}{2v} - 1) \leq z' < t'$.

$$\begin{aligned} P(\hat{V}_{2b_2} < v) &= \frac{d'}{t'}\left(t' - d'\left(\frac{1}{2v} - 1\right)\right) + \frac{1}{t'}\int_0^{d'(\frac{1}{2v}-1)} dz' \left[vd' + \sqrt{2vd'z' + v^2d'^2}\right] \\ &= d' - \frac{d'^2}{6t'}\left(\frac{1}{a} - 3 + 4a^2\right) \\ p_{2b_2}(v) &= \frac{(1 - 8v^3)d'^2}{6v^2t'} \end{aligned}$$

The pulse height spectrum nicely corresponds to that simulated in the range $\frac{d'}{t'+d'} < v < \frac{1}{2}$. No larger pulse amplitudes are possible.

Fragments that do not strike the opposite electrode: charge collected on the opposite electrode, configuration 1. This case is the more interesting one, given that this is the configuration for which the least number of fission events

is lost below an amplitude threshold. It is also the case where, according to the simulation, a maximum occurs just below half the largest possible amplitude. In the new notation the pulse amplitude is

$$\hat{V}_{1b} = \frac{1}{2ud'}(u - z')(2d' + z' - u) \text{ for } z' < u < z' + d'.$$

In this notation it is evident that the amplitude is zero for $u = z'$ and for $u = z' + 2d'$. The first zero is physical and corresponds to fragments emitted at an angle for which they are just completely stopped in the deposit. The second is not since it occurs for fragments striking the opposite electrode. To see that a maximum occurs for each z', we can take the derivative with respect to u

$$\hat{V}'_{1b} = \frac{1}{2u^2d'}\left[z'^2 + 2z'd' - u^2\right] \text{ for } z' < u < z' + d'.$$

The derivative is zero for $u_{\max} = \sqrt{2z'd' + z'^2}$. For lower values of u the derivative is positive, showing the rise of the amplitude going from very tangential tracks to less tangential tracks. For larger values of u the derivative is negative showing the decline in amplitudes as a result of the lessening of the distance that the charge travels to the collecting electrode. This derivative can be used to obtain an expression for the pulse height distribution for a given z'

$$p_{1b}(v, z') = \frac{du}{dv} = \frac{1}{\hat{V}'_{1b}},$$

and from there for all $'z$

$$p_{1b}(v) = \frac{1}{t'}\int_0^{z'} dz' \frac{1}{\hat{V}'_{1b}}.$$

However, to proceed in this way it is necessary to express u in terms of $\hat{V}_{1b}$ and in view of the maximum just discussed this inversion has two branches (it is not unique). For $v = \hat{V}_{1b}$ and fixed z' we have two solutions for u

$$u_{\pm} = z' + d'(1 - v) \pm \sqrt{d'^2(1 - v)^2 - 2z'd'v}.$$

These two solutions are shown in the figure together with the cosine limits and a line connecting the maximum amplitudes for given z'.

The figure makes clear that for each amplitude a range of (z', u) combinations contributes except for $v = 1$. A finite range implies a non-zero value of the pulse-height distribution at that amplitude and so the pulse-height distribution is zero

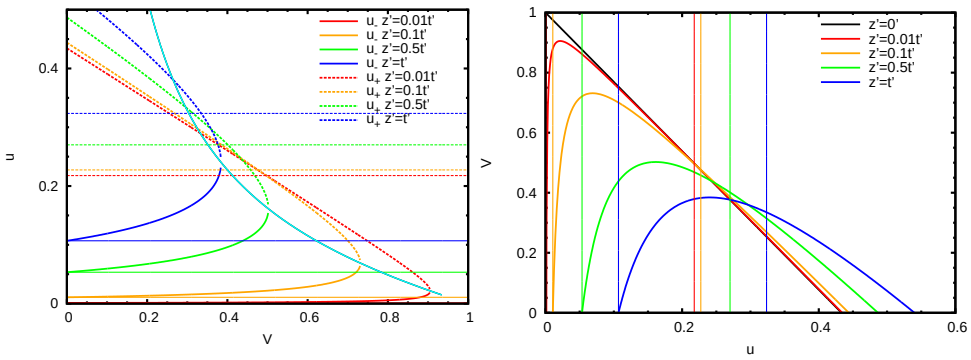

Figure 8: Cosine versus amplitude. For each z', the lowest (z') and highest ($z' + d'$) allowed cosines are shown in matching colors. The cyan line connects the maximum amplitudes.

only at the highest amplitude. Looking at u_- for a given z' shows that its contribution to the pulse height distribution increases up to the maximum pulse amplitude given by

$$v_{\max} = 1 + \frac{z'}{d'} - \sqrt{2\frac{z'}{d'} + \frac{z'^2}{d'^2}},$$

after which it is zero. However, this $v_{\max}$ ranges from a minimum corresponding to $z' = t'$ to a maximum of 1 corresponding with $z' = 0$. The u_- behavior by itself explains the low amplitude behavior of the pulse height distribution found in the simulation: non-zero value for $v = 0$ and a gradual increase towards larger v. It is also seen to contribute to a maximum and a gradual decrease at larger amplitudes. The behavior of u_+ is seen to give contributions to the pulse-height distribution from a certain minimum amplitude

$$v_{\min} = \frac{1}{2}\frac{d'}{d' + z'}$$

up to the maximum amplitude $v_{\max}$. The minimum amplitude is in the range from $\frac{1}{2}\frac{d'}{d'+t'}$ to $\frac{1}{2}$. From the minimum amplitude u_+ contributes to the rise of the pulse height distribution towards its maximum value that occurs for the $v = v_{\max}$ value with $z' = t'$.

Following up on the recipe described above, the contribution to the pulse height distribution from u_- is evaluated to be

$$p_{1b_1}(v) = \begin{cases} \frac{d'^2(1-v)^2(1+2v) - 3d't'v^2 - (t'v + d'(1-v)(1+2v)\sqrt{d'^2(1-v)^2 - 2d't'v}}{3v^2t'}, & v < 1 + \frac{t'}{d'} + \sqrt{2\frac{t'}{d'} + \frac{t'^2}{d'^2}} \\ \frac{d'^2(2-3v+v^3)}{6v^2t'}, & v \geq 1 + \frac{t'}{d'} + \sqrt{2\frac{t'}{d'} + \frac{t'^2}{d'^2}}. \end{cases}$$

Similarly, the contribution from u_+ can be evaluated (the absolute value of the derivative should be used)

$$p_{1b_2}(v)=\begin{cases} 0, & v<\frac{1}{2}\frac{d'}{d'+t'} \\ \frac{3d't'v^2+d'^2v^2(3-2v)-(t'v+d'(1+v-2v^2))\sqrt{d'^2(1-v)^2-2d't'v}}{3v^2t'}, & \frac{1}{2}\frac{d'}{d'+t'}\le v<1+\frac{t'}{d'}+\sqrt{2\frac{t'}{d'}+\frac{t'^2}{d'^2}} \\ \frac{d'^2(3-v^2)}{6vt'}, & 1+\frac{t'}{d'}+\sqrt{2\frac{t'}{d'}+\frac{t'^2}{d'^2}}\le v<\frac{1}{2} \\ \frac{d'^2(1-v)^2(2+7v)}{6v^2t'}, & v>\frac{1}{2}. \end{cases}$$

Finally, these two contributions must be combined to give

$$p_{1b}(v) = p_{1b_1}(v) + p_{1b_2}(v).$$

Again a nice match of the analytic and simulated results is shown.

References

[1] D. B. Gayther, International intercomparison of fast neutron fluence-rate measurements using fission chamber transfer instruments, Metrologia 27 (1990) 221.

[2] G. W. Carlson, The effect of fission fragment anisotropy on fission-chamber efficiency, Nucl. Instrum. Methods Phys. Res. 119 (1974) 97.

[3] C. Straede, C. Budtz-Jörgensen, H. Knitter, ^{235}U(n,f) fragment mass-, kinetic energy- and angular distributions for incident neutron energies between thermal and 6 MeV, Nucl. Phys. A 462 (1987) 85.

[4] S. S. Kapoor, The ^{235}U fission fragment anisotropies, Nuclear Data Standards for Nuclear Measurements, Technical reports series nr. 227, International Atomic Energy Agency, Vienna, ISBN 92-0-135083-X (1983).

[5] J. F. Ziegler, J. Biersack, M. Ziegler, SRIM The stopping and range of ions in matter, www.srim.org, SRIM Co., Chester, MD 21619, USA, ISBN 0-9654207-1-X (2008).

[6] Budtz-Jörgensen, H. Knitter, Assaying targets for nuclear measurements with a gridded ionization chamber, Nucl. Instrum. Methods Phys. Res. 236 (1985) 630.

4. Fission chamber measurements 27 July to 5 August at the VdG

Arjan Plompen

December 19, 2011

Abstract

Measurements of fission spectra were made for a single deposit in parallel plate configuration. Positive and negative voltage was applied to the opposite electrode that was also the readout electrode. Results were normalized to a second parallel plate detector in the same chamber but with independent electronics. The total number of fragments depositing energy in the counter gas was estimated by linear extrapolation to zero from the valley between the alpha-particle+noise and the main fission peak. The uncertainty of this number was often better than 1% but variations up to about 2% are possible. A clearly lower number of events of about 4.4(6)% was found for negative voltage. This seems to confirm expectations from a simple model and from GEANT4 simulations that for low amplitudes and negative voltage an excess over the estimate with linear extrapolation should be present. Implications for the efficiency of the FC@FP3/200m are discussed.

Independently, measurements were made of the alpha spectra with the same parallel plate detectors for deposit #8, #11 and FC@FP3/200m. The measured activities were 5.93(4) *kBq*, 2.985(10) *kBq* and 26.6(2) *kBq*. The agreement with the activities determined using low-geometry alpha counting is remarkable (5.92(3) *kBq*, 2.980(13) *kBq*, and 26.88(5) *kBq*).

1 Goal

1. To study the impact of reversing the polarity of the high voltage on the pulse height distribution.
2. To determine if the amount of fragments lost under the threshold may exceed the value determined from extrapolation.
3. To determine the sensitivity of the estimate of fragments lost under the threshold to the procedure and to neutron energy.

4. To infer a new best value for the efficiency of the FP3/200m fission chamber for the purpose of publications of Pb-206 and Fe-56.
5. To help out with consolidating an efficiency for the fission chamber in FP16/30m.

2 Background

For a fission chamber with many deposits (8 or 10) it is not practical to configure them all with a Frisch-grid due to space limitations. Using a Frisch-grid is advantageous since this would give near perfect amplitude resolution and as a consequence a small fraction of events lost under the threshold. In addition the combination of grid and anode signals could be used to reduce the contribution of alpha particles. Finally, there is good reason to believe that the pulse height distribution for small amplitudes is nearly flat, so that an extrapolation to zero amplitude would result in a reliable estimate of the number of undetected signals.

On the other hand parallel plates have been used for accurate work at the level of a few percent of accuracy on the inferred cross section or fluence, according to the application. Typically, they are operated at 1 atm with P10 gas (90%Ar and 10% CH_4) with an electrode gap of several mm which is well below the range of fission fragments (about 30 mm). The voltage is in the range of one to several hundred V/cm.

The pulse height distribution differs if the electrons produced by the fragments in the counter gas are collected on the electrode opposite to the deposit or on the deposit itself. This was clearly illustrated by the GEANT4 simulations of Jean-Claude Thiry and the measurements performed with the fission chamber of FP16/30m. It is once more clearly established by the measurements shown below. On the other hand no quantitative agreement was obtained between the GEANT4 simulations and the measured pulse height distributions, in particular in the range of small amplitudes. Since this is the range that is important for estimates of the number of fragments lost under the pulse height threshold and therefore of the efficiency of the chamber, several questions remain.

The main point is whether the pulse height distribution just above the threshold may be extrapolated linearly to zero amplitude. From the GEANT4 simulations it seemed that this is fine for electrons collected on the opposite electrode. However, this was shown not to be the case for electrons collected on the deposit.

For a very simple model the same generic behaviour is found. Take a single fission fragment with one energy E_0, emitted from a uniform layer with uniform cosine (u) distribution. Assume the range in the deposit is given by $R_d(E) = R_d \cdot E/E_0$ (here R_d is 4.7 mg/cm^2) and the range in the

gas by $R_g(E) = R_g \cdot E/E_0$ (here R_g is 30 mm). Assumer further that the charge is deposited uniformly along the track and that the electric field is constant. Fission takes place for a given depth z in the deposit. For given z and u the induced voltage may be determined analytically. Sampling z and u a spectrum may then be generated (see figure 1, for an 0.5 mg/cm^2 deposit and a 6.5 mm gap between the electrodes).

This model has qualitative features similar to those observed for a real spectrum when the electrons are collected on the opposite electrode. For the other case (electrons collected on the deposit) the similarity is not at all obvious. More realistic energy loss calculations and fission fragment distributions are required for that case as was shown with the GEANT4 simulations. Nevertheless, the low amplitude behaviour which is determined by fission fragments stopped in the gas is very similar. It emphasises the generic differences between the two configurations:

1. In case, the electrons are collected on the electrode opposite to the deposit, the number of low amplitude events is significantly less than for the case with electrons collected on the electrode with the deposit.
2. In case, the electrons are collected on the opposite electrode, the low amplitude behaviour is very nearly linear, with a slight positive slope and a non-zero value for zero amplitude.
3. In case, the electrons are collected on the electrode with the deposit the low amplitude behaviour is basically non-linear, down sloping, and progressively increasing for decreasing amplitudes.

For the last point it may be argued that the behaviour is still nearly linear for most of the range and that the upturn for the lowest amplitudes does not affect much the total area under the curve. However, given the qualitative nature of the models an experimental verification would be very welcome, since this configuration is used in the past and applies still to the fission chamber of FP3/200m (GAINS setup).

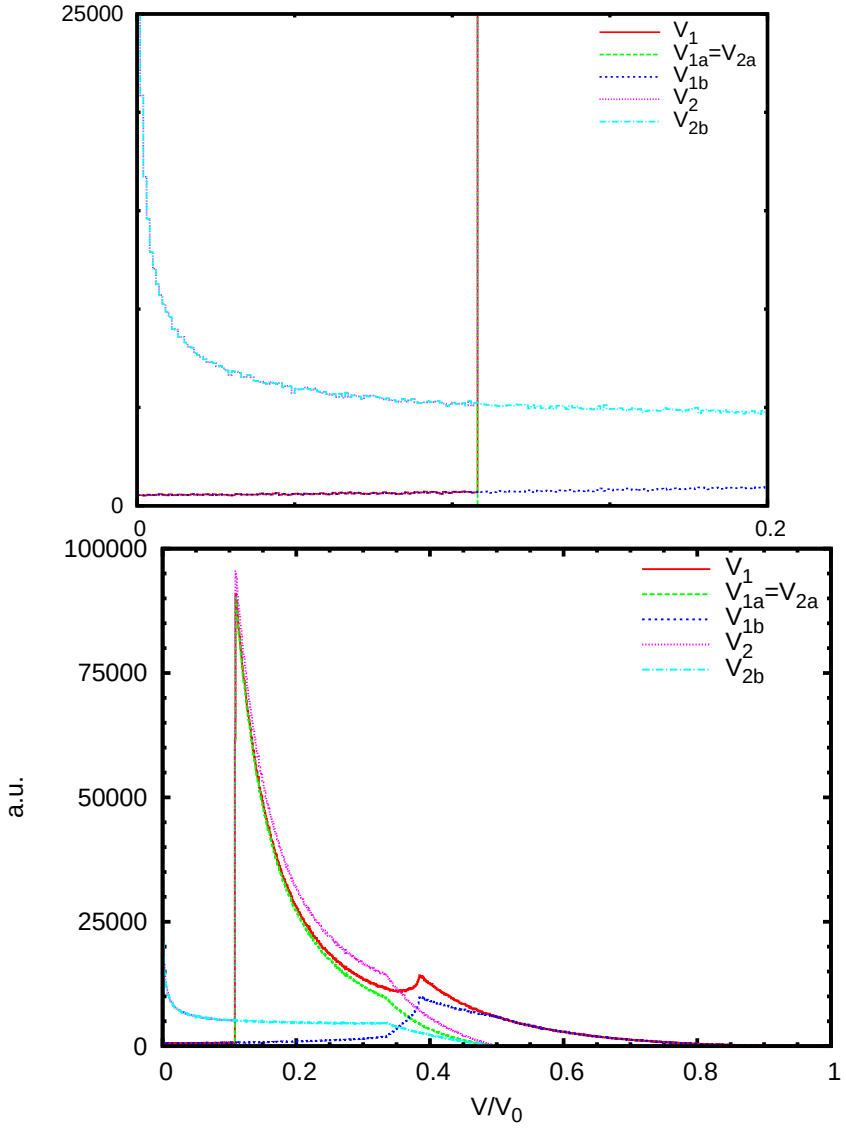

Figure 1: Simple model for the pulse height. For configuration 1 electrons are collected on the electrode opposite the deposit. For configuration 2 electrons are collected on the deposit. The labels 1a and 2a refer to the contributions from fragments stopped on the opposite electrode, while 1b and 2b result from fragments stopped in the gas. The top panel highlights the small amplitude range. The maximum attainable voltage is V_0.

Table 1: Beam energies and run numbers. With beam off a number of alpha spectra measurements were made.

$E_n(0°)$	$E_n(125°)$	Runs E_n
1.3	0.26	12, 13
1.8	0.42	3, 8, 9
2.0	0.49	1
4.5	1.3	2, 5
5.0	1.5	4
5.5	1.6	6, 7, 10, 11
-	-	14-21

Table 2: Metrological data from low-geometry alpha-counting and isotope mass spectrometry (Luyckx-Moens-Schillebeeckx, IRMM 2008). The deposits were prepared from Lot 680 by transformation from UO_2 to UF_4 and vapour deposition.

deposit	activity (Bq)	thickness $\mu g - U/cm^2$
#11a	2980(13)	475(2)
#8a	2963(14)	472(2)
#8b	2954(14)	471(2)

3 Measurements

A simple test was made using neutrons produced at the IRMM VdG for another experiment. The fission chamber of FP3/300m was placed at 1.25(2) m from the target of beamline R3 at an angle of about 125(2) degrees. Neutrons were produced by the T(p,n) reaction using target IRMM31, 2.2 mg/cm^2 Ti on a gold backing (T/Ti 1.7).

The fission chamber consists of two independent units with separate electronics. For both units the deposits are connected to ground and the preamp is connected to the electrode opposite the deposit. High voltage is supplied via the preamp so that a positive voltage corresponds with collecting electrons on the opposite electrode and a negative voltage corresponds with collecting electrons on the electrode with the deposit.

The deposits are #11 and #8 of LOT680C. The metrological data for the deposits are given in table 2. The latter is double sided and it was sandwiched between two electrodes that were connected electrically (to the preamp). The gap on both sides was 6.5 mm. The first (#11) is single sided. Here too the gap is 6.5 mm.

For the unit with the double sided deposit (#8), conditions were kept as

constant as possible. A positive high voltage of 206 V was applied. This unit serves as a monitor. A test pulse was applied to allow for a determination of the deadtime and of the offset in the spectrum.

For the unit with the single sided deposit (#11), the polarity of the high voltage was changed but the value was kept constant (206 V). Several polarity reversals were made. Otherwise the unit was treated in the same way as the other (electronics). Here too a test pulser was used. Of course changing the high voltage requires changing the input polarity of the spectroscopic amplifier and of the test pulser.

To determine the deadtime the test pulses were counted independently. The deadtime for the fission spectrum measurements was quite negligible (<0.2%) and will not be discussed further.

For the measurements looking for the alpha spectrum (runs 14-21) a much higher gain was used, the shaping constant was 0.25 μs and ADC zero and lower-level discriminators were adjusted. In particular, the pulser could not be connected to the test input without a significant deterioration of the noise and a deadtime of 30%. Instead, the pulser was applied to the input of the SA to measure the offset of the combination SA+ADC.

4 Results

4.1 Typical spectra

Typical spectra from the single deposit #9 are shown in figure 2 for neutron-induced fission and in figure 3 for the alpha-activity (beam-off).

For the fission spectra the result with positive high voltage is remarkably similar to the corresponding spectrum of the simple model above. In contrast, the spectrum with negative voltage shows no similarity whatsoever. True, the maximum amplitudes for the negative voltage are clearly reduced compared to those with positive voltage and perhaps the maximum amplitude for the former is indeed close to about half the maximum amplitude of the latter. Also, the nearly flat range below the peak of the spectrum is clearly significantly lower for positive voltage than for negative voltage and perhaps also the slopes appear to correspond to those of the model. On the other hand there is no component that is the same in the two spectra, quite contrary to expectation. Finally, the double-humped structure for negative voltage could never be explained by the simple model above.

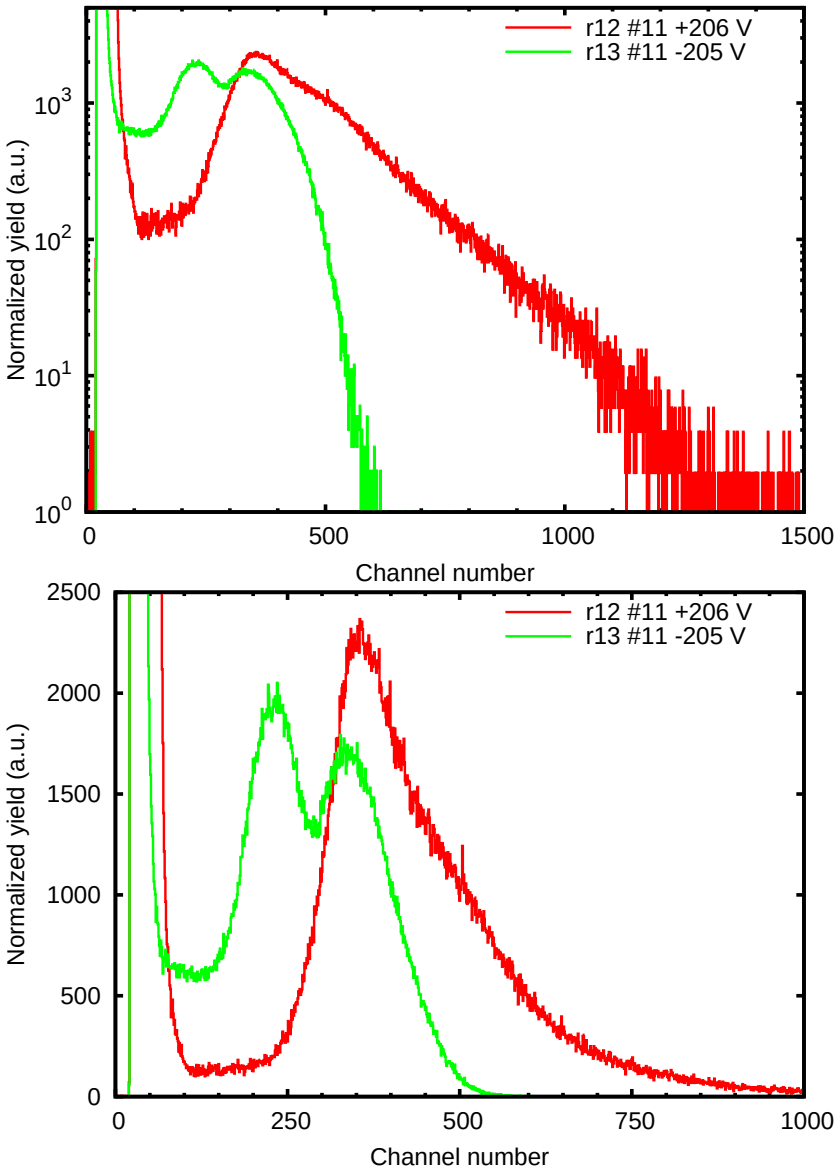

Figure 2: Typical spectra for single-sided deposit #9 (ADC3). These data were taken from runs 12 (r12) and 13 (r13). They have been normalized to 1M fission events of #8 (ADC4). Spectra with 8192 channels were rebinned to 2048 channels.

Table 3: SRIM2008 data for the deposits. The mean energy and standard spread of the alpha energy was deduced from decay data on the LNHB webpage. The activity ratio was determined using the same decay data and isotope ratio measurements by Stephan Richter. On the last line the fraction of alphas lost in the deposit is given as an average over the two activities. Assuming 10% accuracy on the range this number should carry two digits.

isotope	A	$\overline{\overline{E_\alpha}}$	R(P10)	R(UF4)	$t(\#8)/2R$	$t(\#11)/2R$
	(%)	(MeV)	*mm*	μm		
^{234}U	50.8	4.84(3)	34.7	13.7	0.0341	0.0343
^{235}U	49.2	4.47(8)	39.0	15.2	0.0308	0.0307
					0.0325	**0.0323**

In contrast, the alpha spectra agree qualitatively very well with the model. The main component is indeed very similar. There is a secondary maximum for positive voltage. The spectrum for negative voltage falls off progressively to zero near this secondary maximum. Finally, the levels at low amplitude are in relative magnitude comparable to those of the model. The only point seems to be the slopes of those levels, which are both negative in this case.

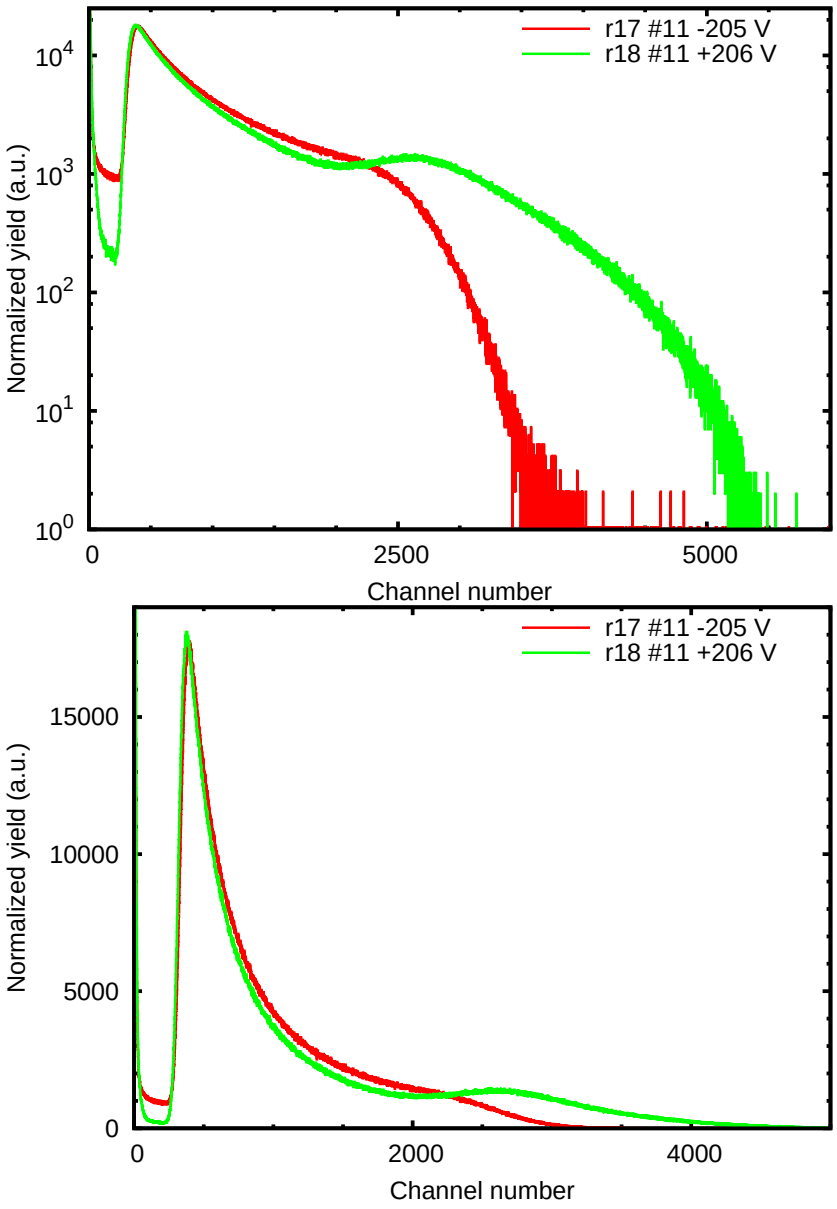

Figure 3: Typical alpha spectra for single-sided deposit #9 (ADC3). These data were taken from runs 17 (r17) and 18 (r18). They have been normalized to 7200s.

4.2 Detailed analysis of the alpha spectra

Given the surprising result that the alpha spectra are close to expectation, it is worthwhile to find out how much may be learned from these.

First, we may verify why the above model is so close to the alpha results. The following table shows data from SRIM, the isotopic measurement results and decay data tables from LNHB. About 50% of the activity of the batch is due to ^{234}U. Obvious differences are the 35-50% longer range in the deposit. As a consequence the fraction of alphas lost in the deposit is less. Furthermore the range in the gas is 17-25% longer. Also the spread in alpha-energies is only about 8%, so that the mono-energetic assumption is pretty good for data taken with a parallel plate ionization chamber. So, all-in-all this is still pretty close to the numbers used for figure 1 above.

Second, it is interesting to see if the total number of counts is in agreement with the measured activity. To deduce the activity the following approach was taken to estimate the number of events. A threshold C was determined (see below) and the total counts Y above this threshold was determined from the spectrum. To Y one has to add Y_A, the number of events depositing charge in the counter gas, but with amplitudes below C and Y_B, the number of alphas stopped in the deposit. The activity was then given by (T is the measurement time.

$$A = 2\frac{Y + Y_A + Y_B}{T}. \tag{1}$$

In practice, Y_B is estimated from the simple expression

$$\frac{Y_B}{Y + Y_A + Y_B} = \frac{\overline{t}}{2R}. \tag{2}$$

Here, $\overline{t/2R}$ is the mean fraction of alphas stopped in the deposit. It was obtained as described in table 3. Therefore the analysis used the following expression for the activity:

$$A = 2\frac{Y + Y_A}{T}\frac{1}{1 - \frac{\overline{t}}{2R}}. \tag{3}$$

For the uncertainty, it was assumed that the range has a 10% uncertainty, implying 0.3% uncertainty (table 3) for the factor $1/(1 - \overline{t/2R})$.

The procedure for Y and Y_A was the following. A linear fit $l(ch) = a \cdot ch + b$ was made to the plateau in the low amplitude region between channels L and H. The values for these channels were picked in such a way as to be free from noise and free from the rising edge of the mean peak. Since there is some arbitrariness different choices were made. For the fit the data were weighted with the uncertainty squared so that a proper chi-square was used. From the fit the parameters a, b, their uncertainties $u(a)$ and $u(b)$

and the correlation coefficient C_{ab} were obtained. Then the central channel $C = (L + H)/2$ of this range was obtained and served as threshold.

The number of counts Y_A from the offset O to channel C was determined with the expression

$$Y_A = \frac{a}{2}\left(C^2 - O^2\right) + b(C - O). \tag{4}$$

The uncertainty for this expression was given by

$$u^2(Y_A) = \left[\frac{u(a)}{2}\left(C^2 - O^2\right)\right]^2 + [u(b)(C - O)]^2 + \frac{u(a)}{2}\left(C^2 - O^2\right)u(b)(C - O)C_{ab}. \tag{5}$$

The offset was determined experimentally with about 10 channels uncertainty. The latter was not propagated.

The results are shown in table 4. The fraction $Y_A/(Y_A + Y)$ is less than 1% for positive voltage and about 3% for negative voltage. The number of fragments lost in the deposit Y_B is about 3% and is the main correction and source of uncertainty. The activity determined here compares extremely well with the reference activity determined by low-geometry alpha counting. The final uncertainty is impressive and appears credible. The slightly low value for deposit #8 is not the result of the fit interval and it has been checked that also the 10 channel uncertainty of the offset is not important. It could be due to deadtime (see below). The three sigma lower value for the one case with negative voltage could be an indication of an excess component for very low amplitudes, as suggested by the model and GEANT4 simulations; i.e. of a contribution in excess of that obtained by linear extrapolation to zero. However, the effect is small (1.4%).

It may be noted that no count loss correction could be applied since no pulser could be connected to the test input without creating a large deadtime and spoiling the low amplitude behavior. Instead, initially (run16) deposit #8 was kept at low amplification resulting in practically no contribution to the data rate. For runs 18 and 19, the amplification for both was high. Adding #8 implied a three times higher count rate. Comparing the results of runs 16 and 18 (or 19) for #11 shows no difference for the final activity. The deadtime may be estimated by the pulse rise time (0.7 μs), the ADC conversion time (0.8 μs) and the actual count rate (4400cps). It is at most 0.66%. Due to the use of non-coincidence mode the deadtime should be independent for the two FCs as a result of buffering at the level of the multiplexer (0.22% for #11 and 0.44% for #8). These values are close to the measurement uncertainty, so for accurate work it would be beneficial to reduce deadtime further or measure it properly.

Table 4: Data analysis results for the alpha spectra. Correlation coefficient $C_{ab} < -0.982$. The reference activities were determined by low-geometry alpha-counting at IRMM (table 2 above). Activities from runs 20 and 21 were corrected for deadtime (relevant for #8).

run	V	FC	L	H	C	a	b	O	Y_A
16	206	#11	100	200	150	-0.50(5)	226(7)	-105	54792(1731)
17	-205	#11	100	200	150	-1.5(1)	1172(17)	-105	290646(3983)
18	206	#11	150	200	175	-0.43(13)	293(22)	-105	77671(5774)
19	206	#11	220	300	260	-0.38(6)	305(15)	0	66412(3427)
20	206	#11	200	250	225	-0.5(2)	354(34)	0	67306(6643)
21	206	#11	200	300	250	-0.38(5)	309(12)	0	65259(2530)
18	206	#8	130	180	155	0.3(2)	446(32)	-160	140211(10041)
19	206	#8	300	350	325	0.7(2)	222(60)	0	108219(17028)
19	206	#8	310	340	325	0.7(4)	222(123)	0	107705(34619)
19	206	#8	310	326	318	-0.1(1.0)	471(311)	0	144448(85648)
20	206	#8	300	320	310	-5(1)	2445(479)	0	505252(128596)
21	206	#8	340	360	350	-0.6(9)	838(328)	0	258225(99359)

run	V	FC	Y	$Y + Y_A$	T (s)	A (Bq)	A/A_{ref}
16	206	#11	6989725	7044517	4878	2985(10)	1.002(6)
17	-205	#11	9534794	9825440	6916	2937(10)	0.986(5)
18	206	#11	10325944	10403615	7200	2987(10)	1.003(6)
19	206	#11	10316243	10382655	7200	2981(10)	1.001(6)
20	206	#11	10329751	10397057	7200	2985(10)	1.002(6)
21	206	#11	10333675	10398934	7200	2985(10)	1.002(6)
18	206	#8	20336482	20476693	7200	5878(20)	0.993(6)
19	206	#8	20339428	20447647	7200	5870(20)	0.992(6)
19	206	#8	20339428	20447133	7200	5870(22)	0.992(6)
19	206	#8	20342461	20486909	7200	5881(32)	0.994(7)
20	206	#8	20309359	20814611	7200	5974(42)	1.010(9)
21	206	#8	20315179	20573404	7200	5904(35)	0.998(8)

4.2.1 Alpha spectrum of the FC in FP3/200m

Given the success of the activity determinations for foils #8 and #11, it seems interesting to see what can be said about the FC used for GAINS. In run 20, this fission chamber was added on ADC2 and first tests showed it was usable after one night of flushing with P10. Due to the much higher activity deadtime will be non-negligible and due to the higher capacitance the noise level is much worse. To monitor deadtime the output of the preamplifiers of #8, #11 and FC@FP3/200m were or-ed (CAEN N625) with the pulser before connecting to the spectroscopic amplifier. The or-unit has four sections. The first was used to branch out the pulser to the other three units. To each of the three a preamp was added (control room). This somewhat increased the noise level for #8 and #11 and the llds were adjusted to lower deadtime.

Data from run 20 showed deadtimes of 0.71%, 0.04% and 2.8% for #8, #11 and FC@FP3/200m. Unfortunately, the added noise from the pulser gave different results for the final activity of #8 (but not for #11). In the spectrum of FC@FP3/200m there was no plateau, just a minimum. Using the three channels around the minimum to determine the activity in the same manner and correcting for the dead time and the loss of fragments in the deposit (2.6% of the total) the activity is 27.2(3) kBq. From the data sheets of the chamber the activity is 26.88(5) kBq. These numbers agree within the uncertainty of 1.3% of the present measurement.

In run 21 the pulser was removed and the preamp signals were directly connected to the spectroscopic amplifiers. Indeed the noise was reduced resulting in a lower minimum between the noise and the main peak. As a consequence the contribution of Y_A dropped from 5.6% for run 20 to 3.2% for FC@FP3/200m and the resulting activity was 26.6(2) kBq. This number differs about 2 standard deviations from the above value of 27.2(3) kBq from run 20. Since the sum over the counts above threshold differs by only 0.3% between runs 20 and 21, this is entirely due to the estimates for Y_A. However, even if the uncertainty for the present estimates is somewhat understated due to a problem with the noise level, the final conclusion is that we have a remarkably accurate verification of the total activity in the chamber.

5 Fission spectrum measurements

Tables 5-8 show the results of estimating the amounts Y_A and $Y + Y_A$ for the fission spectra. For #11 (ADC3), the results are shown in tables 5, 6 and for #8 (ADC4) in tables 7, 8. In table 9 normalized results are shown with #8 taken as the reference.

The same procedure was followed as for the alpha spectra, but no estimate was included for the amount Y_B of fission fragments stopped in the deposit. Here the fits were always made on 2k spectra, obtained from re-

binning the 8k spectra acquired online. Typically three fits were made with a wide interval and the same interval split in two equal parts. Occasionally some additional/different choices for L and H were taken. The variation in limits allow to determine the sensitivity of the procedure for obtaining Y_A.

Several conclusions may be drawn from the tables. Considering first the tables that concern the fit (tables 5 and 7) and then the results concerning Y_A in relation to $Y + Y_A$ (tables 6 and 8).

1. More often than not the slope a does not differ significantly from zero. It is therefore not possible to conclusively decide which sign of slope corresponds to which voltage.
2. The offset b is not determined very precisely, despite the number of channels and often rather large value. It is very sensitive to the value of the slope and tends to go to unphysically low values (even negative) if the interval is chosen too close to the main peak in the spectrum. It is however clear that such low values for b and corresponding relatively large values for a should be discarded on account of the expected behaviour from the GEANT4 simulations and the model.
3. The more reliable results are from the wider fit intervals. Typically, the narrower intervals produce less accurate numbers that agree within uncertainty with the widest interval (for Y_A). Only for obvious unphysical results is this not the case. So, below we only discuss the results from the widest intervals.
4. The uncertainty for Y_A is always significant given the statistics. Only for the longest runs, uncertainties better than 10% are obtained. Mostly, one must be satisfied with a number on the level of 25%.
5. The fraction $Y_A/(Y_A + Y)$ is about 4% for positive voltage and about 15% for negative voltage.
6. In most cases the uncertainty for $Y + Y_A$ is 1% or better. However, the variability with the fitting interval (column dev. in tables 6,8) is somewhat larger: about 2%.

This final point is rather positive.

To determine the impact of the polarity of the voltage, table 9 shows the ratio of $Y + Y_A$ for #11 to that of #8. In itself this ratio is not so meaningfull since we know that the counts of #8 cannot be scaled to the position of #11. In earlier work we found that $1/r^2$ is violated badly by a large constant component in case a DC neutron field is used at the VdG laboratory. Nevertheless, as a monitor #8 is very stable as can be seen in the table. A clear grouping of results is observed (see also figure 4). For negative voltages this is somewhat spoiled by run 13 that appears as an outlier. Positive voltages average 0.548(2) and negative voltages without run 13 average 0.515(2) (unweighted means). The ratio of negative to positive is 0.957(6). It would

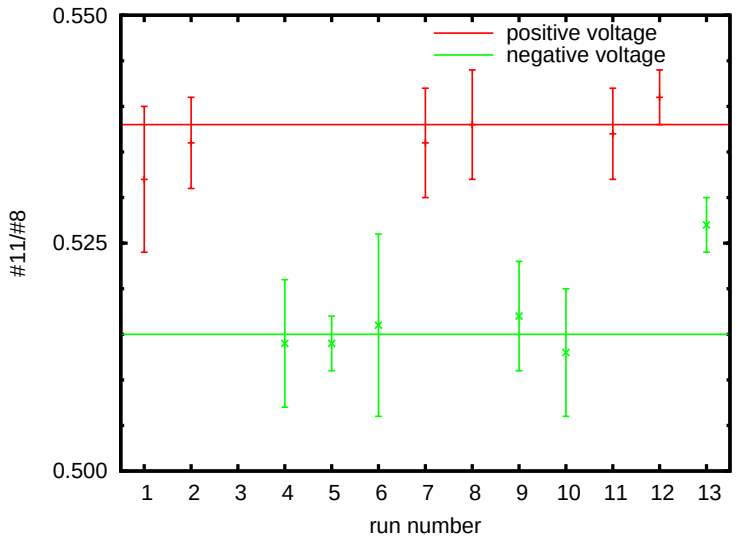

Figure 4: Ratio of $Y + Y_A$ of #11 to that of #8. A clear grouping of the results for positive and negative voltage is observed. The mean for each is indicated (excluding run 13) by the horizontal lines.

appear that this confirms that linear extrapolation underestimates Y_A in the case of negative voltage and that about 4.3(6)% of the total number of events are in the component of excess above the linear extrapolation.

So, we conclude that no significant differences are observed that might have resulted from the use of different neutron energies (here for the range $E_n = 0.2-1.6\ MeV$). However significant differences are observed changing the polarity of the voltage and the effect the missing fraction for negative voltage is 4.3(6)%. Finally, the 1-2% uncertainty for $Y + Y_A$ for the applied procedure is good news. However, the uncertainty is associated with the applied procedure and it would have to be applied to the fission chamber data of the GAINS setup in retrospect to correct the data accordingly. For the GAINS setup only half the fission fragments see a negative electric field compared to their point of origin and therefore a linear extrapolation misses out on 2.2(3)% of the total number of fragments entering the counter gas.

Table 5: Results for #11/ADC3. The correlation coefficient was $C_{ab} < -0.988$. The offset O was -17 for runs 1 and 2 and -15 for the remaining runs

run	$V(V)$	L	H	C	a	b	Y_A	$u(Y_A)/Y_A$
1	+206	150	200	175	0.02(3)	10(5)	2161	41%
		150	250	200	0.01(1)	11(3)	2562	21%
		200	250	225	0.08(4)	-6(10)	719	288%
2	+206	125	225	175	0.04(2)	19(3)	4237	11%
		125	175	150	0.04(5)	19(7)	3646	28%
		175	225	200	0.11(5)	3(9)	2994	57%
4	-205	80	140	110	0.12(8)	122(9)	15962	6%
		110	140	125	0.4(2)	88(24)	15341	19%
		80	110	95	-0.1(0.3)	144(24)	15286	15%
5	-205	82	142	112	0.1(2)	494(18)	63323	3%
		82	112	97	-1.0(4)	605(42)	62697	7%
		112	142	127	0.6(4)	441(44)	66876	8%
6	-205	80	140	110	-0.06(5)	53(5)	6272	9%
		80	110	95	-0.0(1)	51(13)	5432	23%
		110	140	125	-0.1(1)	51(17)	6778	30%
7	+206	110	210	160	0.05(2)	10(3)	2393	17%
		110	160	135	-0.02(4)	20(6)	2738	26%
		160	210	185	0.09(5)	3(10)	2104	83%
8	+206	115	220	168	0.06(1)	7(2)	2112	16%
		115	168	142	0.00(3)	15(4)	2402	24%
		168	220	194	0.11(4)	-3(7)	1566	85%
9	-205	80	145	113	0.03(8)	133(9)	17092	6%
		113	145	129	0.3(2)	98(23)	16463	17%
		80	113	97	0.0(3)	131(24)	14815	16%
10	-205	85	150	118	0.0(4)	61(5)	8124	7%
		118	150	134	0.2(1)	41(16)	7463	28%
		85	118	102	-0.2(1)	77(12)	8166	15%
11	+206	110	210	160	0.03(1)	10(2)	2066	14%
		160	210	185	0.09(3)	-2(6)	1131	94%
		110	160	135	0.03(3)	10(4)	1731	33%
12	+206	116	220	168	0.16(4)	44(6)	10262	10%
		168	220	194	0.2(2)	44(32)	12239	47%
		116	168	142	0.10(8)	52(11)	9172	17%
13	-205	80	130	105	-0.9(2)	710(21)	79816	3%
		108	135	122	-0.0(5)	608(60)	82310	9%
		80	108	94	-1.5(4)	758(42)	76020	5%

Table 6: Results for #11/ADC3, continued.

run	$V(V)$	L	H	Y	$Y + Y_A$	$\frac{u(Y+Y_A)}{Y+Y_A}$	$\frac{Y_A}{Y+Y_A}$	dev
1	+206	150	200	67833	69994	1%	3%	-0.04%
		150	250	67483	70045	0.8%	4%	0.04%
		200	250	67127	67846	3%	1%	
2	+206	125	225	109904	114141	0.5%	4%	0.5%
		125	175	110543	114189	0.9%	3%	0.6%
		175	225	109269	112263	2%	3%	-1%
4	-205	80	140	97630	113592	0.9%	14%	0.4%
		110	140	95585	110926	3%	14%	-2%
		80	110	99677	114963	2%	13%	2%
5	-205	82	142	366695	430018	0.5%	15%	-0.2%
		82	112	374160	436857	1%	14%	1%
		112	142	359062	425938	1%	16%	-1%
6	-205	80	140	33147	39419	2%	16%	0.3%
		80	110	33856	39288	3%	14%	-0.1%
		110	140	32441	39219	5%	17%	-0.2%
7	+206	110	210	67148	69541	0.7%	3%	0.01%
		110	160	67574	70312	1%	4%	1%
		160	210	66654	68758	3%	3%	-1%
8	+206	115	220	61183	63295	0.7%	3%	0.2%
		115	168	61604	64006	1%	4%	1%
		168	220	60710	62276	2%	3%	-1%
9	-205	80	145	96998	114090	0.9%	15%	0.8%
		113	145	94864	111327	3%	15%	-2%
		80	113	99179	113994	2%	13%	0.8%
10	-205	85	150	44850	52974	1%	15%	0.4%
		118	150	43855	51318	4%	15%	-3%
		85	118	45820	53986	2%	15%	2%
11	+206	110	210	57524	59590	0.6%	3%	0.7%
		160	210	57166	58297	2%	2%	-1%
		110	160	57897	59628	1%	3%	0.8%
12	+206	116	220	268890	279152	0.4%	4%	-0.1%
		168	220	266968	279207	2%	4%	-0.1%
		116	168	270648	279820	0.6%	3%	0.2%
13	-205	80	130	445912	525728	0.4%	15%	0.1%
		108	135	437514	519824	1%	16%	-1%
		80	108	454514	530534	0.8%	14%	1%

Table 7: Results for #8/ADC4. The correlation coefficient was $C_{ab} < -0.988$. The offset O was +4. The voltage was +206 V

run	L	H	C	a	b	Y_A	$u(Y_A)/Y_A$
1	145	195	170	-0.02(6)	37(11)	5857	27%
	146	196	171	0.02(7)	30(12)	5377	31%
	148	200	174	0.02(6)	30(11)	5459	29%
2	145	196	171	0.03(7)	50(12)	8792	19%
	148	200	174	0.03(7)	50(12)	8994	20%
	149	201	175	0.03(7)	50(12)	9066	20%
4	134	180	157	0.1(1)	52(15)	9015	22%
	136	183	159	0.1(1)	52(15)	9176	23%
5	132	178	155	0.0(2)	245(26)	37395	9%
	133	179	156	-0.1(2)	261(25)	38948	8%
6	130	180	155	0.01(4)	22(7)	3467	25%
	155	180	168	0.0(1)	22(21)	3756	80%
	130	155	143	0.0(1)	22(16)	3171	59%
7	130	180	155	0.16(7)	14(11)	5116	35%
	155	180	168	0.5(2)	-42(35)	67	7500%
	130	155	143	0.1(2)	20(23)	4053	68%
	130	200	165	0.14(4)	18(7)	4791	19%
8	130	190	160	0.06(4)	26(7)	4783	19%
	160	190	175	0.17(2)	5(19)	3564	88%
	130	160	145	0.0(1)	36(17)	4955	42%
9	130	200	165	0.23(5)	30(8)	7989	14%
	165	200	183	0.2(1)	30(24)	9211	40%
	130	165	148	0.2(1)	30(20)	6859	36%
10	130	210	170	0.08(3)	17(5)	4100	16%
	170	210	190	0.20(7)	-5(13)	2681	80%
	130	170	150	0.08(8)	18(12)	3557	42%
11	125	210	168	0.08(3)	20(4)	4387	14%
	168	210	189	0.15(8)	6(14)	3860	60%
	125	168	147	-0.07(6)	41(9)	5136	21%
12	130	210	170	0.43(7)	84(12)	20161	8%
	170	210	190	0.9(2)	2(30)	16234	30%
	130	170	150	0.2(2)	111(24)	18999	16%
13	130	200	165	1.1(1)	136(20)	36491	7%
	165	200	183	1.8(3)	1(60)	30263	31%
	130	165	148	1.1(3)	137(47)	31459	19%

Table 8: Results for #8/ADC4, continued.

run	L	H	Y	$Y + Y_A$	$\frac{u(Y+Y_A)}{Y+Y_A}$	$\frac{Y_A}{Y+Y_A}$	dev
1	145	195	125903	131760	1%	4.4%	0.3%
	146	196	125879	131256	1%	4.1%	-0.1%
	148	200	125784	131243	1%	4.2%	-0.1%
2	145	196	204053	212845	0.8%	4.1%	0.0%
	148	200	203885	212879	0.9%	4.2%	0.00%
	149	201	203828	212894	0.9%	4.3%	0.01%
4	134	180	211773	220788	0.9%	4.1%	0.00%
	136	183	211634	220810	1%	4.2%	0.00%
5	132	178	797175	834570	0.4%	4.5%	-0.1%
	133	179	796946	835894	0.4%	4.7%	0.1%
6	130	180	72910	76377	1%	4.5%	0.01%
	155	180	72600	76356	4%	4.9%	-0.01%
	130	155	73198	76369	2%	4.2%	0.00%
7	130	180	124573	128689	1%	3.2%	0.6%
	155	180	124069	124136	4%	0.1%	-3%
	130	155	125049	129102	2%	3.1%	0.9%
	130	200	125050	129841	0.8%	3.7%	1%
8	130	190	112892	117675	0.8%	4.1%	0.3%
	160	190	112368	115932	3%	3.1%	-1%
	130	160	113413	118368	2%	4.2%	0.9%
9	130	200	212648	220637	0.5%	3.6%	0.01%
	165	200	211363	220574	2%	4.2%	-0.02%
	130	165	213774	220633	1%	3.1%	0.01%
10	130	210	99132	103232	0.7%	4.0%	0.6%
	170	210	98499	101180	2%	2.6%	-1%
	130	170	99775	103332	1%	3.4%	0.7%
11	125	210	106499	110886	0.6%	4.0%	-0.05%
	168	210	105781	109641	2%	3.5%	-1%
	125	168	107160	112296	1%	4.6%	1%
12	130	210	495904	516065	0.4%	3.9%	0.3%
	170	210	492714	508948	1%	3.2%	-1%
	130	170	498914	517913	0.6%	3.7%	0.7%
13	130	200	960405	996896	0.3%	3.7%	0.4%
	165	200	953933	984196	1%	3.1%	-0.9%
	130	165	966549	998008	0.6%	3.2%	0.5%

Table 9: Normalized results.

run	V (V)	$Y + Y_A$ #11	$Y + Y_A$ #8	$\frac{\#11}{\#8}$
1	206	70045(594)	131760(1623)	0.532(8)
2	206	114141(581)	212845(1756)	0.536(5)
4	-205	113592(1028)	220788(2079)	0.514(7)
5	-205	430018(2029)	835894(3409)	0.514(3)
6	-205	39419(615)	76377(911)	0.516(10)
7	206	69541(489)	129841(997)	0.536(6)
8	206	63295(415)	117675(961)	0.538(6)
9	-205	114090(1052)	220637(1175)	0.517(6)
10	-205	52974(638)	103232(734)	0.513(7)
11	206	59590(377)	110886(686)	0.537(5)
12	206	279152(1125)	516065(1820)	0.541(3)
13	-205	525728(2237)	996896(2903)	0.527(3)
mean	206	655764(1584)	1219072(3379)	0.538(2)
mean	-205	1275822(3474)	2453825(5207)	0.520(2)
mean/w.o.13	-205	750094(2658)	1456929(4324)	0.515(2)

6 Implications for FP@FC3/200m efficiency

For fission measurements we can only discuss estimates for Y_A, the number of events depositing charge in the gas but below threshold. As already mentioned above for the GAINS setup, only half the fission fragments see a negative electric field compared to their point of origin and therefore a linear extrapolation misses out on 2.2(3)% of the total number of fragments entering the counter gas. This number could actually be a little smaller for other chambers since the measurements above were made for a layer with 475 μ^{235}U g/cm^2 while for instance the FC@FP3/200m chamber and the UF_4 deposit of the FC@FP16/30m have layers of 383 μ^{235}U g/cm^2. A simple scaling then gives 1.8(5)% for the additional number of fragments missed by the linear extrapolation (the uncertainty is enlarged since the number was not measured).

To follow the procedure advocated here would require going back to the pulse height spectra of the measurements concerned. This is complicated by the fact that in all earlier work the offsets of the spectra were not explicitly determined. Unfortunately, the relevance of this point was not realized before the July 2009 measurements described above and FC3@FP3/200m was not connected until after the beam was stopped. Therefore no fission spectra were determined with known offset.

Something useful may be learned from the data taken in the April 2009 runs at the VdG. Here we had pulsed beam and the time-of-flight data could be used to distinguish prompt neutron spectra from the continuous background due to moderated neutrons. This has the advantage that we can look at gated spectra corrected for the continuous background under the prompt time peak. Such spectra have a reduced contribution from alphas. Figure 5 shows the gated and the ungated spectra. Of course the gated spectrum has fewer counts, but rescaling shows that the spectra do not differ, except for low amplitudes. Clearly, analyzing both spectra in the minimum would give different estimates for the fraction $Y_A/(Y_A + Y)$ and the gated spectrum would provide the more reliable number.

Unfortunately, it appears easy to get an unphysical result (negative offset b). Using a rather narrow interval to fit the minimum the ungated spectrum has 8.6(2.8)% for $Y_A/(Y_A+Y)$ and the gated spectrum 7.5(2.5)%. So, despite the apparent differences in the spectrum there is no significant impact on Y_A. In both cases the uncertainties are 3% for the sum $Y + Y_A$, which is nearly exclusively the uncertainty due to estimating Y_A. Including an offset of -12 channels in the 2k spectrum leads to an increase of 0.5%, well within the uncertainty. It then appears that we do not have to worry too much about the offset, unless perhaps it could exceed 100 channels in an 8k spectrum. Note that the above 8% contribution for Y_A to $Y_A + Y$ is somewhat less than would be anticipated from the measurements for #11. The average over positive

and negative voltage for #11 is 9.5%. The small difference may be due to the slightly smaller layer thickness (507 $\mu g/cm^2$ vs 628 $\mu g/cm^2$).

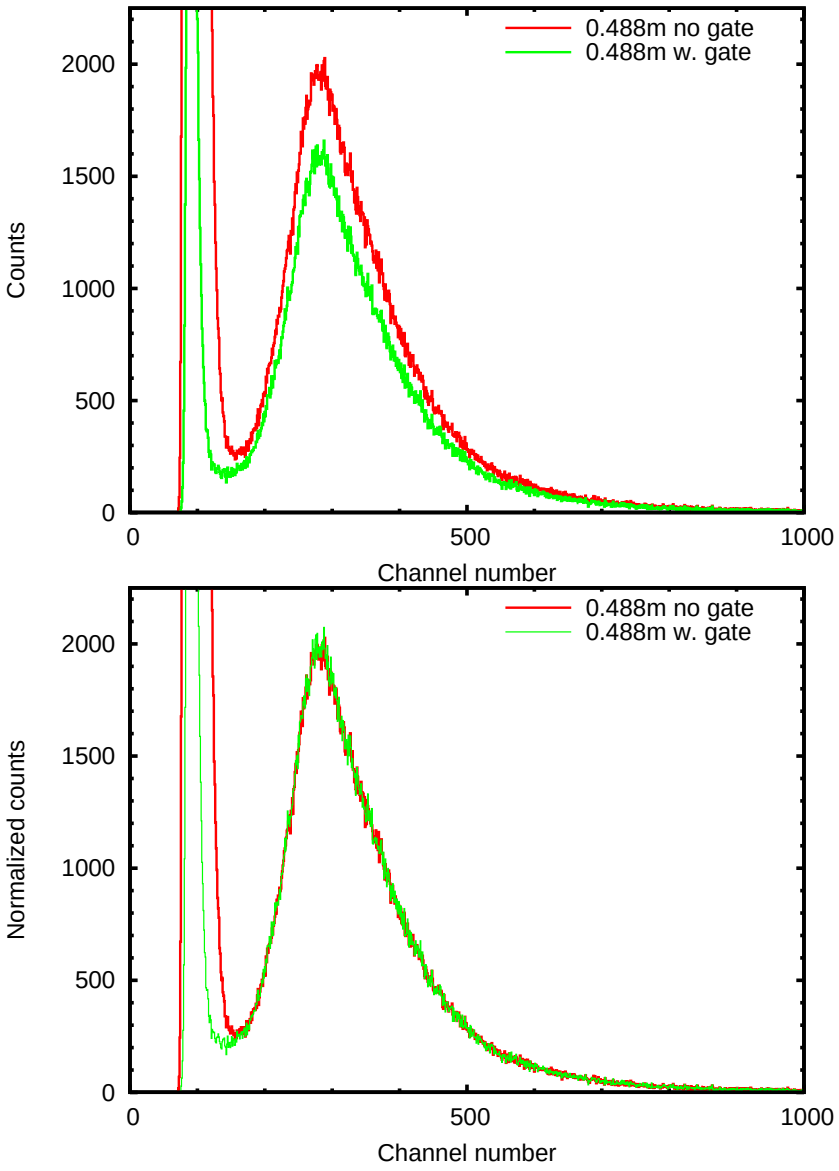

Figure 5: Pulse height spectra for FC@FP3/200m obtained at the VdG in April during measurements with pulsed beam. The data were rebinned to 2k from 8k spectra.

Conclusion It can be concluded that the procedure of linear interpolation can be followed, with a likely small additional uncertainty due to not having determined the offset. Two corrections are then needed for $Y + Y_A$ in order to obtain the total number of fission counts. The first concerns the correction for Y_B. Here for the moment all we have is $Y_B/(Y + Y_B + Y_A) = 0.105(7)t$ (t is total thickness in mg/cm^2) from the paper of Budtz-Joergensen. For #11 and #8 this is a correction of 6.6(4)%, while for FC@FP3/200m this is 5.3(4)%: we need to divide by 0.934(4) and 0.947(4), respectively. The second correction, for a chamber like FC@FP3/200m with equal deposits and equal number of fragments seeing the wrong field gradient, amounts to 2.2(3)% or division by 0.978(3). However, for the GAINS chamber itself 1.8(5)% is more appropriate due to the thinner layers in that chamber (correction factor 0.982(5)). From the above it would seem that the main uncertainty on the total number of fissions is from estimating Y_A. For the statistics shown here for the FC@FP3/200m this was 3%. Including the uncertainties for the above two effects does not change much the final uncertainty. Likely this is also true for the effect of an unknown offset.

6.1 Efficiency correction

In the paper of Mihailescu et al. [1] an efficiency of 0.984(16) is claimed. The procedure for determining it is given in the paper and it clearly does not correspond to the procedure advocated above. There is, however, sufficient detail in that paper to determine the efficiency that should have been used. It is therefore possible to correct the data that were analyzed with that procedure.

In the paper the area Y of the spectrum is taken above channel 850. A linear fit is made to a portion of the spectrum and is given as $y = -28.45 + 0.061x$. This linear fit cuts the horizontal axis (counts=0) at channel 466.4. The area under this curve between channels 466.4 and 850 is $A = 4488.2$. The efficiency is given as $0.984 = Y/(Y + A)$. This may be inverted to give $Y = 276024$ for the number of counts above threshold.

One may now apply the procedure above, approximately. An average height of 26(2) counts between channels 670 and 850 was determined using eight points from the graph in the paper. Extrapolating down to zero pulse height we find 22100(2210) counts between channel zero and 850. Here the uncertainty of 7% was augmented to 10% to account for not having determined the offset experimentally. The total number of fissions with pulse height comes to 303589(2782) with a correction factor of 1/0.982(5) for the polarity effect. The polarity effect of 2.2(3)% for FC@FP3/300m was lowered to 1.8(5)% to account for the lower thickness of the layers in FC@FP3/200m and the uncertainty was enlarged to account for not having determined this change experimentally. Finally, accounting for the loss of

fission fragments in the deposit, the total number of fissions for the spectrum in the paper is 320579(3235).

For the threshold of 850 channels this amounts to an overall efficiency of 0.861(9). Thus the cross sections determined by Mihailescu et al. must be multiplied with a factor of 0.875(10) to obtain the correct values. This correction should be applied to the data published for ^{52}Cr [2], ^{208}Pb [3], and ^{209}Bi [4].

References

[1] L. C. Mihailescu, L. Oláh, C. Borcea, A. J. M. Plompen, A new HPGe setup at Gelina for measurement of gamma-ray production cross sections from inelastic neutron scattering, Nucl. Instrum. Methods Phys. Res. A 531 (2004) 375.

[2] L. Mihailescu, C. Borcea, A. Koning, A. Plompen, High resolution measurement of neutron inelastic scattering and (n,2n) cross-sections for ^{52}Cr, Nucl. Phys. A 786 (2007) 1.

[3] L. C. Mihailescu, C. Borcea, P. Baumann, P. Dessagne, E. Jericha, H. Karam, M. Kerveno, A. J. Koning, N. Leveque, A. Pavlik, A. J. M. Plompen, C. Quétel, G. Rudolf, I. Trešl, A measurement of (n, xnγ) cross sections for ^{208}Pb from threshold up to 20 MeV, Nucl. Phys. A 811 (2008) 1–27.

[4] L. C. Mihailescu, C. Borcea, A. Koning, , A. Pavlik, A. J. M. Plompen, High resolution measurement of neutron inelastic scattering and (n,2n) cross-sections for ^{209}Bi, Nucl. Phys. A 799 (2008) 1–29.

5. Fission Chamber Measurements April 2009 Pulsed Beam

C. Rouki, A. Plompen, and M. Stanoiu

The fission chambers FC200 and FC300, installed respectively at the 200m and 300m stations of flight path 3, were used for further measurements at the Van De Graaff neutron beam. After the January 2009 runs showed a large background component in all measured neutron rates, a pulsed beam and the timing information of all data was used in the current measurements to reject events not originating from the direct beam.

The proton recoil telescope (PRT) was again used as a reference, with measurements taken at two distances from the source. Background measurements with the Ta foil inverted were made for both distances. For three runs the PRT was placed behind the fission chamber measuring simultaneously.

All measurements are expressed with reference to the long counter monitor.
The neutron beam energy was 2 MeV throughout the experiment.

Contents **page**

1. EXPERIMENTAL DETAILS

A. FC300

On opening FC300 in April 2009 it was confirmed that the distances between double-sided foil 8 and its two collecting electrodes were different, which had been evident from the double-humped shape of the pulse height distribution (Figure 1) of the January 2009 measurements (after the modification of 28/1/2009).
These distances were measured to be 6.8 mm and 7.5 mm respectively (Figure 2).

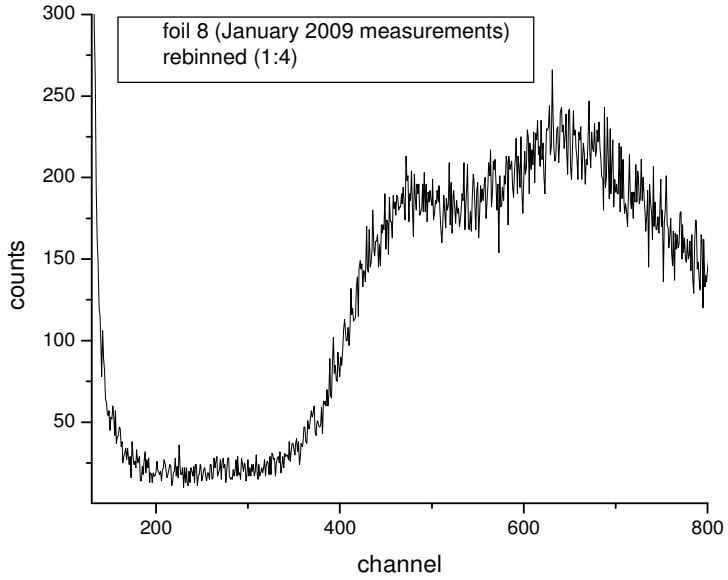

Figure 1: pulse height distribution from January 2009 measurements for double-sided foil 8 of FC300.

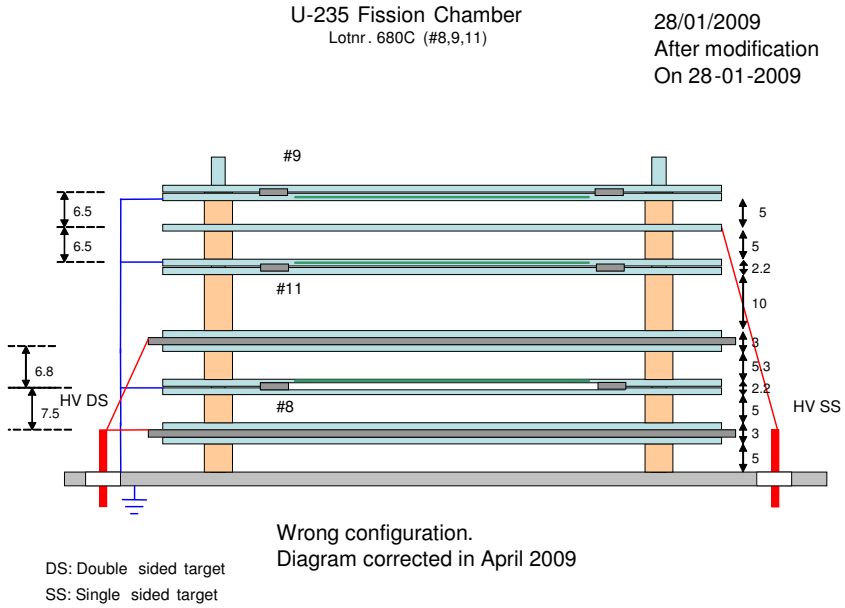

Figure 2: configuration of FC300 before April modification.

The configuration was modified and both distances were changed to 6.5 mm (Figure 3). The correction was confirmed by the shape of the pulse height distribution of foil 8 (Figure 4), where the double-humped structure has disappeared.

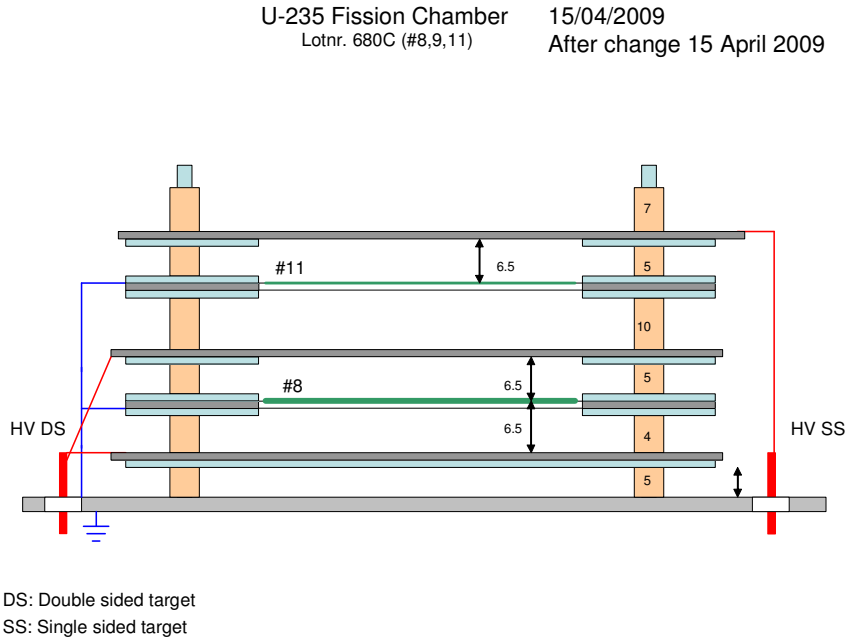

Figure 3: corrected configuration of FC300.

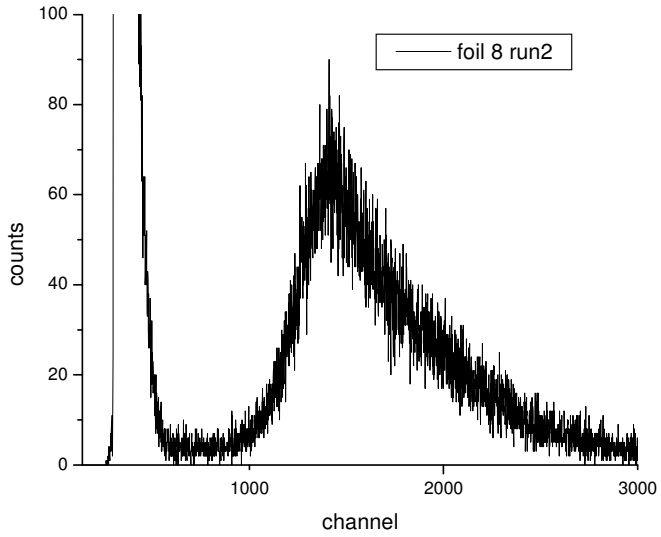

Figure 4: pulse height distribution from foil 8 after the correction.

From the single-sided foils, only foil #11 was used in the measurements, also at 6.5 mm from the collecting electrode.
The double-sided foil #8 was at distance 33 mm from the chamber's front window and the single sided foil 11 at 13.8 mm.

The following measurements were taken:

run	Run time (s)	foils	Distance source – front window (mm)	Description
1	145543	8,11	523	FC300
2	15509	8,11	231	FC300
7	15904	8,11	1089	FC300
8	50097	8	314	PRT behind FC300
9	4222	8	314	PRT (inverted) behind FC300

Table 1: FC300 measurements

B. FC200

The following measurements were taken with the 200m fission chamber:

run	Run time (s)	Distance source - centre of chamber (mm)	Description
12	62149	487.5	PRT behind FC200
14	90442	1015	FC200
17	89754	1504	FC200

Table 2: FC200 measurements

The data analysis for FC200 is based on the approximation that all UF_4 foils are situated in the centre of the chamber, which is considered at 12 mm from the front window.

C. PRT

The radiator foil was Tristearin 0.7476 mg/cm^2 thick (box 1/5) and the detector gas was 95% Ar and 5% CO_2 at 72 mbar. The following measurements were taken:

run	Run time (s)	Distance source – front plate (mm)	Description
3	37660	252	PRT
4	5567	252	PRT foil inverted
8	50097	740	PRT behind FC300
9	4222	740	PRT inverted & behind FC300
10	12675	740	PRT
11	3250	740	PRT
12	62149	740	PRT behind FC200
13	105799	740	PRT

Table 3: PRT measurements

During the first 7 cycles of run 3 the long counter monitor was very unstable and these files were rejected – the run time shown in the table corresponds to cycles 8-28.
Run 4 was used to estimate the background at 252 mm in spite of its low statistics.

Runs 8 and 9 were measured to have very large dead times (>11%) and introduced significant uncertainties in the results, so they were rejected for the largest part of the analysis. They were only used for the estimation of the background at 740 mm and of the effect of FC300 on the PRT measurement.

D. Long counter monitor

During some runs the long counter monitor showed very large noise in the low amplitudes. This noise was observed in apparently random bursts and seems to originate in faulty electronics, since large numbers of 'events' were registered even without beam. This noise doesn't seem to affect the dead time of the DAQ systems – for instance the noisy run 13 was measured to have negligible dead time (0.11%).

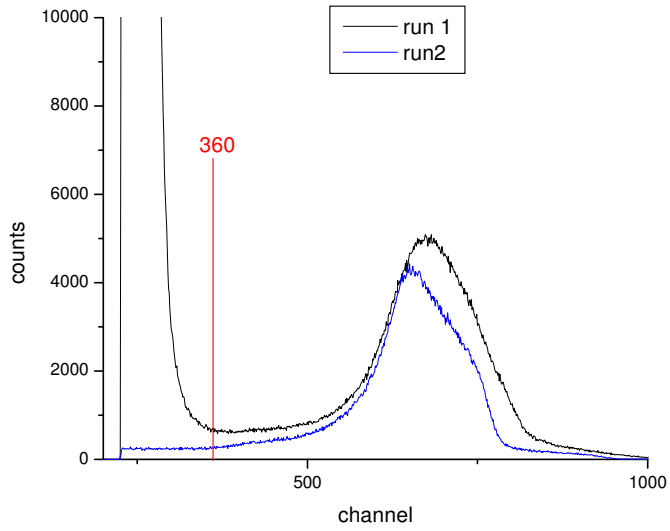

Figure 5: amplitude distribution of the long counter monitor, showing the large noise of run 1 compared to run 2, and the software threshold used.

The effects of the noise can be removed by applying a software cut at the low end of the amplitude distribution (Figure 5).
Figure 6 shows the variation of total monitor counts with time (file/cycle number) for the noisy run 13, compared with the monitor counts above the applied threshold for the same run. The variation of the timing signal of the PRT is also displayed for comparison, as an indication of the variation of the beam.
The application of the threshold removes the very large discrepancies caused by the noise and the response of the long counter is stable enough to be used as a reference.

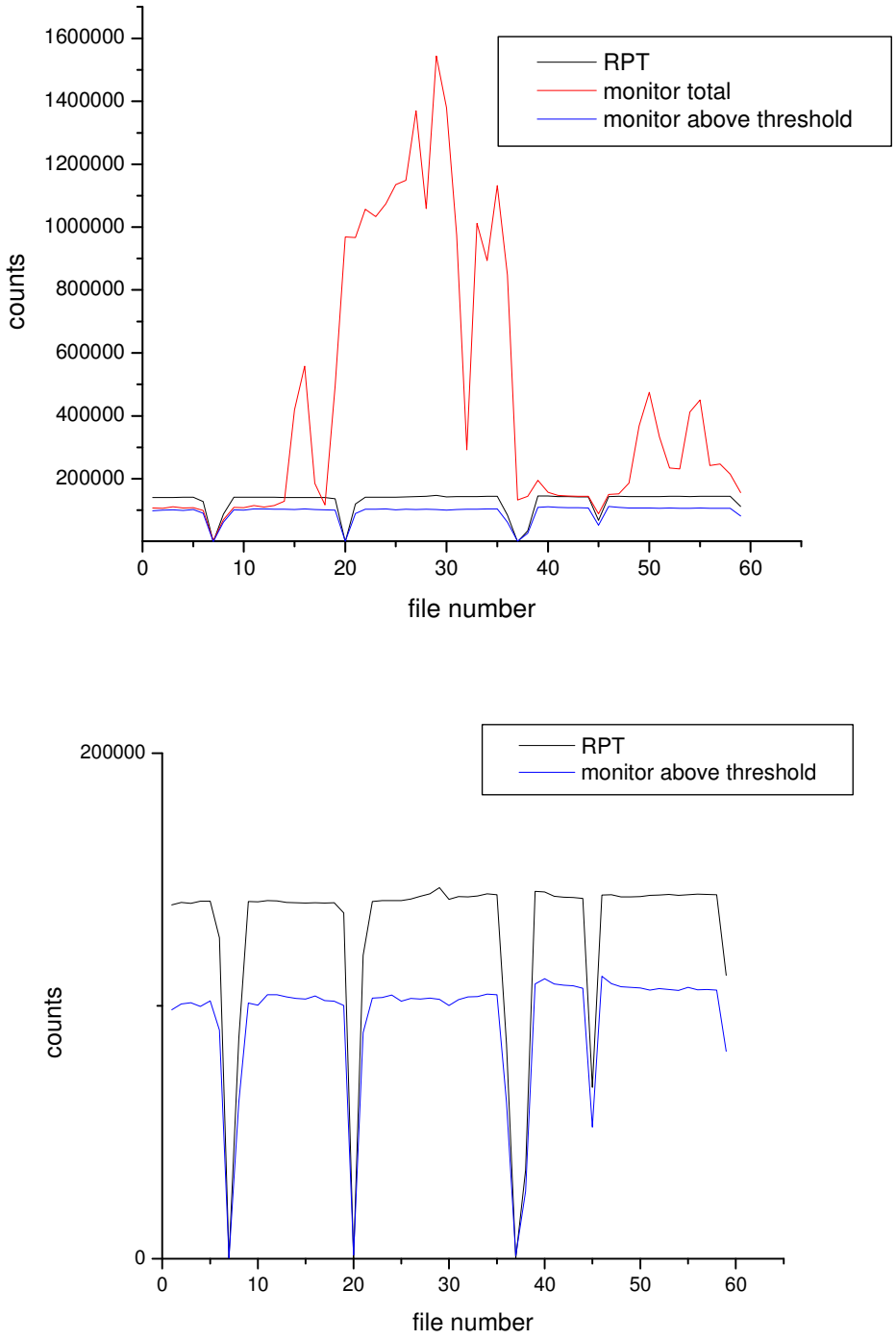

Figure 6: Top: total monitor counts (red) during run 13, compared with the monitor counts above the threshold (blue) and the total PRT counts for the same run (black). Bottom: detail of the top graph.

Two more monitors were used during the measurements:

- a scintillator at 0° from the beam axis at 1.967 m away from the source
- a ^{3}He counter outside the beam axis, connected to scaler 3A of xlipc102.

E. Dead time measurements

Two DAQ systems were used for the data collection, noted here as xlipc102 and xvgpc036. Several dead time measurements were taken for the two systems by connecting a pulser to the test input of the preamplifiers of the FC or PRT. The following dead time measurements were taken for the two DAQ systems:

Run	Run time (s)	FC/PRT	Distance (mm)	ADC	Measured DT (%)
xlipc102					
3	37660	PRT	252	4	0.40
4	5567	PRT inv.	252	4	0.19
10	12675	FC300 #8	out of beam	3	0.06
11	3250	FC300 #8	out of beam	3	0.06
13	105799	FC200	out of beam	3	0.11
16	221	FC200	1003	1	0.22
xvgpc036					
7	15904	PRT	out of beam	1	0.89
8	50097	PRT	740	4	11.47
9	4222	PRT inv.	740	4	13.55
10	12675	PRT	740	4	0.51
11	3250	PRT	740	4	1.13
12	62149	PRT	740	4	0.33
13	221	PRT	740	4	0.13
13	221	PRT	740	4	0.13

Table 4: Dead time measurements. The fourth column of the table gives the distance between the front window of the FC/PRT to the source.

The ADCs giving the large dead time at xvgpc036 during runs 8, 9 were wrongly configured in ‘updating’ mode. For subsequent, runs the ADC internal jumper was changed to non-updating mode and the problem was eliminated.
In the data analysis a dead time of 0.22% was considered for the FC measurements (all taken with DAQ xlipc102). For the PRT the measured dead time values were used for each run individually.

F. Calibration runs

To determine the offset of the ADCs different attenuation factors were applied to the pulser signal. The measured pairs (x, y) = (attenuation factor, ADC channel number) were fitted linearly as y = a*x + b and gave the following offset values b:

DAQ	ADC	FC	a	b
xlipc102	1	FC300 #8	2629.08	4.48
xlipc102	2	FC300 #8	2623.49	92.17
xlipc102	3	FC300 #8	2609.48	92.11
xlipc102	3	FC200	2611.32	87.16
xlipc102	4	FC300 #8	2611.57	-10.64
xlipc102	4	FC300 #11	3647.68	-13.99

Table 5: Calibration measurements.

These were used in the analysis as the offset channel (O) for the pulse height distributions of the fission chambers. However it must be noted that these values are approximate in the sense that they were measured at the end of the experimental session for nominally

equivalent conditions and not for each of the measurements separately. For an accurate analysis a measurement of the offset is needed immediately before or after an actual measurement.

The negative values of the last 2 offsets have no physical significance. Since these are small and don't affect many datasets (ADC4 of xlipc102 was mainly used with the scintillator and foil #11), they are used as they are in the following analysis, also with the purpose of assessing if and how they affect the results.

2. DATA ANALYSIS

A. Fission chambers

i. Data reduction and gating

Typical raw amplitude and timing distributions from the fission chambers are shown in Figure 7.

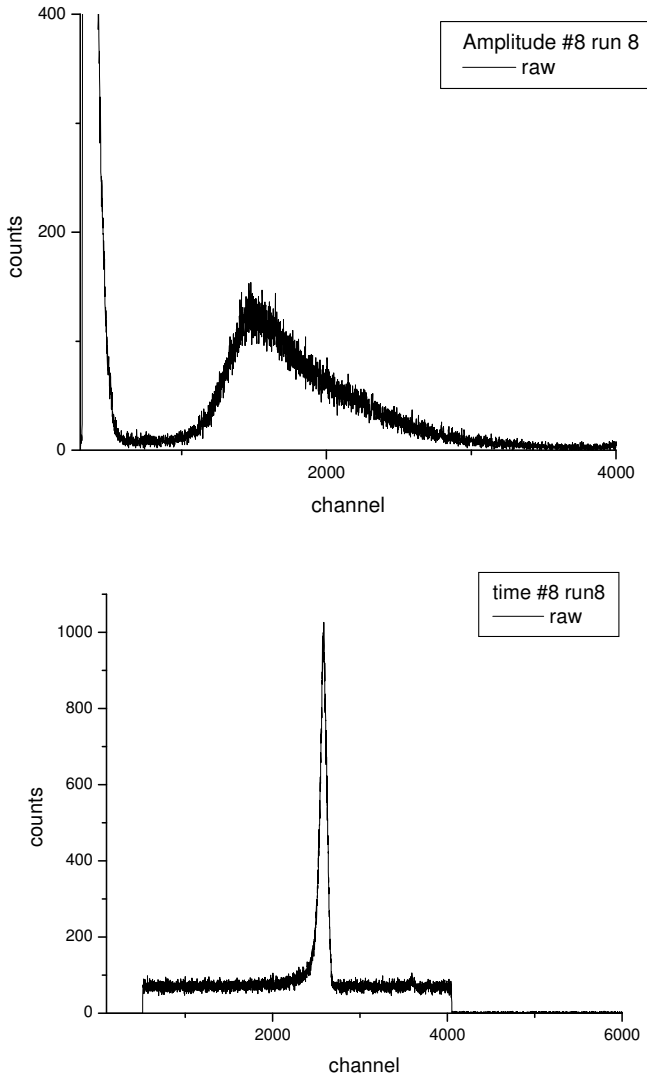

Figure 7: raw amplitude and timing distribution for FC300 #8, run8.

As in the January runs, the amplitude distribution shows a well-defined plateau between the alphas and the fission fragments for both chambers. However, the lower limit of 0.45P (where P is the channel of the fission fragment peak) no longer works well for FC200, so this rule of thumb is not applied here. Instead a threshold of roughly the centre of the plateau was considered for all spectra.

Software gates were applied on these distributions on an event-by-event basis to sort the events of interest, i.e. fission fragments from neutrons arriving directly from the source (within the time peak).
Figure 8 shows typical gated timing and amplitude distributions resulting from the conditions on the corresponding raw amplitude and timing spectra respectively.
The gating discards the largest part of the background for both spectra, giving much better defined peaks and a wider plateau in the case of the amplitude distribution.

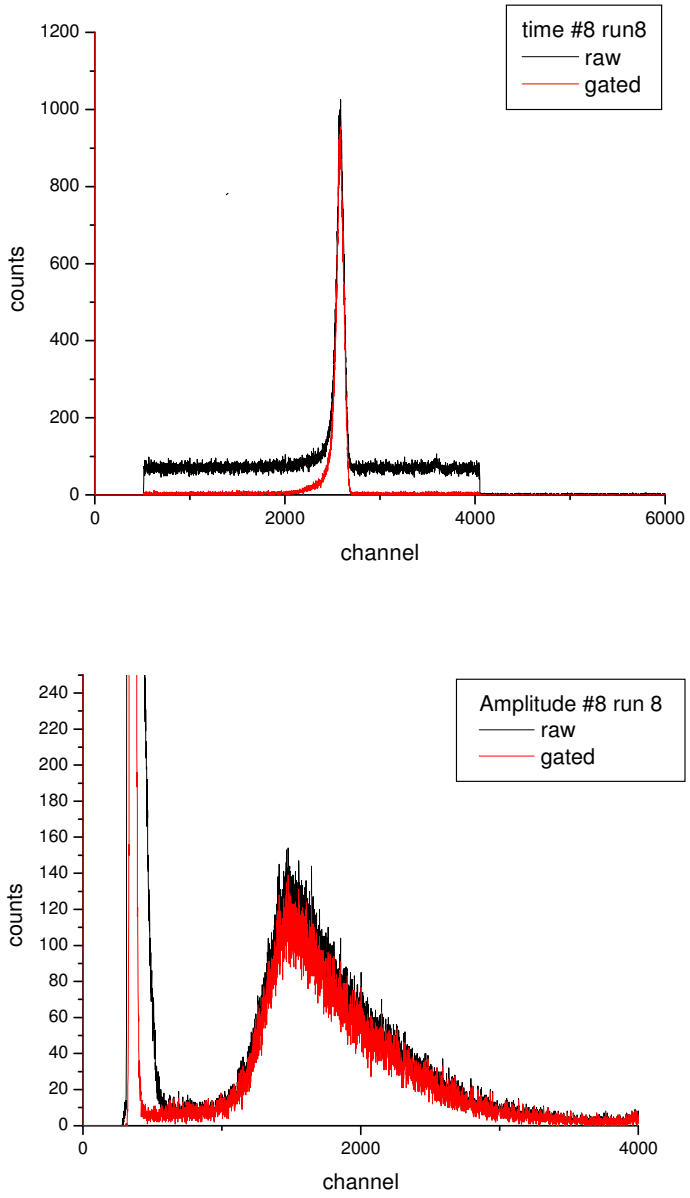

Figure 8: gated timing and amplitude distributions from FC300 #8 and the related ungated spectra.

ii. Further background subtraction

Although gating discards most of the background events, there is still a small component in the gated spectra (Figure 8) that could be subtracted.
Further treatment was applied by the following two approaches:

a) Using the timing distribution

The average number of counts was calculated in the regions left and right of the time peak (regions C_1, C_2 in figure 13). The mean of C_1 and C_2 was considered as the background below the time peak and was subtracted from it. The number of detected fission fragments was calculated from the integral of the resulting time peak.

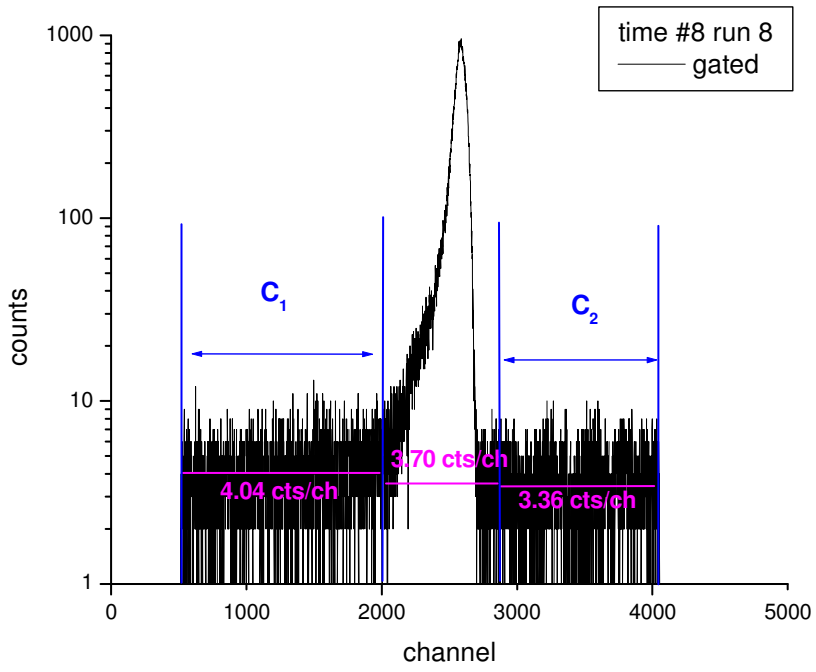

Figure 13: the mean of the background levels of C1 and C2 is subtracted from the time peak.

Notably region C_1 always has a higher number of counts than C_2. In the raw spectra the difference is ≤2%, while in the gated distributions it is more pronounced (10-15%).

b) Using the amplitude distribution

The gated amplitude distribution is examined in this case. Since it contains only events within the peak of the timing distribution, those that need to be discarded are the events that correspond to the background within that region.

This was calculated in the following way:

- software gates were applied on the regions C_1 and C_2 of the time distribution separately, which produced the amplitude distributions A_1 and A_2 (Figure 14).

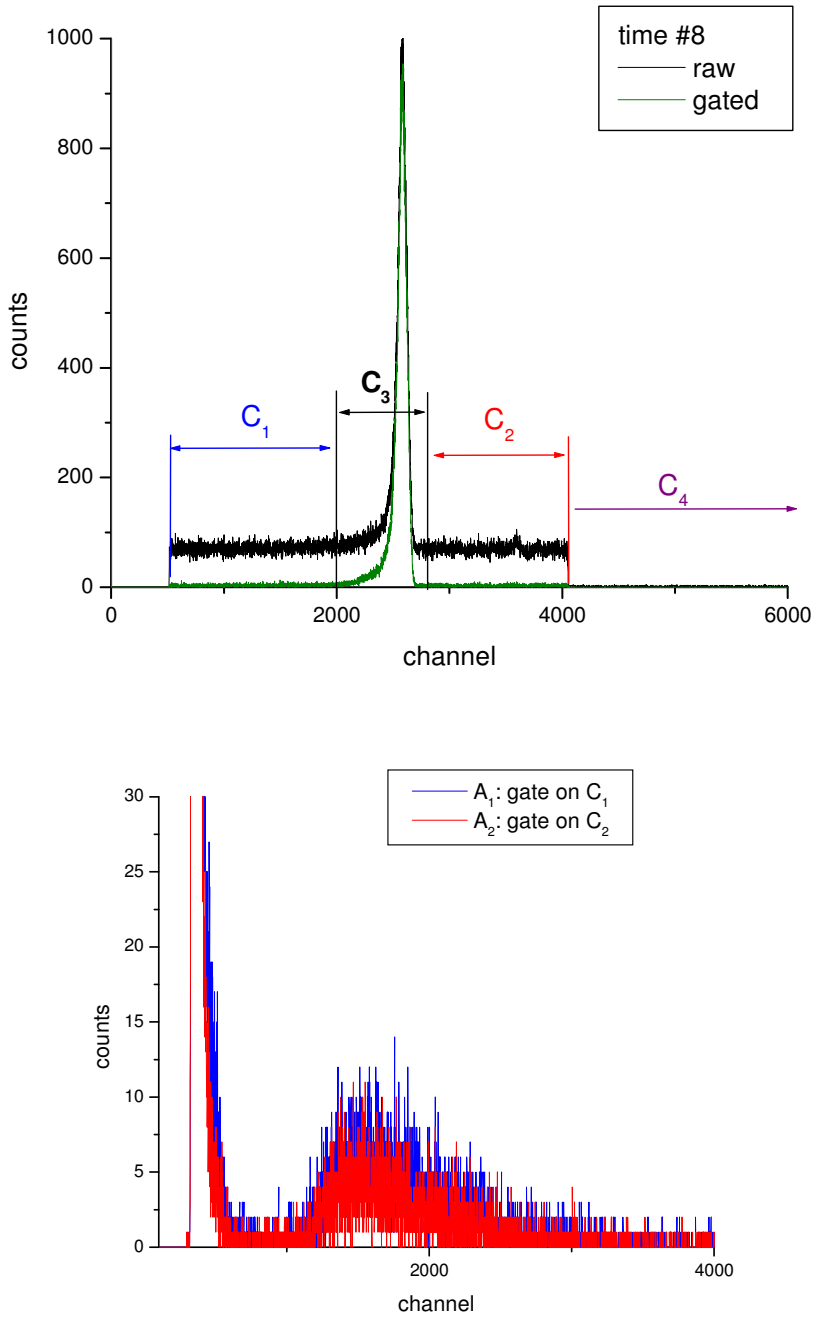

Figure 14: gating on the background regions C_1 and C_2 and the produced amplitude spectra A_1 and A_2.

- If N_i the number of channels in the region C_i, the distribution A_3 of the background in region C_3 is constructed by scaling A_1 and A_2 according to:
  $A_3 = N_3 \cdot ((A_1/N_1+A_2/N_2)/2)$.

The resulting component A_3 is then subtracted from the initial gated amplitude spectrum..

As shown in fig. 15, the procedure largely eliminates the alpha peak from the spectrum.

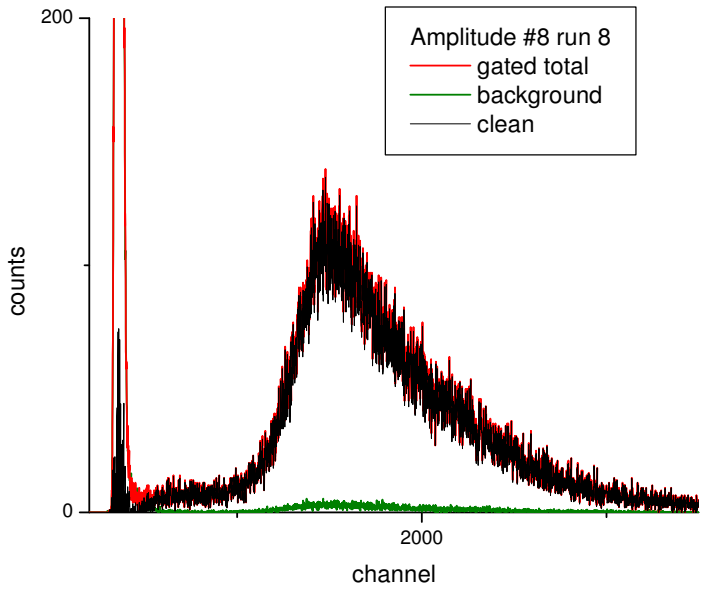

Figure 15: The produced background A_3 (green line), the gated (red) and clean (black) distributions.

The region C_4 on the right of C_2 in the timing distribution has a very low background that can be missed, and because it is spread over a large number of channels, it can account to a significant number of events (figure 16). This background doesn't affect the above calculations (the amplitude spectrum is gated for the region C_3) but it does make a difference when looking at the total number of events in the time and amplitude distributions. Then it must be taken into account, otherwise these will not be consistent.

No counts were recorded on the left of region C_1.

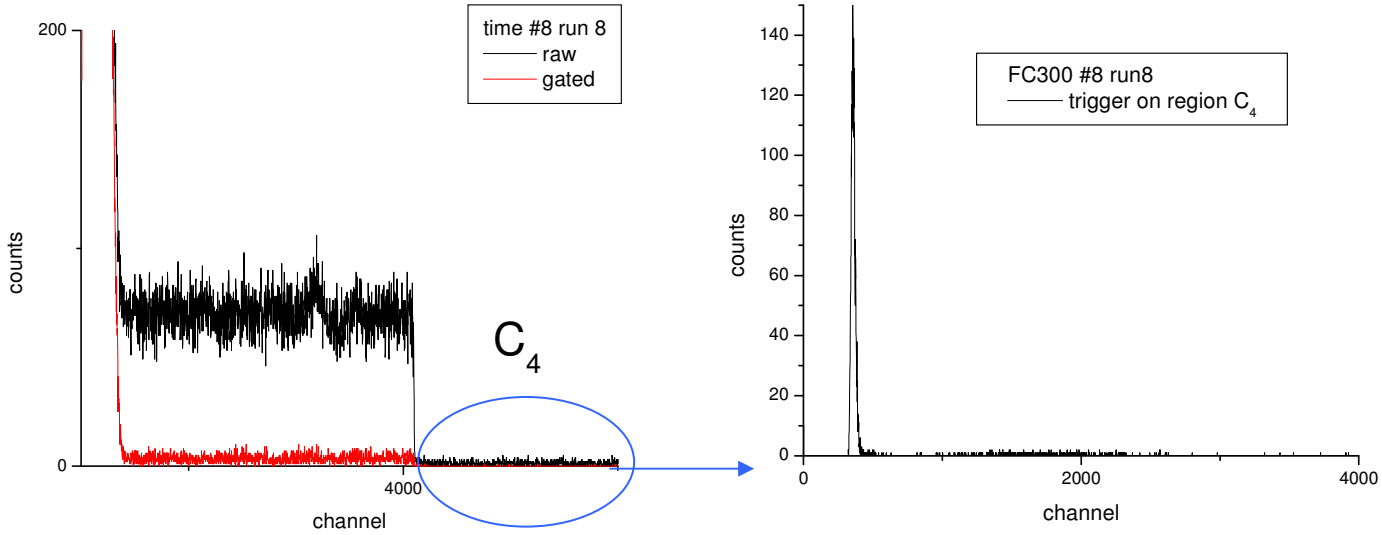

Figure 16: the background of region C_4 and the corresponding amplitude spectrum.

c) Comparison of the two methods

The two methods showed very good agreement, with an average difference of 0.44% between the resulting clean numbers of fission fragments, which is reasonable considering the amount of approximations used.
The only exception to this agreement was the short run 7 for foil 11, where the second method gave 7% higher counts than the first – this was probably due to the poor linear fit of the regions C_1, C_2 because of the low statistics.

As figure 15 shows, the cleaning procedure causes a minimal change in the fission fragment distributions near and above the threshold and affects mostly the region below threshold.
To confirm the validity of the technique, all the following analysis is presented for both the gated-only spectra and the cleaned distributions.
As will be presented next, the gated and clean spectra yield similar fractions $Y_A/(Y+Y_A)$ of fission fragments below threshold. For the two FC300 deposits there is a small difference in $Y_A/(Y+Y_A)$, 4.5% for #8 and 4.1% for #11 (tables 8, 10).
The largest change after cleaning appears for FC200 (table 13), where there is an average decrease of 6.90% in $Y_A/(Y+Y_A)$. This reflects a change of about 40% in the larger distances (runs 14, 17) and 50% for 487.5 mm distance from the source (run 12).

Looking at each FC200 run individually (figures 17, 18) it appears that the alpha peak extends much farther into the plateau than it originally appeared. Therefore caution must be exerted when choosing the threshold, and background measurements with no beam may be necessary to define it correctly in any future measurements.

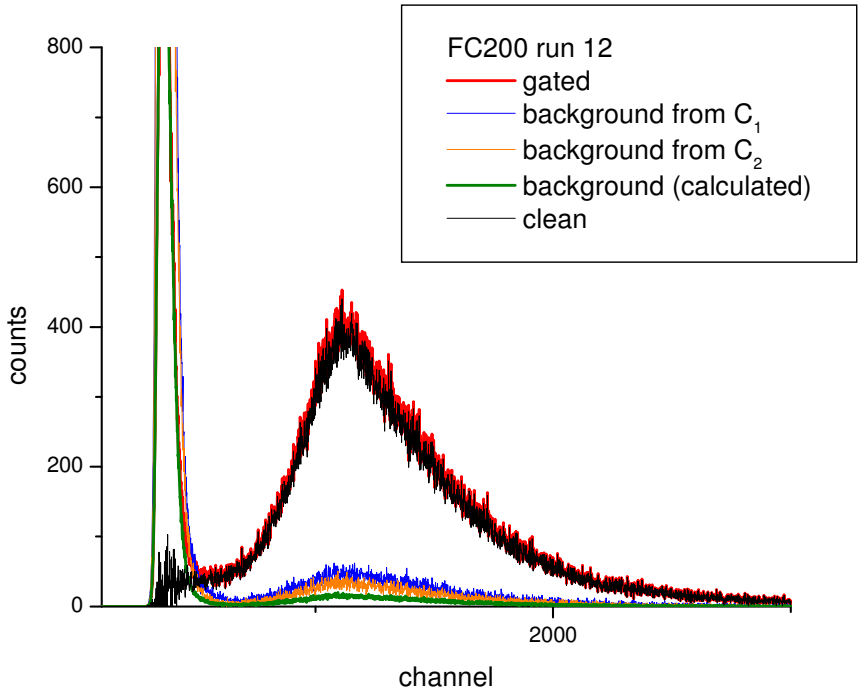

Figure 17: Gated, background and clean amplitude distributions for FC200, run 12.

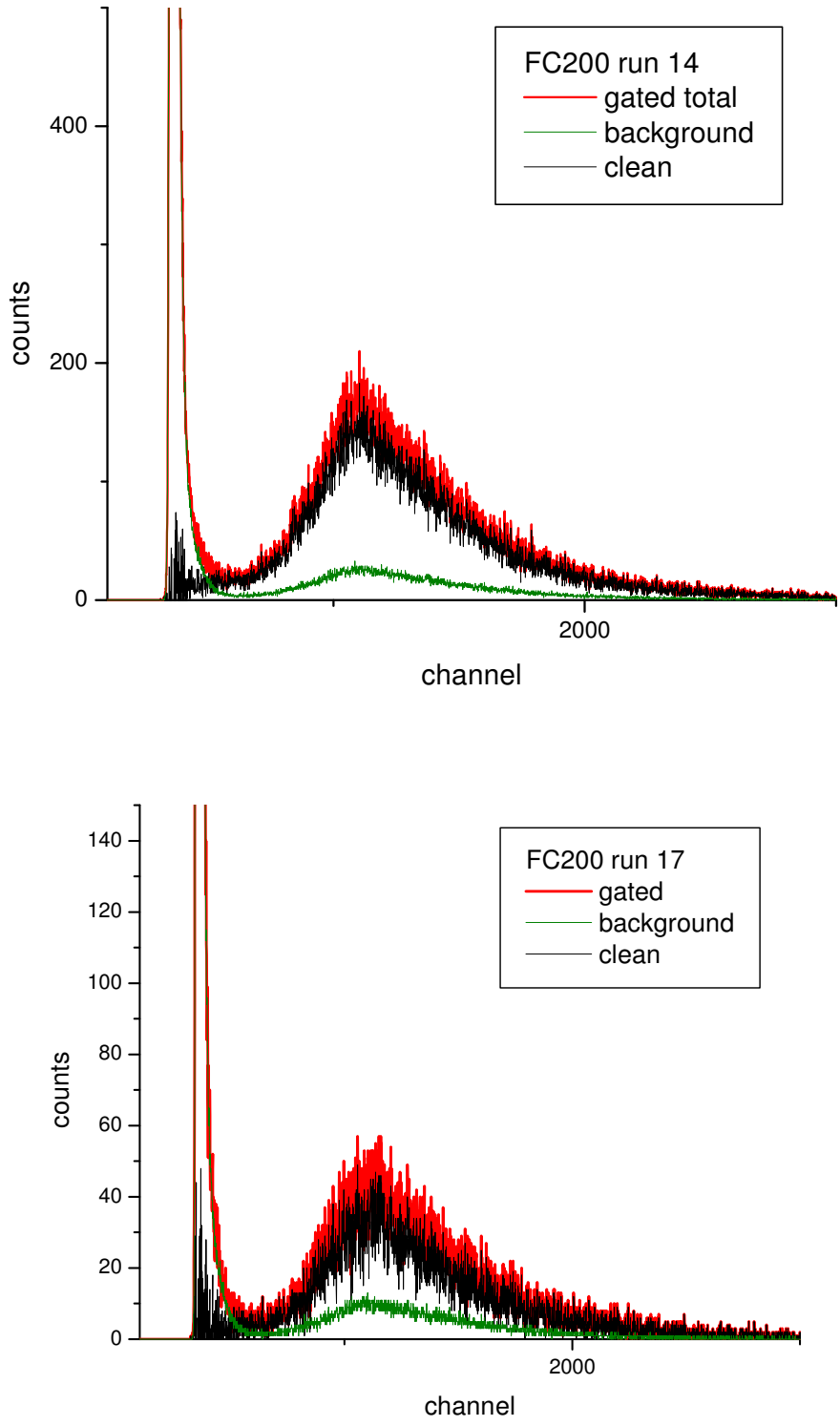

Figure 18: Gated, background and clean amplitude distributions for FC200, runs 14 and 17.

It must also be noted that with the largest part of the alpha peak removed, the resulting fission fragment distribution below the threshold is not horizontal, but presents a small downward slope. The slope is more pronounced for the deposits of FC300, for which the

clean fission fragment distribution appears to drop to zero right after the top end of the residual alpha peak (figures 17, 18, 19).
This shape may raise the question on whether the area defined between the apparent 'zero' and the threshold has an actual physical meaning and defines the fission fragment distribution below threshold. A rough estimation of the number of counts Y_G included in this region shows that not to be the case, as shown in table 6.

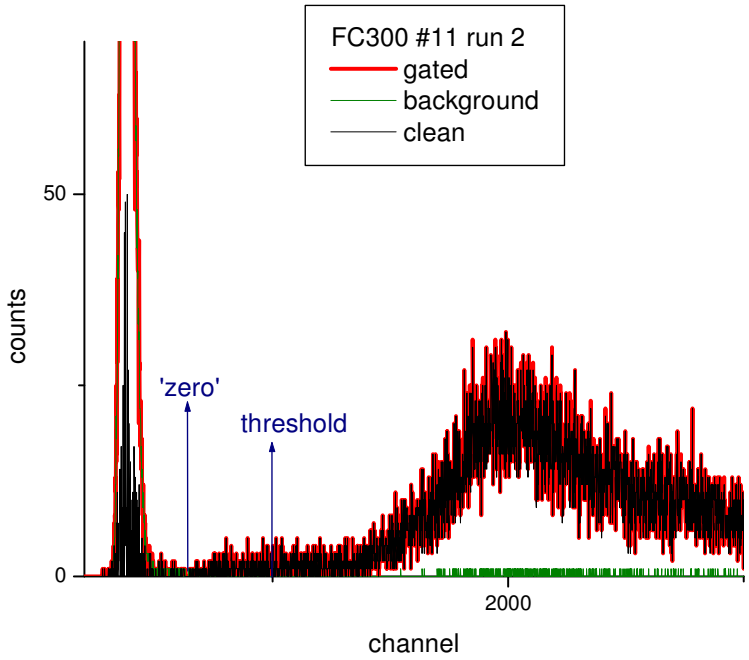

Figure 19: Gated, background and clean amplitude spectra for foil 11 of FC300, run 2. The channel where the clean distribution appears to drop to 0 ('zero') and the applied threshold are indicated.

For the calculation of Y_G a simple integral was taken between the 2 limits for foils #8 and #11, while for FC200 the events of the remaining alpha peak were first manually rejected from the graph.

run	'zero' channel	threshold C	Y_G	$Y+Y_G$	$Y_G/(Y+Y_G)$
FC300 #8					
1	443	850	488	22414.73	2.18%
2	446	780	394	44947.94	0.88%
7	-	850	-	-	-
8	430	675	1002	98134.43	1.02%
9	441	675	137	14968.5	0.92%
FC300 #11					
1	728	1000	81	11977.39	0.68%
2	621	1000	308	25094.29	1.23%
7	-	1000	-	-	-
FC200					
12	280	520	4761	293224.51	1.62%
14	317	610	2643	104403.56	2.53%
17	412	610	548	25431.26	2.15%

Table 6: The fission fragment integrals Y_G between the threshold and the channel where the clean distributions appear to drop to 0 ('zero' channel). Run 7 has too low statistics to define a 'zero' channel.

The resulting fractions $Y_G/(Y+Y_G)$ have a mean of 1.25% for deposit #8, 0.95% for #11 and 2.1% for FC200. These are significantly lower than the anticipated fractions of fission fragments below threshold, which are expected to be in the order of >3%.

iii) Corrections and results

In order to deduce the neutron rates detected by the fission chambers, the fission fragment distributions must also be corrected for the following quantities:

1. The number Y_A of fission fragments below threshold (detailed calculation follows)
2. The dead time of the measurements, according to table 4
3. The fraction Y_B of fission fragments that stop in the deposit.
   According to the Budtz-Jørgensen article (NIM A236 (1985) 630-640), the inefficiency of 2π counting for evaporated UF_4 is:
   $$\Delta_{UF_4} = (10.5 \pm 0.7) \cdot t\,(\%)$$
   where t is the UF_4 thickness of the deposit in mg/cm^2.
   A correction factor $F=1-\Delta_{UF4}$ was applied as $Y+Y_A+Y_B=(Y+Y_A)/F$.

   From the thickness and isotopic compositions of the used deposits shown in table 7, the corrections are:
   $\Delta_{UF4}(\#11) = 0.0660 \pm 0.0044$ or $F(\#11) = 0.9340$
   $\Delta_{UF4}(\#8) = 0.0656 \pm 0.0044$ $F(\#8) = 0.9344$
   $\Delta_{UF4}(FC200) = 0.0533 \pm 0.0036$ $F(FC200) = 0.9467$
   For the double-sided deposit 8 and the FC200 chamber, the average UF_4 thicknesses were used.

	Thickness (μg/cm^2)			Isotopic composition (%)			
foil	**U**	**^{235}U**	**UF_4**	**^{234}U**	**^{235}U**	**^{236}U**	**^{237}U**
FC300 #8							
8/side1	472.60	472.32	625.05	0.036	99.940	0.011	0.013
8/side2	471.30	471.02	623.33	0.036	99.940	0.011	0.013
8 average	471.95	471.67	624.56				
8 total	943.90	943.33	1248.38				
FC300 #11							
11	475.30	475.01	629.00	0.036	99.940	0.011	0.013
FC200							
foil1_side1	421.97	421.23	557.45	0.062	99.826	0.036	0.073
foil2_side1	419.38	418.65	554.04	0.062	99.826	0.036	0.073
foil3_side1	421.46	420.72	556.78	0.062	99.826	0.036	0.073
foil1_side2	383.45	382.78	506.57	0.062	99.826	0.036	0.073
foil2_side2	382.99	382.33	505.96	0.062	99.826	0.036	0.073
foil3_side2	382.98	382.32	505.95	0.062	99.826	0.036	0.073
foil4	326.79	326.22	431.71	0.062	99.826	0.036	0.073
foil5	327.15	326.58	432.19	0.062	99.826	0.036	0.073
FC200 total	3066.17	3060.83	4050.64				
FC200 average	383.27	382.60	507.21				

Table 7: Thickness and isotopic composition of the UF_4 deposits of FC300, FC200.

4. The extended surface of the foil, including corrections for the angle dependence of the fluence, the ^{235}U(n,f) cross section and the inhomogeneity of the deposit. This correction was applied on the distance as $R' = R \Big/ \sqrt{1655.84 \Big/ R^2}$.

Calculation of number Y_A of fission fragments below threshold

Two methods can be applied for the calculation of the fission fragment amplitude distribution below threshold:

1. The distribution is extended horizontally between the threshold channel C and the offset channel O (figure 20) with a constant value of:

y = b = average number of counts/channel in plateau

b is calculated between the low (L) and high (H) limits of the plateau.

The number of fission fragments below the threshold is:

$$Y_A = b \cdot (C\text{-}O)$$

with uncertainty

$$u(Y_A) = u(b) \cdot (C\text{-}O)$$

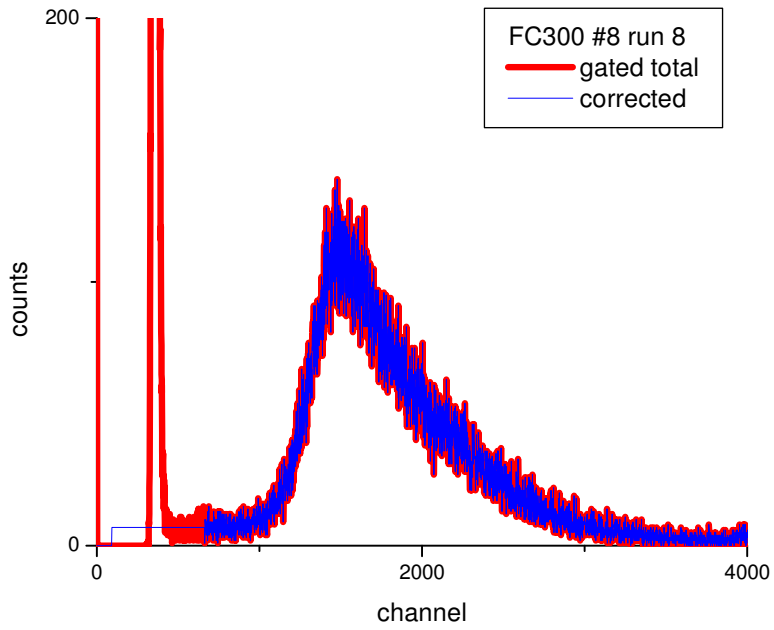

Figure 20: gated amplitude distribution from FC300 #8 with threshold correction.

2. The distribution between L and H is fitted with the linear function

$$y = a \cdot x + b$$

Y_A is then calculated with the relations:

$$Y_A = \frac{a}{2}(C^2 - O^2) + b(C - O)$$

and the uncertainty of Y_A:

$$u^2(Y_A) = \left[\frac{u(a)}{2}(C^2 - O^2)\right]^2 + [u(b)(C - O)]^2 + \left[\frac{u(a)}{2}(C^2 - O^2)\right][u(b)(C - O)]C_{ab}$$

The data analysis of the January runs showed that comparable and similarly good results can be achieved with both methods with low uncertainties in the order of 1-2%. However the use of gating on the current data produces fission fragment distributions with much lower statistics, not as well defined in the plateau region and with larger variations. This is more pronounced after the further background subtraction, where the cleaned distributions present a slope in the region of the plateau (figures 17, 18, 19).

Consequently the first method may introduce large uncertainties in the definition of Y_A and the resulting neutron rates, and perhaps method 2 presents a more realistic simulation to the shape of the region below threshold.

To estimate and compare the magnitude of the uncertainties for each method, both procedures were applied for all data. The produced neutron rates were subsequently tested with the distance from the source (tables 9, 11, 14) according to:

$$y = P_1 + P_2/x^2$$

where y: detected neutron fluence/monitor count, x: distance from source in cm.

The results for the gated and the clean amplitude distributions are presented in tables 8, 10 and 13. The total yields $Y+Y_A+Y_B$, detected neutron rates and their corresponding uncertainties are expressed per monitor count and have been corrected for dead time.

FC300 #8

run	Y_A	$\frac{u(Y_A)}{Y_A}$	$\frac{Y_A}{Y+Y_A}$	$Y+Y_A+Y_B$ */monitor*	$\frac{u(Y+Y_A+Y_B)}{Y+Y_A+Y_B}$	*neutrons/cm^2 /monitor*	±
GATED DISTRIBUTION							
y=b							
1	1236.19	78.30%	5.07%	$2.56\cdot10^{-2}$	4.02%	218.90	8.80
2	2156.36	56.48%	4.51%	$7.12\cdot10^{-2}$	2.59%	608.56	15.75
7	249.62	174.25%	5.09%	$8.25\cdot10^{-3}$	8.97%	70.51	6.32
8	4040.70	37.98%	3.88%	$6.41\cdot10^{-2}$	1.51%	548.16	8.26
9	563.13	101.74%	3.54%	$6.47\cdot10^{-2}$	3.69%	553.32	20.43
y=ax+b							
1	1232.99	23.57%	5.06%	$2.56\cdot10^{-2}$	1.35%	218.87	2.95
2	4765.47	22.30%	9.45%	$7.51\cdot10^{-2}$	2.15%	641.75	13.81
7	355.07	53.31%	7.08%	$8.43\cdot10^{-3}$	4.01%	72.02	2.89
8	3794.70	17.02%	3.65%	$6.40\cdot10^{-2}$	0.70%	546.86	3.81
9	765.54	27.96%	4.75%	$6.56\cdot10^{-2}$	1.55%	560.36	8.68
GATED AND CLEAN DISTRIBUTION							
y=b							
1	1154.49	81.02%	5.00%	$2.43\cdot10^{-2}$	4.10%	207.30	8.51
2	2070.37	57.64%	4.44%	$6.94\cdot10^{-2}$	2.60%	593.12	15.43
7	235.46	179.41%	5.61%	$7.06\cdot10^{-3}$	10.17%	60.31	6.14
8	3898.87	38.67%	3.86%	$6.23\cdot10^{-2}$	1.53%	532.14	8.12
9	548.90	103.05%	3.57%	$6.26\cdot10^{-2}$	3.77%	535.30	20.16
y=ax+b							
1	1195.13	23.77%	5.17%	$2.43\cdot10^{-2}$	1.39%	207.66	2.88
2	5057.66	20.92%	10.19%	$7.38\cdot10^{-2}$	2.18%	631.13	13.75
7	352.04	51.59%	8.16%	$7.25\cdot10^{-3}$	4.46%	61.98	2.76
8	3732.10	17.18%	3.70%	$6.22\cdot10^{-2}$	0.71%	531.26	3.78
9	741.96	28.65%	4.76%	$6.34\cdot10^{-2}$	1.59%	542.02	8.59

Table 8: Results with two methods for deposit #8 of FC300.

The most striking difference between the two methods appears in the uncertainty of the value of Y_A, which is very high for the case of the y = b approach. This is due to the very low statistics in the plateau region, which give values of b between 0.3 and 7 counts/channel for foil #8, and therefore high values of u(b).

Another discrepancy appears in the higher fraction $Y_A/(Y+Y_A)$ for method 2.
The mean value of $Y_A/(Y+Y_A)$ for the gated distributions is 4.42% when calculated with method 1, and 6.00% with method 2.
For the clean spectra the corresponding values are 4.50% and 6.40%.
The high values for method 2 correspond to the low statistics run 7, which can be ignored, and run 2, which presents a fairly large slope in the plateau region (figure 21).
Disregarding these runs, method 2 gives $\langle Y_A/(Y+Y_A)\rangle = 4.49\%$ for the gated and $\langle Y_A/(Y+Y_A)\rangle = 4.54\%$ for the cleaned spectra.

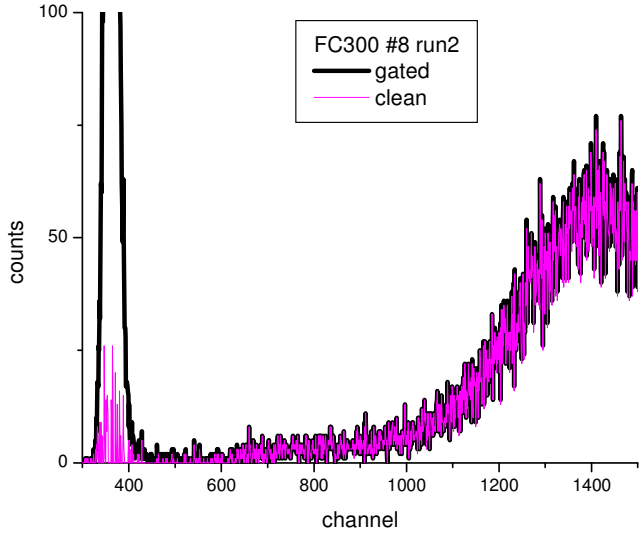

Figure 21: gated and clean amplitude distributions for FC300 #8 for run 2.

The above differences do not reflect to the detected neutron rates, which only disagree by about 2% - however their uncertainties again differ considerably, with 2.1% for the linear fit and 4.4% for the flat distribution.

Applying the distance test to the above values, very good agreement with the $1/r^2$ rule is found for all datasets (table 9, figure 22).

FC300 #8		**P_1**	**u(P_1)**	**P_2**	**u(P_2)**	**C_{12}**	**Reduced χ^2**
GATED	**y=b**	16.10	4.69	652395.00	8979.00	-0.77	0.53
	y=ax+b	15.92	7.44	651229.00	15750.00	-0.78	7.04
GATED & CLEAN	**y=b**	6.63	4.70	644468.00	9051.00	-0.77	0.57
	y=ax+b	6.46	7.47	644468.00	16080.00	-0.77	7.65

Table 9: Fit parameters for the datasets of table 8 with the function $y= P_1 + P_2/x^2$. C_{12} is the correlation coefficient of the fit.

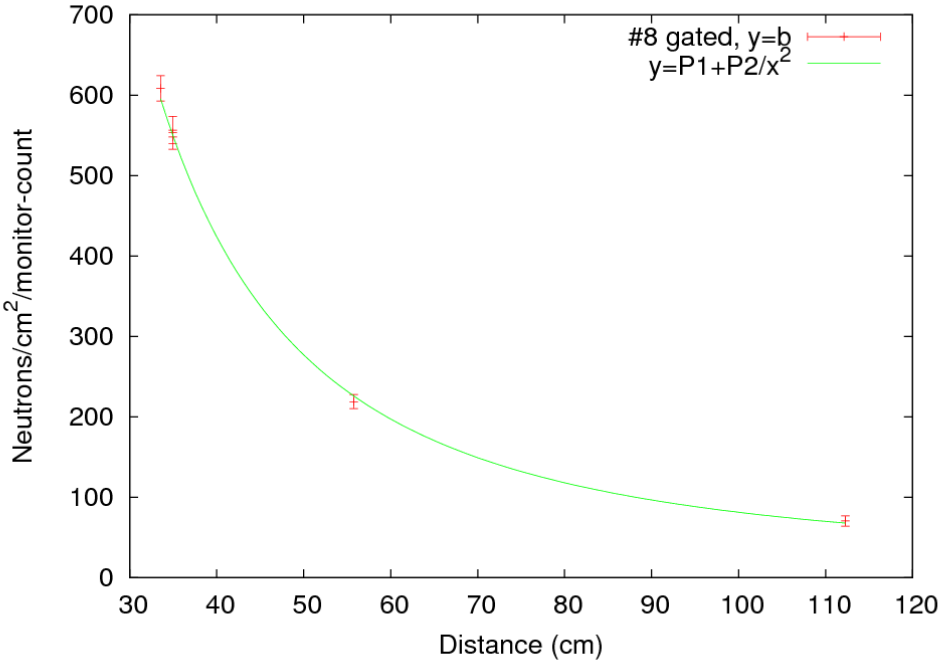

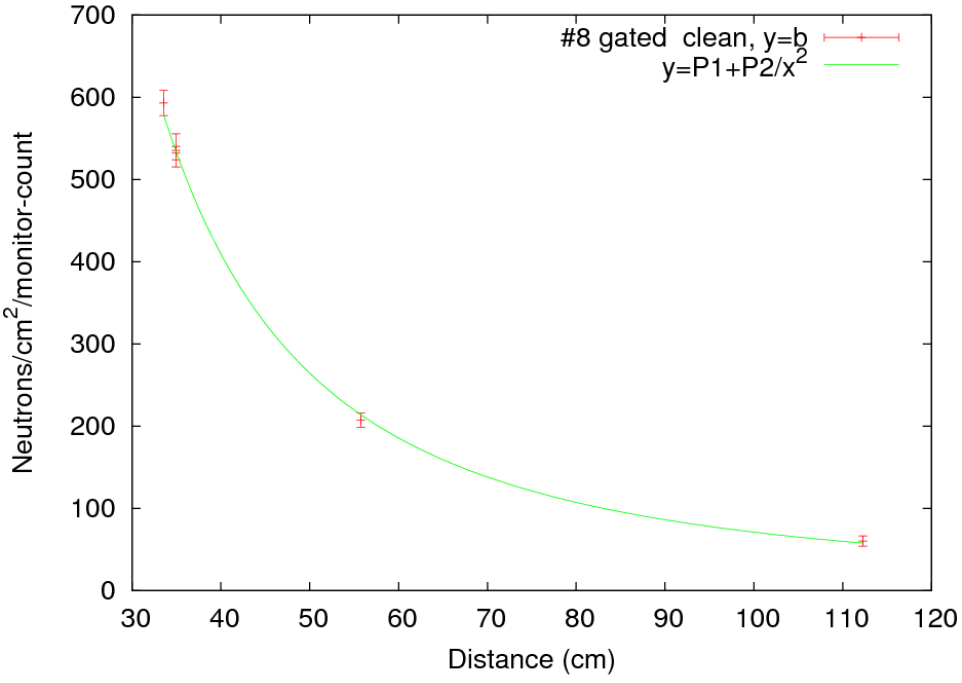

Figure 22: The neutron rates measured by FC300 #8 as a function of distance from the neutron source. Results for gated (top) and cleaned (bottom) distributions, calculated with method 1 (flat plateau). Fits with the function $y= P_1 + P_2/x^2$ (green line).

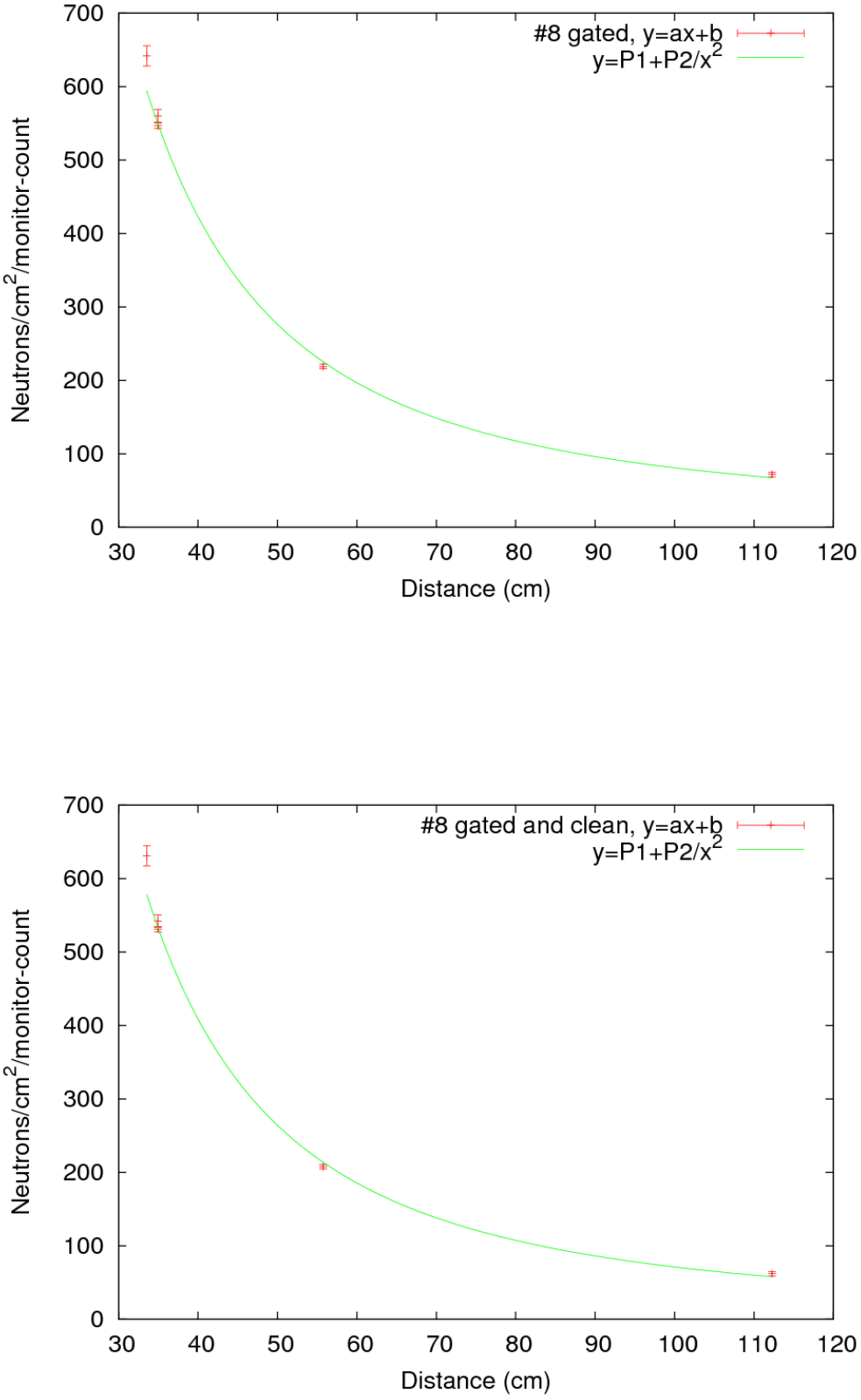

Figure 23: The neutron rates measured by FC300 #8 as a function of distance from the neutron source. Results for gated (top) and cleaned (bottom) distributions, calculated with method 2 (linear fit of the plateau). Fits with the function $y= P_1 + P_2/x^2$ (green line).

As expected, the higher uncertainties of method 1 result in better fits than method 2. The χ^2 values suggest that the y = b approach overestimates the starting uncertainties of the detected neutron rates, while y = ax + b may be underestimating them. Nevertheless the excellent agreement between the P_1, P_2 values of the clean datasets suggests that the produced values with both methods are reliable.

The parameters P_1 of table 9 also display the effects of the background subtraction process, showing a small but clear reduction in the background component of the spectra.

Similarly, for deposit #11:

FC300 #11

run	Y_A	$\frac{u(Y_A)}{Y_A}$	$\frac{Y_A}{Y+Y_A}$	$Y+Y_A+Y_B$ */monitor*	$\frac{u(Y+Y_A+Y_B)}{Y+Y_A+Y_B}$	*neutrons/cm² /monitor*	±
GATED DISTRIBUTION							
y=b							
1	464.11	147.81%	3.60%	$1.36\cdot10^{-2}$	5.39%	229.89	12.38
2	1272.85	89.25%	4.79%	$3.96\cdot10^{-2}$	4.32%	670.68	28.95
7	84.84	345.71%	3.54%	$4.03\cdot10^{-3}$	12.39%	68.33	8.47
y=ax+b							
1	610.99	21.96%	4.68%	$1.37\cdot10^{-2}$	1.34%	232.51	3.12
2	1571.11	12.42%	5.84%	$4.00\cdot10^{-2}$	0.94%	678.21	6.40
7	100.39	32.42%	4.16%	$4.06\cdot10^{-3}$	2.41%	68.78	1.66
GATED AND CLEAN DISTRIBUTION							
y=b							
1	456.91	148.97%	3.70%	$1.30\cdot10^{-2}$	5.58%	220.03	12.28
2	1245.73	90.22%	4.79%	$3.88\cdot10^{-2}$	4.36%	656.76	28.64
7	82.39	350.81%	3.76%	$3.68\cdot10^{-3}$	13.37%	62.35	8.34
y=ax+b							
1	597.80	22.21%	4.78%	$1.31\cdot10^{-2}$	1.38%	222.54	3.07
2	1553.01	12.44%	5.90%	$3.92\cdot10^{-2}$	0.95%	664.51	6.34
7	97.64	32.53%	4.43%	$3.71\cdot10^{-3}$	2.54%	62.78	1.59

Table 10: Results for deposit #11 of FC300.

The same differences between the two methods appear for foil 11, however there is a much better agreement of about 1% between the neutron rates.
Again the linear fit of the plateau results in higher numbers Y_A, and run 2 gives higher $Y_A/(Y+Y_A)$ fractions in all cases.
Method 1 gives $\langle Y_A/(Y+Y_A)\rangle$ = 3.97% for the gated and 4.08% for the clean spectra, while method 2 results in $\langle Y_A/(Y+Y_A)\rangle$ = 4.89% and 5.04% respectively.

The fits of the above datasets with the fluence–distance relation present the same image as before, with good agreement between parameters P_1, P_2 for the two methods and better fits for method 1, again with $\chi^2<1$ (table 11, figures 24,25).

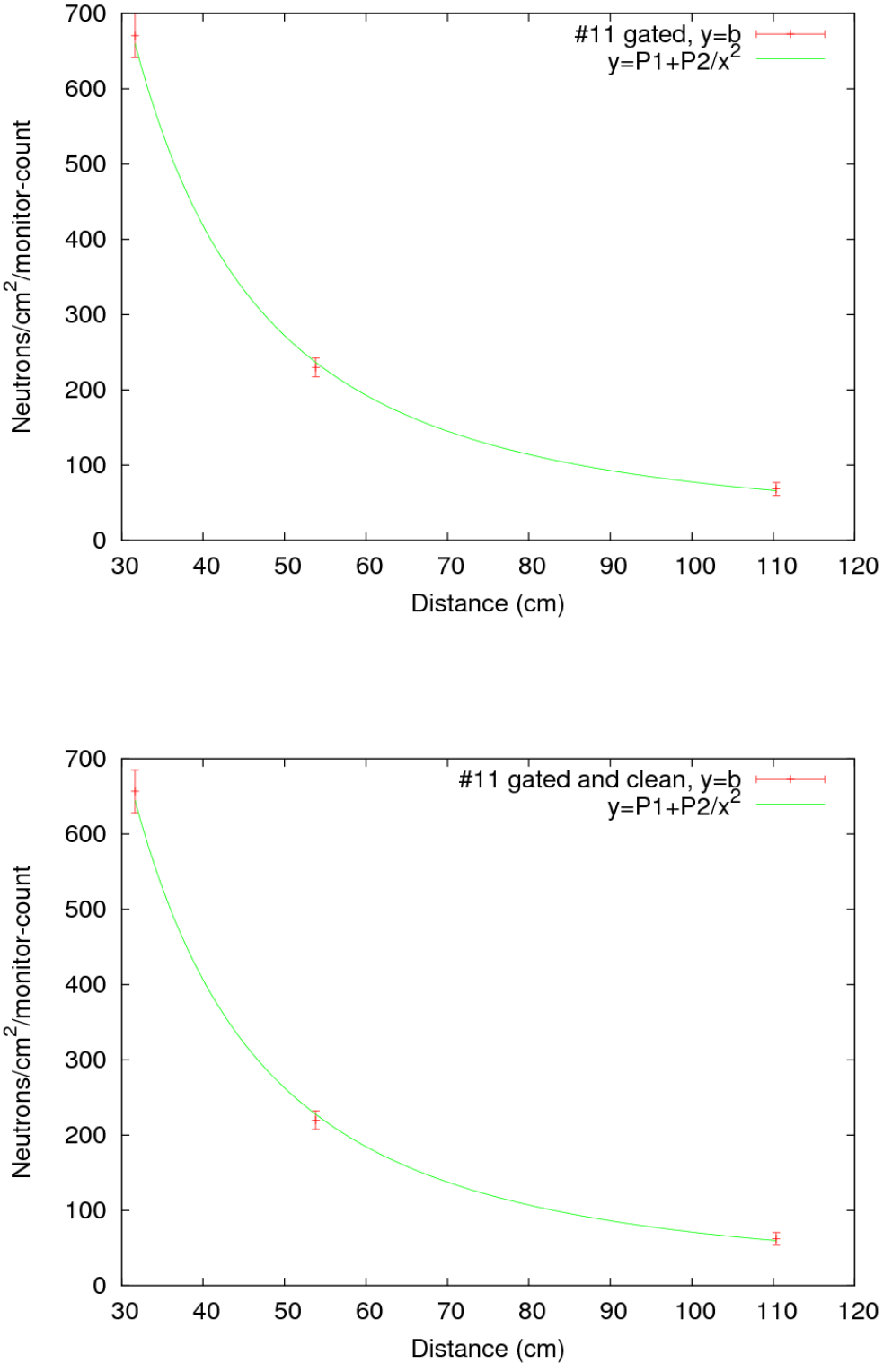

Figure 24: The neutron rates measured by FC300 #11 as a function of distance from the neutron source. Results for gated (top) and cleaned (bottom) distributions, calculated with method 1 (y=b). Fits with the function $y= P_1 + P_2/x^2$ (green line).

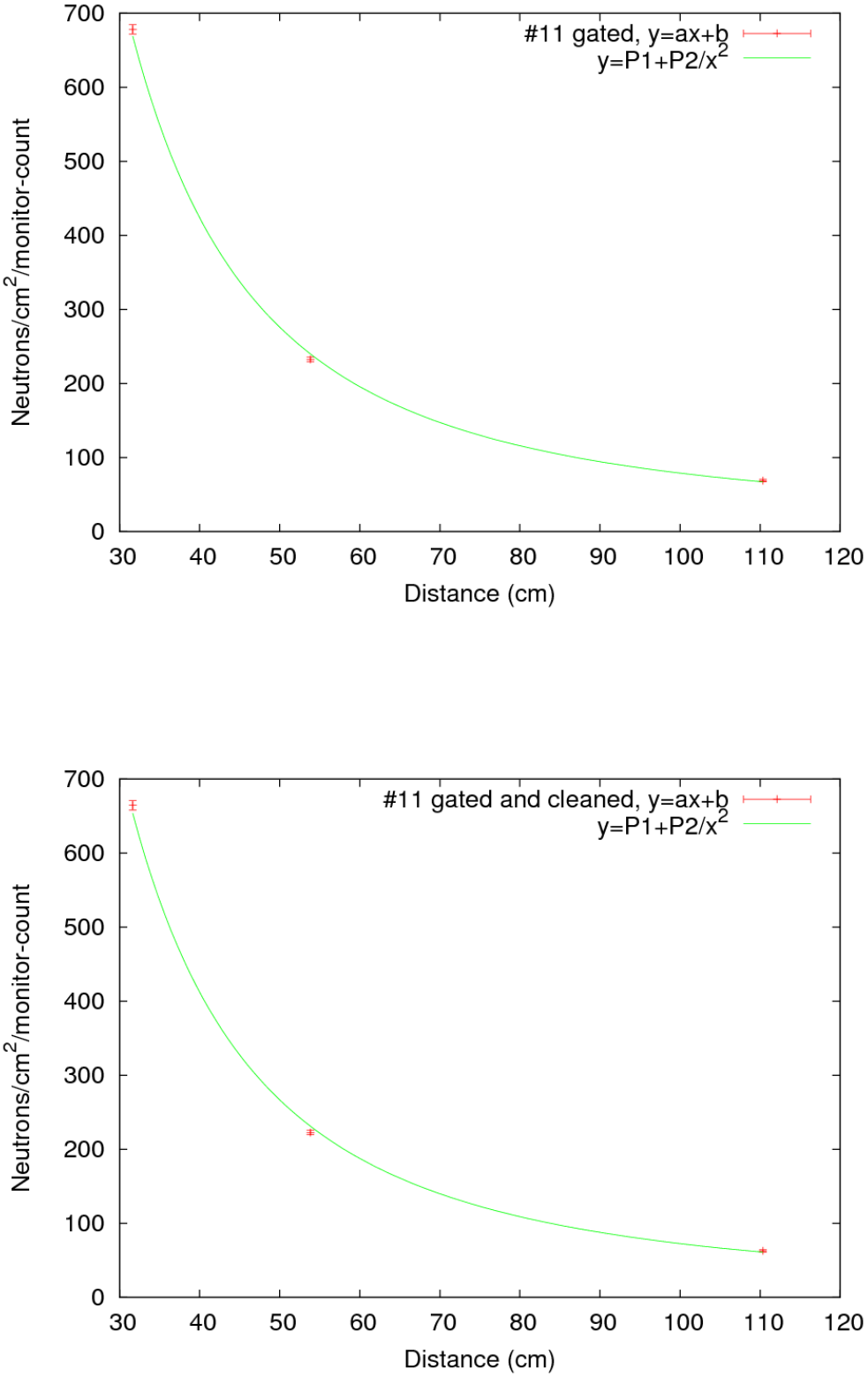

Figure 25: The neutron rates measured by FC300 #11 as a function of distance from the neutron source. Results for gated (top) and cleaned (bottom) distributions, calculated with method 2 (y=ax+b). Fits with the function $y= P_1 + P_2/x^2$ (green line).

FC300 #11		P_1	$u(P_1)$	P_2	$u(P_2)$	C_{12}	Reduced χ^2
GATED	**y=b**	12.86	6.55	648339.00	21240.00	-0.69	0.49
	y=ax+b	13.33	5.48	656869.00	19440.00	-0.65	8.55
GATED & CLEAN	**y=b**	7.41	7.45	638388.00	24220.00	-0.69	0.65
	y=ax+b	8.00	6.22	646897.00	22540.00	-0.65	11.86

Table 11: Fit parameters for the datasets of table 10 with $y= P_1 + P_2/x^2$.

A quick comparison of the total fission fragment yields detected by deposit #11 to those of #8 for the common runs 1,2 and 7, shows that all datasets display a relation of #11/#8 ≈ 0.52-0.53 (tables 8,10).
The two deposits however are not in the same distance from the source (#8 is 19.2 mm behind #11) so these numbers cannot be directly compared.
Using the fluence-distance relation and the parameters of table 11, the total fission fragment yield of #11 can be estimated at the position of #8.
A test with the parameters and data of the clean distribution for method 1 (3rd row of table 11) gives:

	#11 neutrons/cm^2				#11 total yield $Y+Y_A+Y_B$ (x10^{-2})				$(\#11)_{norm}$ / #8	
run	**measured**		**normalised to #8**		**measured**		**normalised to #8**		$Y+Y_A+Y_B$	
1	220.03	± 12.28	212.81	± 7.82	1.30	± 0.07	1.26	± 0.11	51.79%	± 4.98%
2	656.76	± 28.64	574.52	± 5.53	3.88	± 0.17	3.39	± 0.21	48.87%	± 3.30%
7	62.35	± 8.34	58.06	± 7.57	0.37	± 0.05	0.34	± 0.08	48.56%	± 12.20%

Table 12: comparison between total fission fragment yields of foils #8 and #11 for the common runs 1,2,7. The detected neutron rate and total yield of #11 have been normalised to the position of #8 according to $y= P_1 + P_2/x^2$ with the parameters of table 11. All quantities are expressed per monitor count.

The resulting ratios are consistent with the ^{235}U content ratio of the two foils (table 7), where ^{235}U(#11)/ ^{235}U(#8) = 50.35%.

The P_2 parameters for the two foils can give an estimate of their relative efficiency. Method 1 produces the ratio $< P_2(\#11)/P_2(\#8)> = 99.24 \pm 2.65\%$, and method 2 $<P_2(\#11)/P_2(\#8)> = 100.65 \pm 2.87\%$ (weighed means).

For FC200 the gated spectra contain higher numbers of counts, so the uncertainties of method 1 are lower than before - for the case of the clean distributions, even lower than those calculated with method 2.

FC200

run	Y_A	$\frac{u(Y_A)}{Y_A}$	$\frac{Y_A}{Y+Y_A}$	$Y+Y_A+Y_B$ */monitor*	$\frac{u(Y+Y_A+Y_B)}{Y+Y_A+Y_B}$	*neutrons/cm^2 /monitor*	±
GATED DISTRIBUTION							
y=b							
12	19037.32	14.99%	5.95%	$1.05\cdot10^{-1}$	0.91%	275.11	2.51
14	10190.52	22.54%	7.77%	$2.79\cdot10^{-2}$	1.77%	73.38	1.30
17	2946.60	41.92%	8.30%	$1.33\cdot10^{-2}$	3.52%	34.86	1.23
y=ax+b							
12	15736.61	16.32%	4.97%	$1.04\cdot10^{-1}$	0.83%	272.27	2.26
14	13080.11	20.86%	9.76%	$2.85\cdot10^{-2}$	2.05%	75.00	1.54
17	4936.23	23.71%	13.16%	$1.40\cdot10^{-2}$	3.16%	36.81	1.16

Table 13: Results for FC200.

FC200

run	Y_A	$\frac{u(Y_A)}{Y_A}$	$\frac{Y_A}{Y+Y_A}$	$Y+Y_A+Y_B$ */monitor*	$\frac{u(Y+Y_A+Y_B)}{Y+Y_A+Y_B}$	*neutrons/cm^2 /monitor*	±
GATED AND CLEAN DISTRIBUTION							
y=b							
12	16642.17	16.03%	5.45%	$9.98 \cdot 10^{-2}$	0.89%	262.51	2.35
14	8098.61	25.29%	7.37%	$2.34 \cdot 10^{-2}$	1.89%	61.48	1.16
17	2130.09	49.31%	7.89%	$1.01 \cdot 10^{-2}$	3.93%	26.52	1.04
y=ax+b							
12	21049.09	12.10%	6.80%	$1.01 \cdot 10^{-1}$	0.84%	266.30	2.24
14	13028.75	21.77%	11.35%	$2.44 \cdot 10^{-2}$	2.49%	64.24	1.60
17	4072.69	28.99%	14.07%	$1.08 \cdot 10^{-2}$	4.11%	28.43	1.17

Table 13 (cont.): Results for FC200.

Like in the January tests, a higher fraction of fragments are lost below threshold for FC200 than foils 8 and 11 because of the different field structure of this chamber.
The mean fraction for method 1 is 7.34% (gated) and 6.90% (clean spectra), while method 2 again gives higher percentages, with $\langle Y_A/(Y+Y_A)\rangle$ = 9.30% (gated) and 10.74% (clean).
The uncertainties $u(Y_A)$ from method 1 are generally lower for FC200 than for the FC300 deposits, and for the high statistics runs 12 and 14 they are comparable to those derived with method 2.

The results of table 13 also agree very well with the $1/r^2$ rule (table 14, fig. 26, 27).

FC200		**P_1**	**$u(P_1)$**	**P_2**	**$u(P_2)$**	**C_{12}**	**Reduced χ^2**
GATED	**y=b**	8.58	3.14	641222.00	20090.00	-0.69	7.26
	y=ax+b	10.70	3.08	628466.00	18040.00	-0.67	7.10
GATED & CLEAN	**y=b**	-0.68	1.12	631256.00	7580.00	-0.69	1.22
	y=ax+b	1.06	1.37	635817.00	7873.00	-0.67	1.37

Table 14: Fit parameters for the datasets of table 13 with the function $y= P_1 + P_2/x^2$.

Table 14 shows that also the goodness of the fit is comparable for the two methods, as in the January data. If this similarity is due to the better statistics, it would signify that the two methods converge for longer measurement times. This would be useful to investigate experimentally, as it would shed more light on the actual shape of the distribution near and below threshold.

The effect of the cleaning process is more pronounced for this chamber. Besides the reduction of the parameter P_1, the goodness of the fit also appears to improve with the further background subtraction.

From the above analysis of all three chambers, the cleaning technique appears to be generally beneficial for precise efficiency measurements. However it only adds a small improvement to the already good quality of the gated data, so it does not appear to be vital for simple flux measurements with the fission chambers.

The consistency of the results for FC200 is especially encouraging, as the more complex structure of this chamber necessitated several approximations to be used in the data analysis concerning the position and thickness of the UF_4 foils.

A comparison with deposit #8 (table 9) gives a relative efficiency of FC200 of $\langle P_2(FC200)/P_2(\#8)\rangle = 98.03 \pm 1.59\%$ with method 1, and $98.87 \pm 2.19\%$ with method 2.

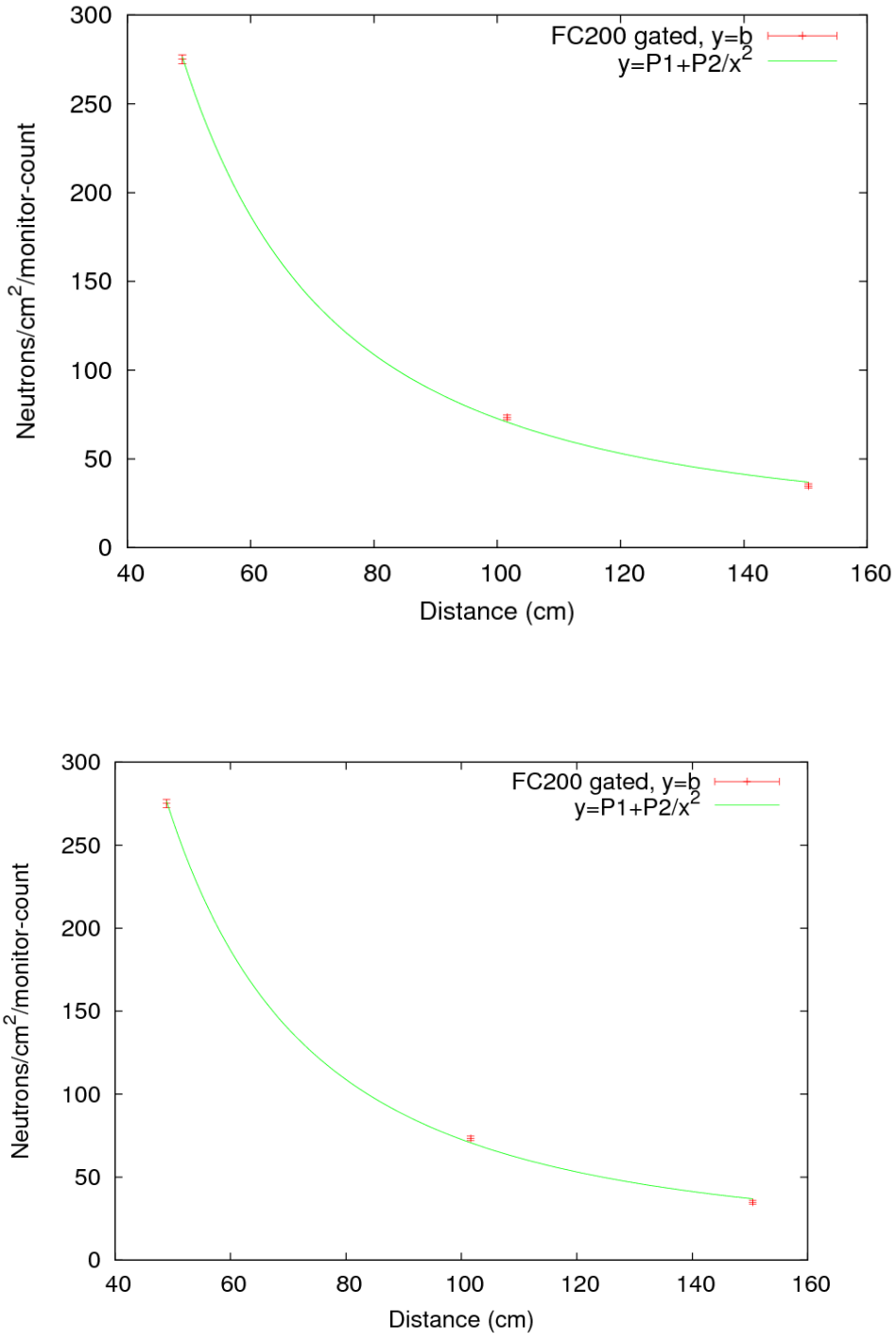

Figure 26: The neutron rates measured by FC200 as a function of distance from the neutron source. Results for gated (top) and cleaned (bottom) distributions, calculated with method 1 (y=b). Fits with the function $y= P_1 + P_2/x^2$ (green line).

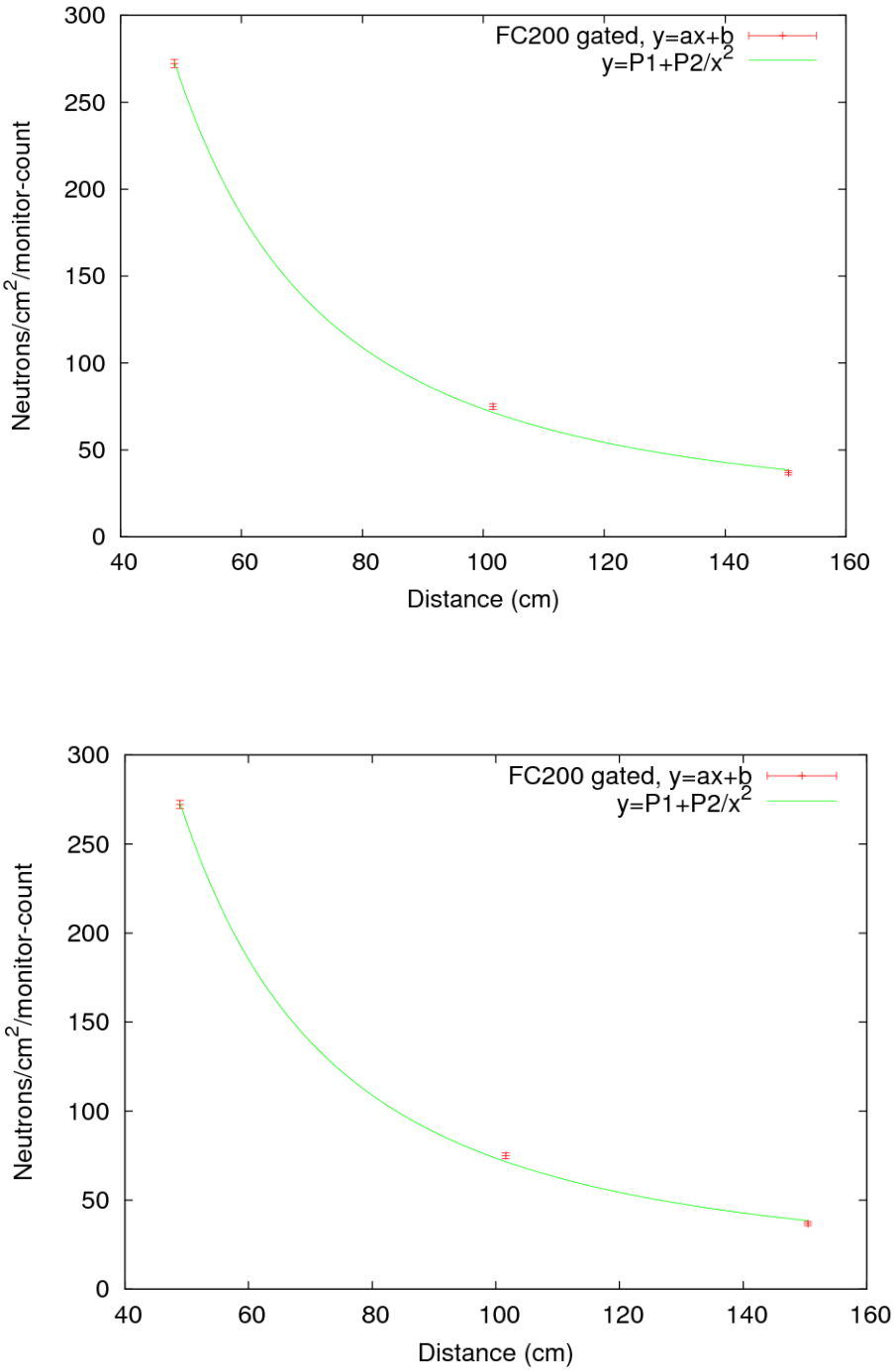

Figure 27: The neutron rates measured by FC200 as a function of distance from the neutron source. Results for gated (top) and cleaned (bottom) distributions, calculated with method 1 (y=ax+b). Fits with the function $y= P_1 + P_2/x^2$ (green line).

From all the above, both methods for calculating Y_A give reasonable results with fairly good agreement. Method 1 introduces higher uncertainties for $Y+Y_A+Y_B$ but better fits to the $1/r^2$ rule, while the opposite applies for method 2. At this stage it is unclear which simulation technique is more advantageous. Additional data with higher statistics would be most helpful for a better understanding of how these two approaches compare.

B. Proton Recoil Telescope

i. Data reduction and gating

The raw PRT data are sorted by setting up conditions on the timing and amplitude distributions. The stages of the data treatment are shown in Figures 28 and 29. Starting from the raw data, a condition is set for both proportional counter wires to fire simultaneously with the silicon detector (time and amplitude signals). In this way the rough limits of the time and amplitude peaks are found and applied as initial gates to the complementary distributions. These limits are subsequently narrowed until well-defined peaks are achieved for both spectra.

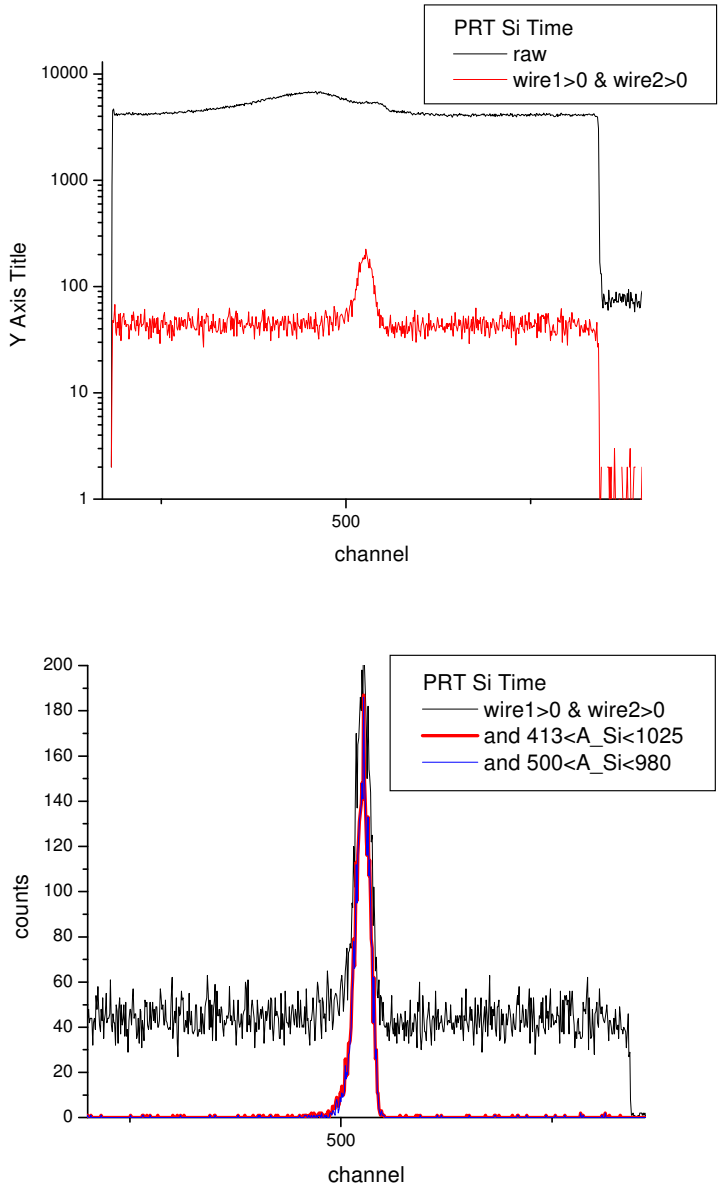

Figure 28: The timing signal of the Si detector of the PRT. Top: raw data, and with the condition for both PC wires firing. Bottom: with successively stricter conditions on the amplitude spectrum.

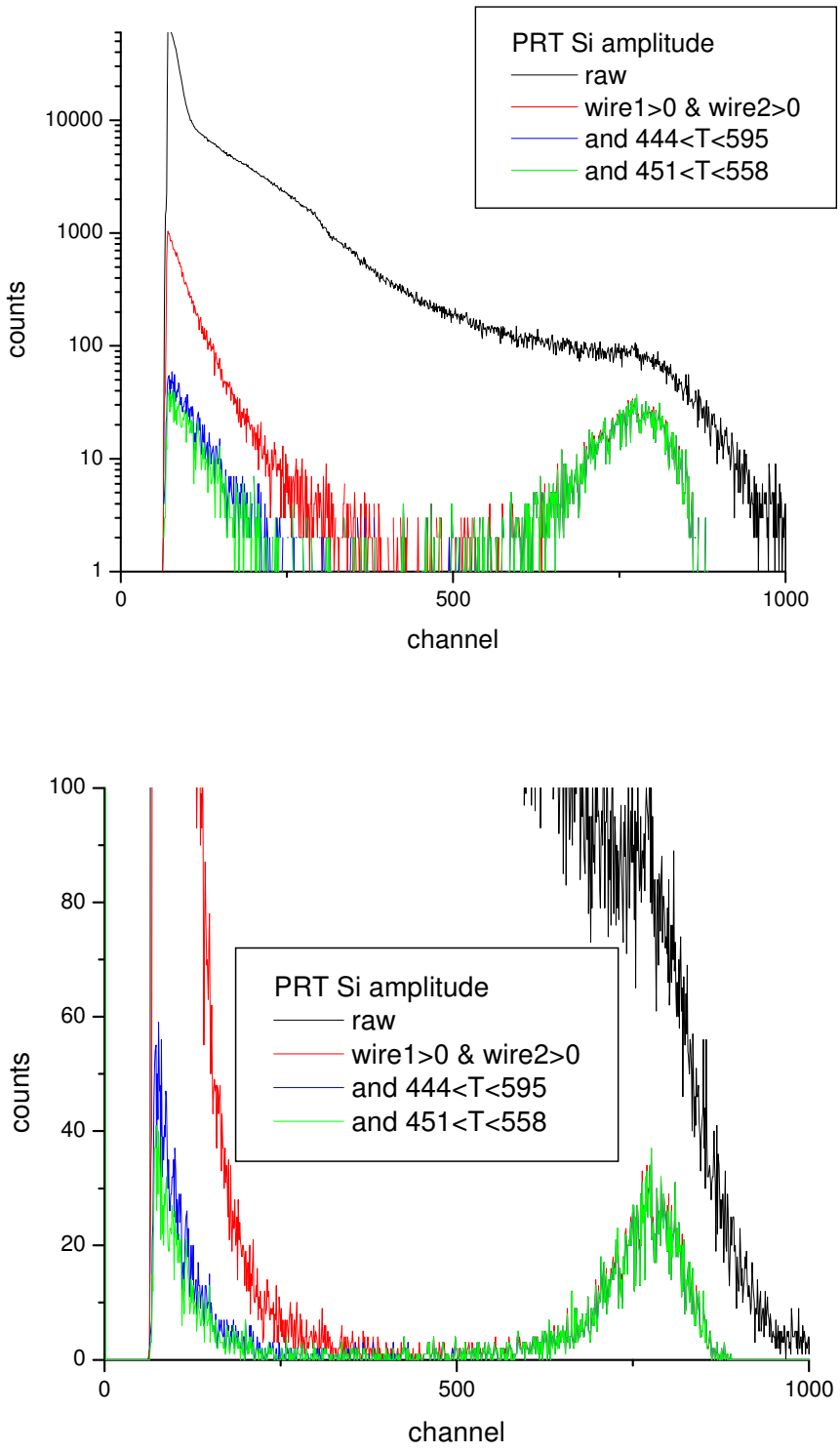

Figure 29: The amplitude signal of the Si detector of the PRT. Top: raw data, and with successively stricter conditions. Bottom: the same in linear scale.

The total number of events was taken from the integral of the time peak and corrected for dead time.

ii. Background subtraction

Background measurements with the Ta plate inverted were taken during runs 4 and 9, with the PRT at 252 mm and 740 mm from the source respectively.
Both measurements contain large uncertainties: run 4 had very low statistics and run 9 a very high dead time. In addition, the PRT was behind FC300 during runs 8 and 9.

The measured background spectra were expressed per monitor count and were deducted from the corresponding forward PRT runs (figure 30).
The background levels were measured to be 14.97% at 252 mm and 16.31% at 740 mm distance of the PRT from the source.
The measured yields of proton recoils are shown in table 15.

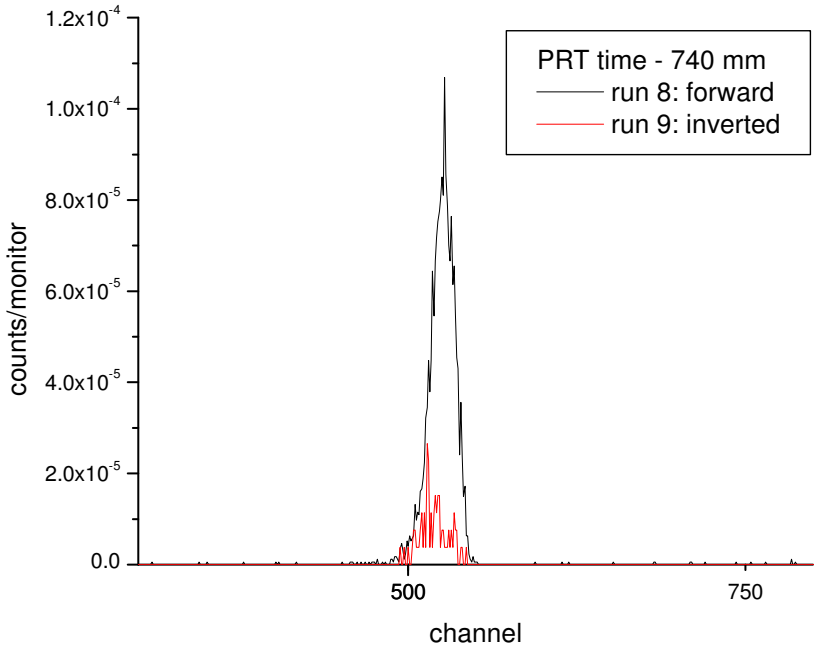

Figure 30: Forward PRT time spectrum at 740 mm (black) and background (red) at 740 mm.

run	description	Distance (mm)	PRT recoils/monitor	PRT recoils/monitor corrected for background
3	forward	252	$1.52 \cdot 10^{-2}$	$1.295 \cdot 10^{-2}$
4	inverted	252	$2.28 \cdot 10^{-3}$	
8	forward, FC300 #8	740	$2.14 \cdot 10^{-3}$	$1.792 \cdot 10^{-3}$
9	inverted, FC300 #8	740	$3.49 \cdot 10^{-4}$	
10	forward	740	$1.89 \cdot 10^{-3}$	$1.544 \cdot 10^{-3}$
11	forward	740	$1.85 \cdot 10^{-3}$	$1.499 \cdot 10^{-3}$
12	forward, FC200	740	$1.94 \cdot 10^{-3}$	$1.562 \cdot 10^{-3}$
13	forward	740	$1.86 \cdot 10^{-3}$	$1.511 \cdot 10^{-3}$

Table 15: PRT measurements.

At the 740 mm distance, for which we have several measurements, there is reasonably good agreement between the results of the different runs (except the rejected runs 8, 9).

iii. Influence of FC

The comparison between run 12 to the corresponding runs where the PRT looks directly at the source (10,11 and 13), shows that the existence of FC200 between the source and the PRT increases the neutron fluence at the telescope by 3.62%.
Regarding FC300, run 8 indicates a very high increase of 12.81% but the high dead time (11.47%) of this run doesn't permit to draw any useful conclusions from this value.

iv. Neutron fluence calculation

The program PRTelescope.exe was used to calculate the corresponding neutron fluences for the two distances.
Considering 1 proton recoil count at the distances of the experiment, the corrections and results from the program are shown in the top part of table 16. Because dead time corrections have already been applied on the measured values of PRT counts/monitor, the dead time correction factor input to the program is 1.0.
The last rows of table 16 give the measured PRT counts/monitor (from table 15), and the resulting neutron rates at the source and the front plate of the telescope according to the program output. The 740 mm input value was calculated as the mean from runs 10-13 (run 12 was corrected for the FC200 influence).

distance source-front plate (mm):	252	740
distance source-radiator (mm):	277	765
Dead time correction factor:	1.0	1.0
total n-p cross section @2MeV (mb):	2915.0	2915.0
Correction for window and backing:	1.002	1.002
Correction for air scattering:	1.002	1.005
Correction for wires:	1.017	1.017
Total correction:	1.021	1.024
Neutrons/sr at source:	$0.479 \cdot 10^{8}$	$0.365 \cdot 10^{9}$
Neutrons/cm^2 at front plate:	$0.754 \cdot 10^{5}$	$0.667 \cdot 10^{5}$
Measured recoils (PRT counts/monitor count)	$1.295 \cdot 10\text{-}^{2}$	$1.529 \cdot 10^{-3}$
Neutrons/sr at source / monitor count	620192.59	557722.78
Fluence at front plate (n/cm^2/monitor count)	976.59	101.83

Table 16: Output of the program PRTelescope.exe and resulting PRT fluences.

The table shows an immediately obvious difference between the measured neutron fluences for the two distances. Testing with the $1/r^2$ rule, the neutron fluences at the front plate per monitor count give ($fluence_{252mm}$ / $fluence_{740mm}$) = 9.58, while $(740/252)^2$ = 8.62, a difference of about 11%.

Large uncertainties may be introduced by the low-statistics run 11 and in the correction of the FC influence in run 12. By rejecting these runs from the calculation of the recoil

proton rate at 740 mm, we get ($fluence_{252mm}$ / $fluence_{740mm}$) = 9.59, a slightly larger difference from the distance ratio than before.

The stability of the monitor detector during the PRT runs was checked against the other two monitor detectors, i.e. the scintillator and the ^{3}He counter.
For runs 10-13 both the monitor and the PRT were very stable, with a deviation of 0.66% of the long counter against both the scintillator and the ^{3}He counter.
Unfortunately no data exist for runs 3 and 4 from either of the two supplementary monitors, so no conclusions can be drawn about any possible stability problems there.

In summary, because of the inconsistency of the PRT measurements, the current data do not permit a reliable calculation of the absolute neutron fluence of the experiment. Therefore they cannot be used as a reference for the estimation of the FC neutron detection efficiencies.

3. CONCLUSIONS

Although the absolute neutron detection efficiencies of the fission chambers were not achieved due to problematic PRT data, several useful secondary conclusions can be drawn from the April 2009 measurements.

The main improvement comes from the confirmation that the time-of-flight technique, with the use of the pulsed beam and gating on the timing distributions, discards the large background component that was observed in the January 2009 data. The resulting detected neutron rates are highly consistent with the $1/r^2$ rule, which is particularly encouraging for the case of the more complex chamber FC200.
Further background rejection can be obtained for more precise efficiency measurements.

Additional validation was achieved for the procedure applied to calculate the total number of fission fragments from the amplitude spectra. A threshold of roughly the middle of the plateau is satisfactory and the use of approximate, even negative, offset values does not introduce any noticeable complications.
Both methods of simulating the fission fragment distribution near and below threshold produce consistent results with acceptable uncertainties. Better statistics would be helpful to clarify the differences between the two techniques and provide details on the shape of the distribution at and below threshold.

6. Fission Chamber Measurements January 2009

C. Rouki, A. Plompen, and M. Stanoiu

The fission chamber installed at the 200m station of flight path 3 of the GELINA accelerator as part of the GAINS setup has been calculated to have an efficiency of 0.984(16) [1]. Recent GEANT4 simulations [2] contradict this value, estimating a 10% offset.
In order to evaluate these claims, the chamber was used for neutron flux measurements at the Van de Graaff accelerator in January 2009 with continuous monoenergetic beams of 1.25 and 2.5 MeV. A detailed assessment of the acquired fission spectra and the methodology used for their analysis is presented here.
Two more fission chambers were tested in the same experiment, which allowed for the additional study of different chamber configurations and varying distances between the fissionable deposits and the corresponding collecting electrodes.
The resulting neutron rates were tested for consistency with respect to the neutron fluence measured by a reference proton recoil telescope.

Contents

1. EXPERIMENTAL DETAILS

Three fission chambers were tested in the experiment:
1. FC300: the test chamber installed at the 300m station of flight path 3
2. FC200: the fission chamber used for the GAINS setup (flight path 3, 200m station)
3. FC30: the fission chamber installed at the 30m station of flight path 16

Only the measurements taken with the first two chambers will be covered in detail here. The experimental details of the FC30 and PRT measurements will only be summarised.

The proton recoil telescope (PRT) provided by the Van de Graaff facility was used as the reference instrument for the neutron flux measurements in order to determine the absolute efficiency values for the chambers.

The same data acquisition system was used for all three chambers and the proton recoil telescope, and was measured to have negligible dead time (<1%).
A second acquisition system was used for a BF_3 detector and a long counter monitor, both used to monitor the variations of the neutron beam. After several cycles showing a large noise component for the BF_3 counter, it was decided to use only the long counter data for beam monitoring.

A. FC300

The 300m fission chamber houses 2 different configurations of UF_4 foil-collection plates:
1) Two single-sided deposits (#9 and #11) placed on either side of a collection plate. The positive bias is applied on the electrode and the UF_4 foils are grounded.
2) A grounded double-sided UF_4 deposit (#8) placed at equal distances between two positively biased electrodes.

The UF_4 deposits are all from the same batch (Lot 680), prepared by vacuum evaporation on 20 μm Al foils of 70 mm diameter and supported by 84 mm diameter rings. The chamber is operated with a continuous flow of P10 gas at atmospheric pressure.

Details on the FC300 deposits are presented in Table 1:

	Thickness (μg/cm^2)			Activity	Isotopic composition (%)				
foil	U	^{235}U	UF_4	(Bq)	^{233}U	^{234}U	^{235}U	^{236}U	^{237}U
8/side1	473(1)	472(1)	625(2)	2966(8)	<0.001	0.036	99.94	0.011	0.013
8/side2	471(1)	471(1)	624(2)	2958(8)					
8 average	472(1)	472(1)	625(2)	2962(8)					
8 total	944(2)	943(2)	1249(3)	5924(12)					
11	475(1)	475(1)	629(1)	2983(6)					
9	469(1)	469(1)	621(2)	2945(9)					

Table 1: Characteristics of the UF_4 deposits of FC300.

The construction of the chamber permitted relatively easy access to the interior and the configuration of FC300 was modified several times during the experiment (Figures 2-5, 7).

A summary of the measurements carried out with this chamber is presented in Table 2 and details are given in the following sections (i)-(v).

run	E_n (MeV)	Foils in FC300	Run time (s)	Distance from source (mm)	Test description
3	1.25	8, 9, 11	56428	974	1.25 MeV measurement
14	2.50	8, 11	74482	984	Configuration test
17	2.50	8, 11	54741	983	Configuration test
18	2.50	8, 11	89717	985	Configuration test
19	no beam	8, 11	1800	985	α background measurement
20	no beam	8, 11	8167	985	α background measurement
21	2.50	8, 9, 11	53955	984	Distance test
27	2.50	8, 9, 11	1890	208.5	Distance test
28	2.50	8, 9, 11	1822	402	Distance test
29	2.50	8, 9, 11	1800	608	Distance test
30	2.50	8, 9, 11	6987	1004	Background measurement
31	2.50	8, 9, 11	1804	1004	Background measurement
32	2.50	8, 9, 11	1800	1004	Background/Distance test
33	2.50	8, 9, 11	1800	801	Distance test

Table 2: Measurements carried out with FC300. The fifth column indicates the distance between the centre of the chamber's front window and the neutron source.

i) E_n=1.25 MeV measurement

One measurement was taken with the 1.25 MeV neutron beam (run 3).
Online observation of the amplitude spectra of the single-sided foils (#9, #11) showed a distribution with a double-humped shape (Figure 1), indicating unequal charge collection distances for the two deposits.

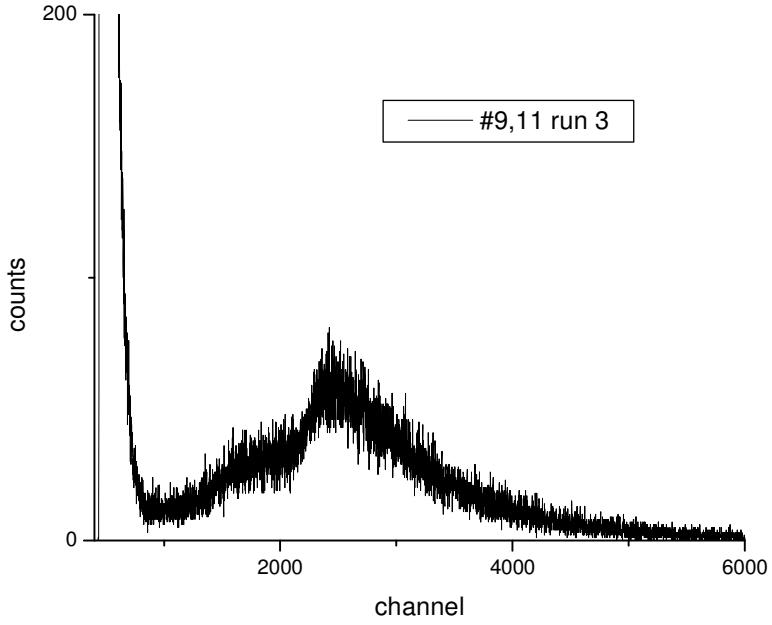

Figure 1: Amplitude distribution of foils #9, #11 for the 1.25 MeV neutron beam measurement (run 3).

On opening the chamber it was found that it had the wrong configuration (Figure 2). There was no collecting plate between the two foils and the positive bias had been applied to #11, while #9 was grounded.

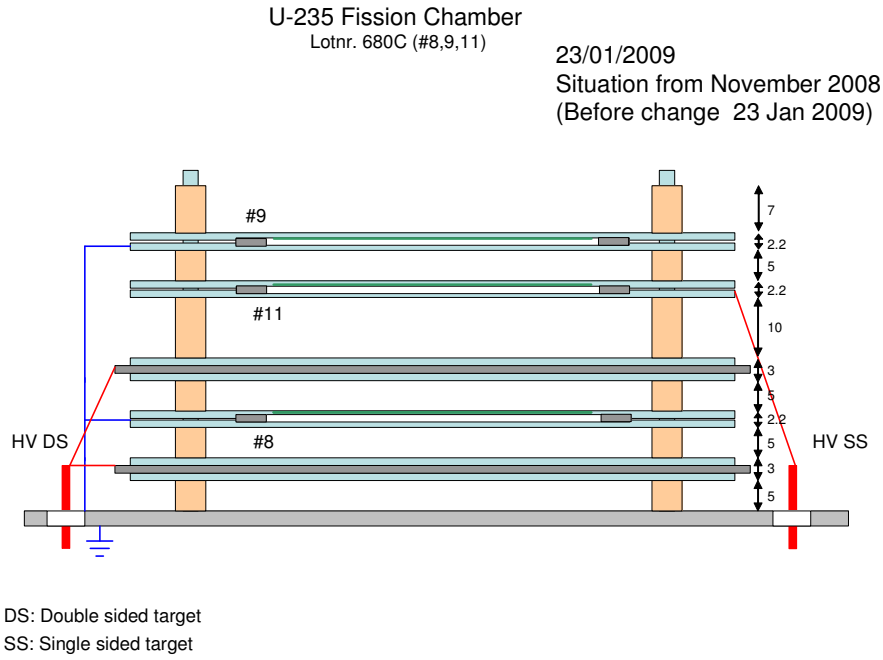

Figure 2: FC300 at the beginning of the January measurements. The wrong configuration of the single-sided foils was corrected after run 3.

The configuration of the chamber was modified with the addition of a 1 mm thick positively biased electrode opposite #11 (Figure 3) and further tests were carried out.

The double-sided foil #8 was left unchanged during this modification.

ii) Configuration test

This test was carried out to examine the effect of the distance between a UF_4 deposit and the corresponding collecting electrode, and to determine the optimum spacing between them.

Deposit #9 was removed and three measurements (Table 3) were taken with the configuration of Figure 3 at E_n=2.5 MeV. Using spacers of 5, 6 and 7 mm, the distances between deposit 11 and the electrode were varied by 1 mm in each run. The fission chamber remained at about the same distance from the source.

run	Distance #11-plate (mm)	Run time (s)	Distance to source (mm)
14	5.5	74482	984
17	6.5	54741	983
18	7.5	89717	985

Table 3: Configuration test runs, with foil #11 at different distances from the collecting electrode.

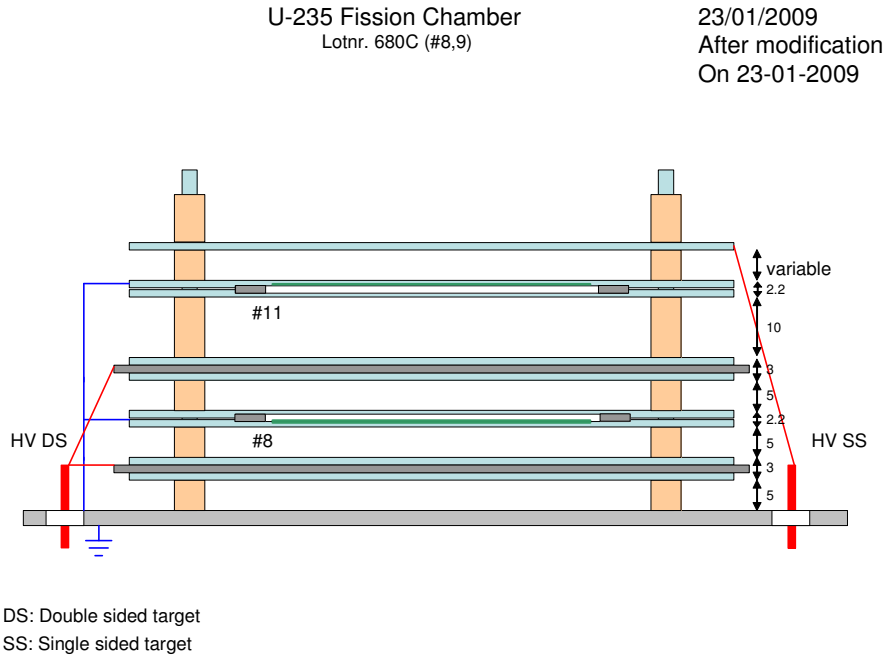

Figure 3: Arrangement of FC300 during the configuration test.

iii) Alpha background measurement

A background measurement was taken with no neutron beam and with the chamber configuration of run 18 (distance #11-electrode: 7.5 mm).

iv) Distance test

The configuration of the chamber was changed again and foil #9 was added (Figures 4, 5). Both single-sided foils were placed at 6.5 mm on either side of the collecting plate.

The configuration of the double-sided foil was also altered to adjust the distance between #8 and the two electrodes to 6.5 mm. An error occurred at this point and the double-humped shape appeared in the amplitude spectra of #8 in the subsequent runs (Figure 6).
The chamber was next opened in April 2009 and it was confirmed that this modification resulted in different spacing of 6.8 and 7.5 mm between the foil and the electrodes (Figure 7). The mistake was due to the misconception that the deposit was facing the flange, when it was actually facing the window of the chamber.

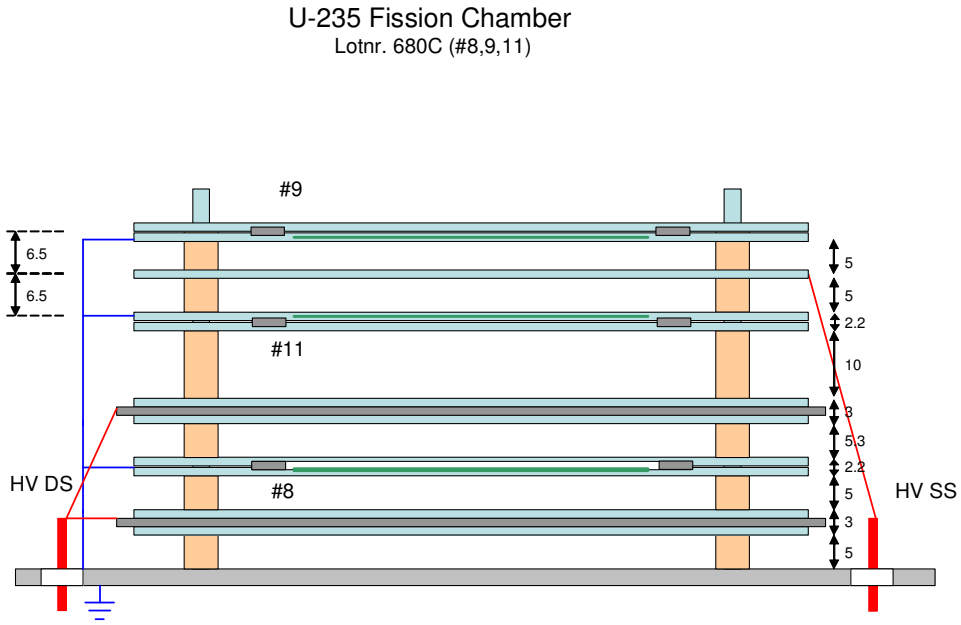

Figure 4: The final configuration of the single-sided foils #9 and #11 in FC300.

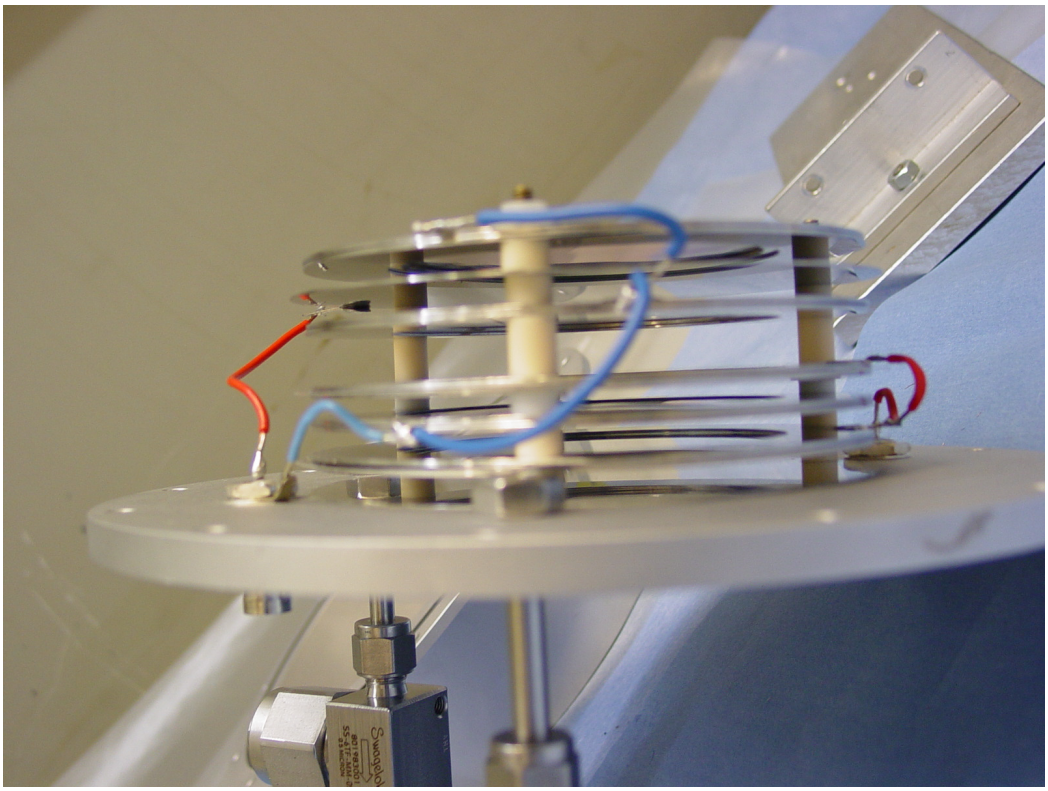

Figure 5: the interior of FC300 with the single-sided foils at 6.5 mm from the collecting plate.

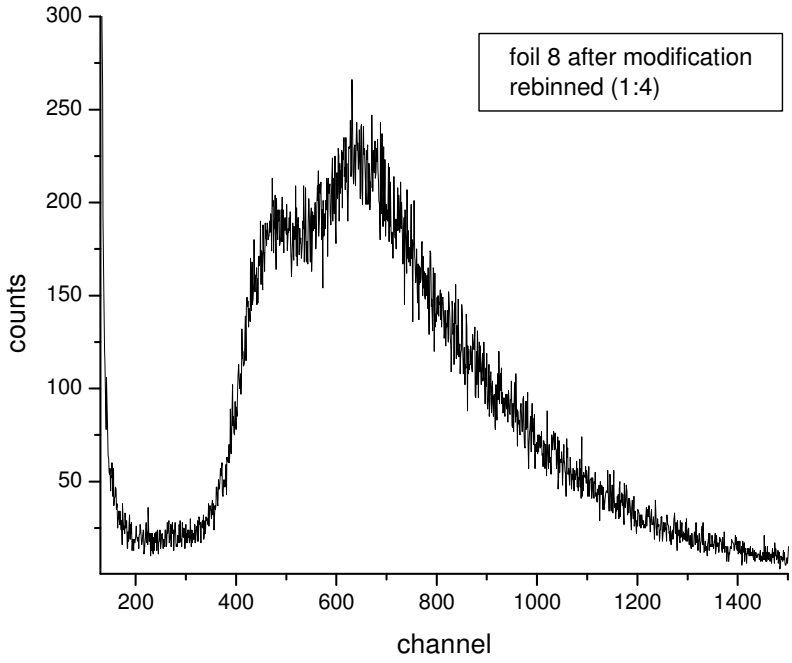

Figure 6: amplitude distribution of the double-sided foil #8 after the last modification of January 2009.

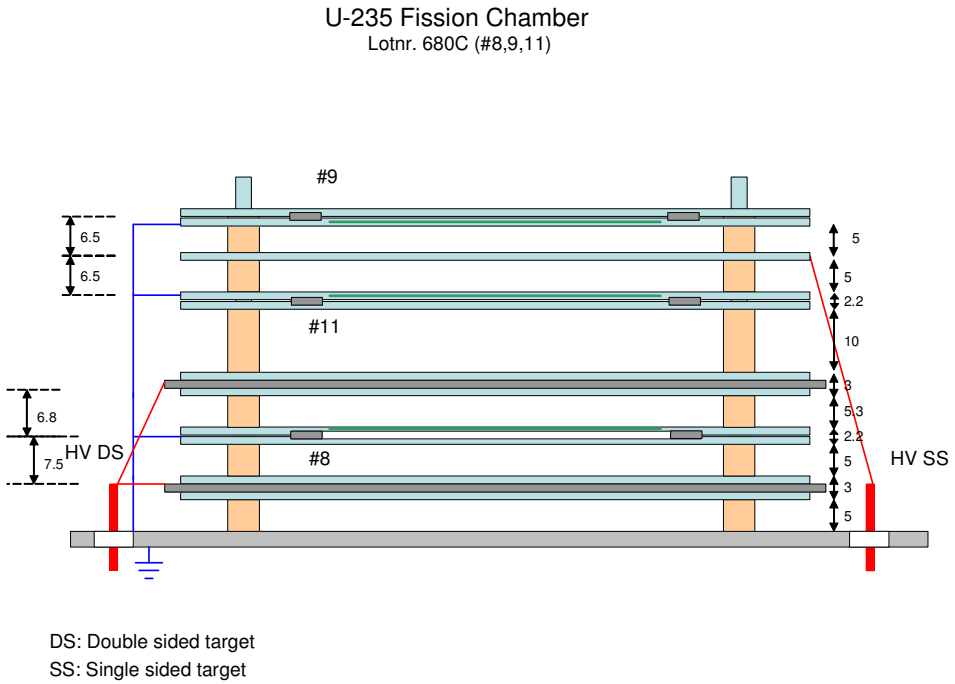

Figure 7: the actual configuration of FC300 after the final modification of January 2009.

For the current tests the distance of FC300 from the neutron source was varied between 20-100 cm, and short (mostly 30-minute) neutron rate measurements were taken at E_n=2.5 MeV with the chamber's window perpendicular to the beam axis.
The purpose of these tests was to confirm the $1/r^2$ dependence of the measured neutron rates on the distance r from the source, and to compare the measurements with the neutron fluence observed by the proton recoil telescope for efficiency calculations.

v) Neutron background measurement

Neutron background measurements (runs 30-32) were carried out with a 40x20x10 cm^3 paraffin and Li_2CO_3 brick placed on a metal support leg in front of the chamber (run 30). The effect of the support alone was measured during run 31.
The paraffin block was used as a shadow bar substitute, and was considered to completely shield the chamber from direct source neutrons. This assumption is only an approximation and the measurement is only used as an indication of the neutron background level.

B. FC200

The fission chamber of the FP3/200m station contains an assembly of 8 UF_4 deposits (Table 4) of 70 mm diameter, arranged on 5 Al foils of 20 µm thickness (Figure 8). The two single-sided deposits are placed at the two ends of the chamber facing inwards, and the 3 double-sided foils are contained between them at equal spacing of 6 mm. All deposits are from the same batch (Lot 929), manufactured by vacuum evaporation.
Positive and negative voltages are alternated between foils and the P10 gas in the chamber is kept at atmospheric pressure.

	Thickness (µg/cm²)			**Isotopic composition (%)**			
foil	**U**	**^{235}U**	**UF_4**	**^{234}U**	**^{235}U**	**^{236}U**	**^{237}U**
foil1_side1	422(3)	421(3)	558(3)				
foil2_side1	419(2)	419(2)	555(3)				
foil3_side1	421(3)	421(3)	558(3)				
foil1_side2	383(2)	383(2)	507(3)				
foil2_side2	383(2)	382(2)	507(3)	0.062	99.826	0.036	0.073
foil3_side2	383(2)	382(2)	507(3)				
foil4	327(2)	326(2)	432(3)				
foil5	327(2)	327(2)	433(2)				
FC200 total	3066(6)	3061(6)	4058(8)				
FC200 average	383(2)	383(2)	507(3)				

Table 4: Characteristics of the UF_4 deposits of FC300.

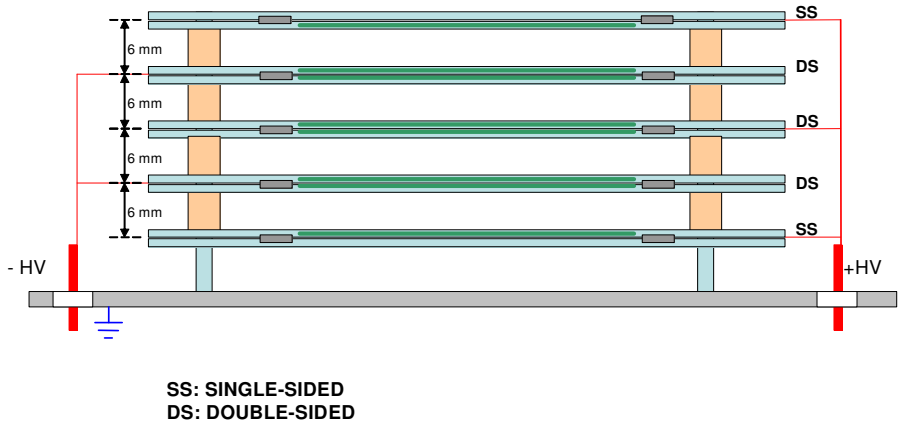

Figure 8: Approximate schematic representation of the FC200 chamber.

The following measurements were taken with FC200:

run	E_n (MeV)	Run time (s)	Distance from source (mm)	Test description
1	1.25	1753	1040	1.25 MeV measurement
2	1.25	5400	1001	1.25 MeV measurement
12	2.50	47477	997	Distance test
35	2.50	1800	209	Distance test
34	2.50	1800	402	Distance test
36	2.50	1800	604	Distance test
37	2.50	2525	998	Background measurement
38	2.50	957	998	Background measurement
39	2.50	896	998	Background/Distance test

Table 5: Measurements made with FC200. The fourth column denotes the distance of the chamber's front window to the neutron source.

Approximate background measurements were made with two 40x20x10 cm^3 blocks of paraffin and Li_2CO_3 placed on a metal support (run 37) in front of the chamber. During run 38 the bricks were removed to measure the effect of the support.

C. FC30

The configuration and characteristics of FC30 are shown in Figures 9, 10.

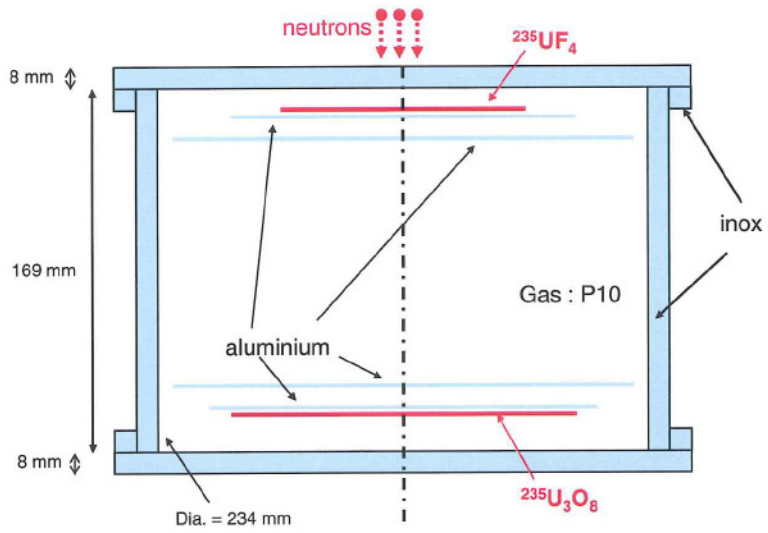

Figure 9: schematic diagram of the FC30 chamber. From [2].

The evaporated UF_4 deposit of FC30 is from the same batch (Lot 989, Table 5) as the FC200 foils, while the U_3O_8 foil (Lot 89) was prepared by spray-painting and consists of >99.5% ^{235}U atoms.

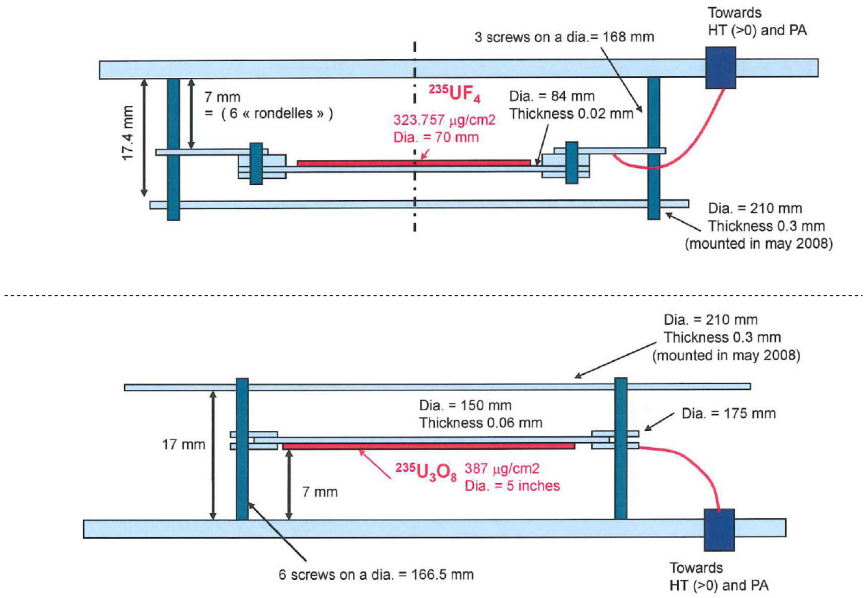

Figure 10: the ^{235}U deposits of FC30 and corresponding electrodes in detail (from [2]).

The following measurements were taken with FC30:

run	E_n (MeV)	Run time (s)	Distance from source (mm)	Test description
4	1.25	76154	985	1.25 MeV measurement
7	1.25	45049	985	1.25 MeV measurement
13	2.50	93472	1013	2.5 MeV measurement
22	2.50	16296	987	2.5 MeV measurement
23	2.50	5267	987	Dead time measurement
24	2.50	3380	987	Dead time measurement
25	2.50	1820	490	2.5 MeV measurement
26	2.50	46946	490	2.5 MeV measurement

Table 6: Measurements made with chamber FC30. The fourth column denotes the distance of the chamber's front window to the neutron source.

The configuration of the chamber was modified twice before runs 7 and 22 to change the spacing between deposits-electrodes. The dead time of the system was measured as <1%.

D. PRT

The measurements made with the proton recoil telescope are summarised in Table 7.
Runs 6, 9 and 16 were background measurements, taken with the Ta foil of the PRT inverted.
The characteristics of boxes 1/5 and 1/11 of the PRT are shown in Table 8.

run	E_n (MeV)	Run time (s)	Distance from source (mm)	Test description
5	1.25	3600	250	Box 1/5
6	1.25	3600	250	Box 1/5, Ta foil inverted
8	2.50	7200	250	Box 1/11
9	2.50	7200	250	Box 1/11, Ta foil inverted
15	2.50	8602	350	Box 1/11
16	2.50	7857	350	Box 1/11, Ta foil inverted

Table 7: Measurements made with the proton recoil telescope.

	Box 1/5	Box 1/11
Radiator foil	Tristearin	Tristearin
Radiator foil thickness (mg/cm^2)	0.7476	1.5026
Radiator H-content (cm^{-2})	$0.5494 \cdot 10^{20}$	$0.1104 \cdot 10^{21}$
Radius of radiator (mm)	12.5	12.5
Distance radiator-detector (mm)	85.0	85.0
Thickness of Ta backing (mm)	0.10	0.10
Radius of detector (mm)	12.5	12.5
Thickness of Al window (mm)	0.50	0.50
Gas	95%Ar, 5% CO_2	95%Ar, 5% CO_2
Gas pressure (mbar)	48.1	87.9
Wire HV (V)	1200	1200

Table 8: Physical characteristics of the PRT boxes used in the experiment.

2. DATA ANALYSIS

The following sections describe the data analysis for the chambers FC300 and FC200.
The FC30 and PRT data were analysed separately, and while the detailed analysis will not be presented here, the resulting fluence measured by the PRT will be used as a reference for the fission chamber efficiencies. For the 2.5 MeV neutron beam this value was given as 661935.7 neutrons/srad per monitor count at the position of the source [3].

A typical fission chamber pulse height distribution is shown in Figure 11. The large alpha peak in the low amplitudes is separated from the broad fission fragment region by an effectively flat area (plateau). The spectrum includes all events with non-zero amplitudes.

The beam neutrons interact with the ^{235}U of the UF_4 foils through an (n, f) reaction. In the energy region that the chambers are operated, the reaction has a relatively stable cross-section, with $\sigma_{(n, f)} = 1.26$ b at 2.5 MeV [4].
The neutron rate detected by the fission chamber is determined from the total number of fissions taking place. In order to reproduce the full fission spectrum from the raw amplitude distributions, the following analysis steps are used:

1. Definition of plateau limits: channels for the low (L) and high (H) limits of the plateau are located, so that the region between them is mostly flat and free from alpha background. The selection of L, H and the uncertainty that it introduces to the results are examined in more detail in sections A-i and A-iii.
2. Definition of threshold C: According to [5], if P is the channel of the fission peak, then a threshold C = 0.45P is effective for achieving full fission-alpha separation and completely removing the alpha background.
   This assumption was tested in detail in section A-iii, and compared to a threshold in the centre of the plateau. For all examined spectra the channel 0.45P was found to be within the plateau and near its centre, so this method was adopted for the largest part of the analysis.

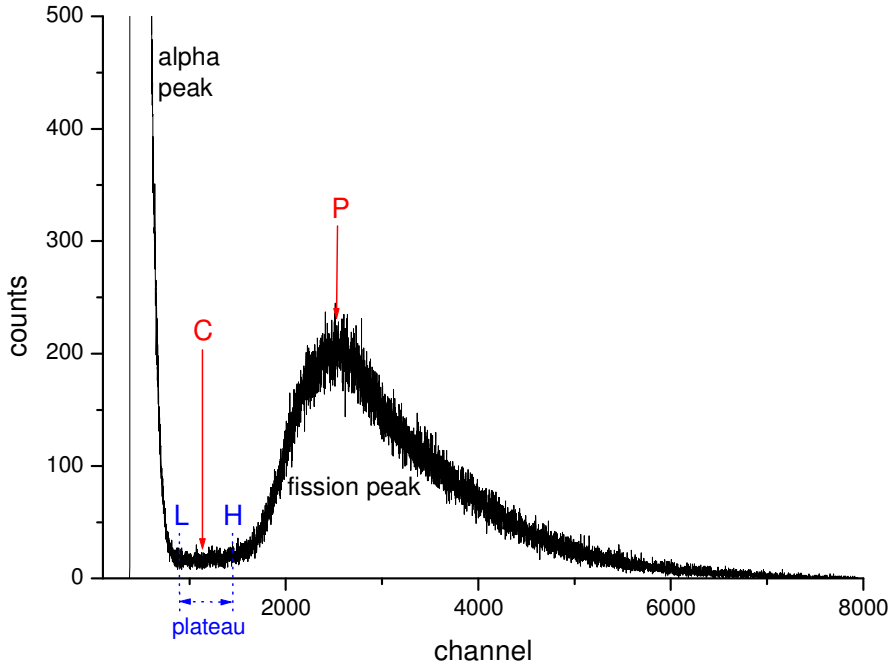

Figure 11: Typical raw amplitude distribution of a fission chamber, and the related threshold and plateau.

3. Fissions above threshold: The integration of the amplitude distribution above the threshold C gave the number Y of fission fragments above threshold.

4. Fissions below threshold: Following the technique of [5], the distribution is extrapolated horizontally from C to zero pulse height (Figure 12) to reproduce the fission fragment spectrum below threshold. The distribution below threshold is considered constant and equal to the average number of counts per channel in the plateau (Av), as calculated between channels L and H. The integration of this region produces the number Y_A of fissions below threshold.
   An alternative method of calculating Y_A is examined in section A-iii.

5. Fragments that stop in the deposit: To the total number ($Y+Y_A$) of fission fragments determined from the spectra, a small fraction Y_B must be added, to account for the fission fragments that stop in the UF_4 foils without depositing energy in the gas.
   According to the [6], the inefficiency of 2π counting for evaporated UF_4 is:
   $\Delta_{UF_4} = (10.5 \pm 0.7) \cdot t\,(\%)$, where t is the UF_4 thickness of the deposit in mg/cm^2.
   A correction factor $F=1-\Delta_{UF4}$ was applied as $Y+Y_A+Y_B=(Y+Y_A)/F$.
   From the thickness and isotopic compositions of the used deposits shown in Tables 1 and 4, the corrections are:

   Δ_{UF4}(#11) = 0.0660 ± 0.0044 or F(#11) = 0.9340
   Δ_{UF4}(#9,11) = 0.0656 ± 0.0044 F(#9,11) = 0.9344
   Δ_{UF4}(#8) = 0.0656 ± 0.0044 F(#8) = 0.9344
   Δ_{UF4}(FC200) = 0.0533 ± 0.0036 F(FC200) = 0.946

   For the double-sided deposit 8, the pair (#9, #11) and for FC200, the average UF_4 thicknesses were used.

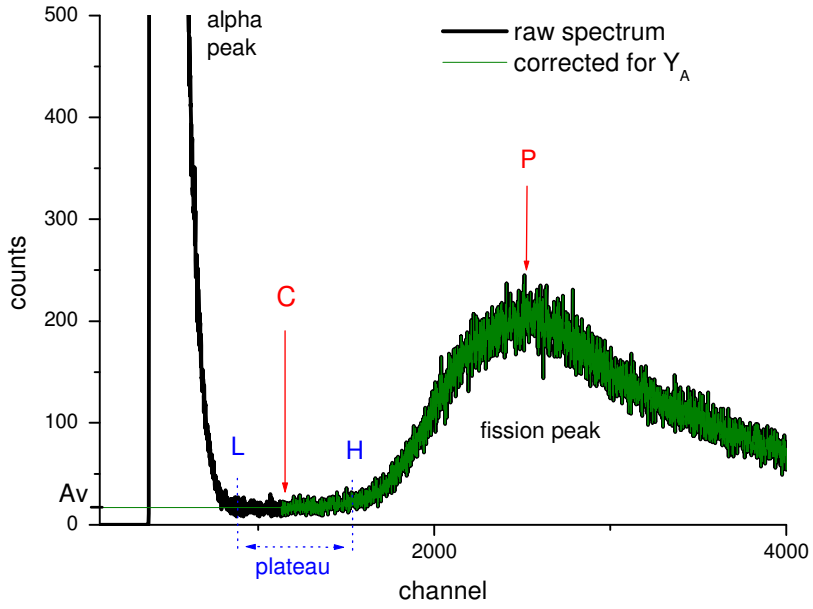

Figure 12: The distribution of Figure 11 corrected for the fission fragments below threshold.

All data were normalised to the yield of the long counter, which presented unexpected electronic noise during some measurement cycles. The affected data were discarded to ensure the stability and consistency of the system for all measurements.

A. FC 300m

i) Alpha background measurement

For deposit #11, the largest part (99.998%) of the background events was located below channel 800 in the 8192 channel spectrum. Above this limit the background count rate was $2 \cdot 10^{-3}$ s^{-1}, which amounts to162 counts for run 18, or 0.08% of the measured events in that region. Therefore the requirement L>800 is expected to reject the largest part of the background (Figure 16). The same condition was applied when both single-sided foils #9, #11 were used.
For foil #8, the background was mostly (99.994%) concentrated below channel 840 (in the 8k spectrum), and the count rate above that limit was 10^{-3} s^{-1}. For all #8 spectra the condition L>840 was applied. (Figure 17).

ii) E_n=1.25 MeV measurement

a) Single-sided deposits (#9, #11)

As mentioned earlier, foils 9 and 11 had the wrong configuration during run 3 and presented the double-humped shape of Fig. 1, typical of two different charge collection distances.

In spite of the ambiguity in locating channel P, and the rather narrow plateau of about 300 channels (in the 8k spectrum), a threshold of 0.45P appears sufficient to separate the fission peak from the alpha background (Figure 13).

Although this measurement is not very constructive, the analysis results are shown in Table 9 as a reference. The ratio between the height of the fission peak and the average yield in the plateau region is very low, while a high fraction of the fissions lies below threshold.

run	Peak/plateau ratio	$Y_A/(Y+Y_A)$	$(Y+Y_A+Y_B)$/monitor
3	4.9	12.1(2) %	$1.30(4)\cdot 10^{-2}$

Table 9: Analysis results for foils #9, #11 of FC300 for E_n=1.25 MeV.

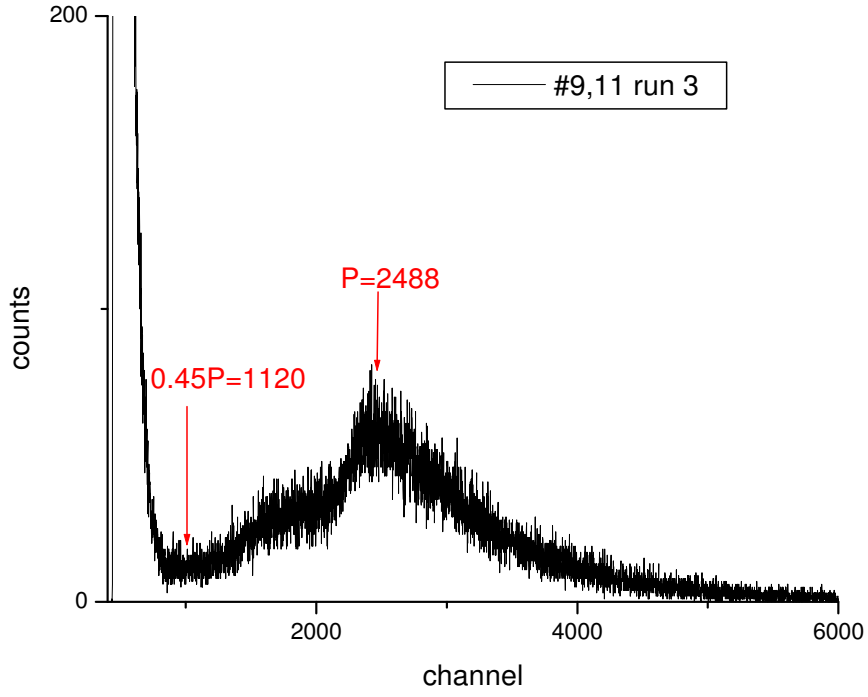

Figure 13: Applied threshold of 0.45P for the single-sided deposit spectrum of run 3.

Due to the shape of the fission spectra, the height of the fission peaks in all the acquired distributions can only be defined approximately, and its ratio over the height of the corresponding plateaus is given here just as an indication of the quality of each measurement.

b) Double-sided deposit (#8)

The pulse-height distribution of foil #8 at 1.25 MeV is shown in Figure 14.

The spectrum has a wide and well-defined plateau, and the channel 0.45P lies roughly in the middle of the flat region, offering good separation between fissions and alphas.

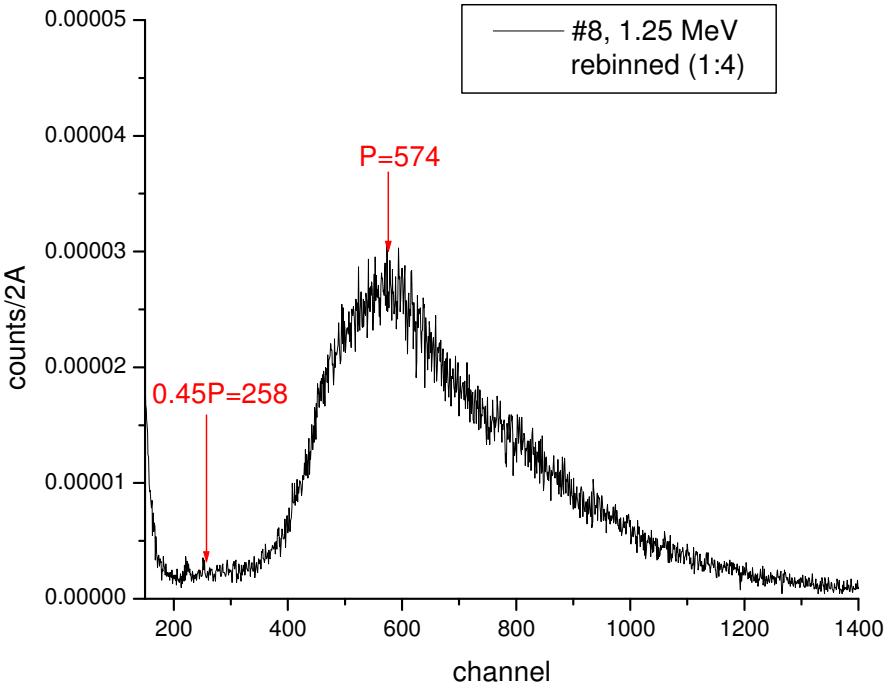

Figure 14: Pulse-height distribution of #8 for run 3. The indicated channels refer to the rebinned (1:4) spectrum.

The data analysis shows a high peak/plateau ratio (Table 10), and the resulting total fission yield compares well with that measured by the single-sided deposits (Table 9).

run	Peak/plateau ratio	$Y_A/(Y+Y_A)$	$(Y+Y_A+Y_B)$/monitor
3	11.9	5.0(1) %	$1.285(4)\cdot10^{-2}$

Table 10: Analysis results for foil #8 of FC300 for E_n=1.25 MeV.

iii) Configuration test

a) Single-sided deposit (#11)

The amplitude spectra of the single-sided deposit #11 for the three different distances to the collecting electrode are drawn together in Figure 15.

As shown in Figures 15 and 16, the area between channels 200-300 in the rebinned 2k spectra (channels 800-1200 in the original 8k spectra) was reasonably flat for all three runs and mostly free from background when compared to the spectra of runs 19 and 20 (Fig. 16). These channels were used as plateau limits for all three spectra.

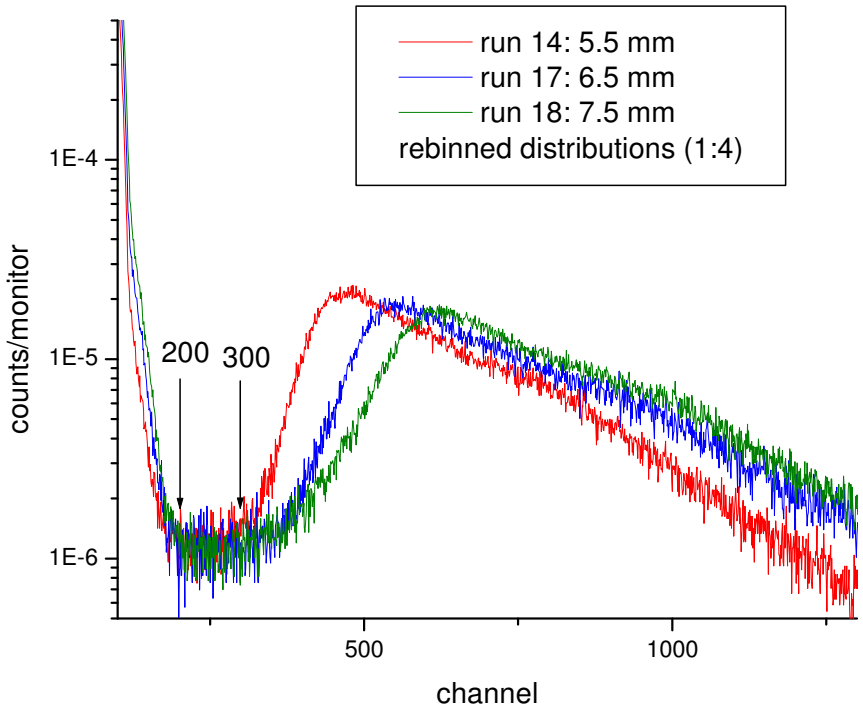

Figure 15: Rebinned (1:4) amplitude distributions of foil 11 for runs 14, 17, 18 in counts/monitor.

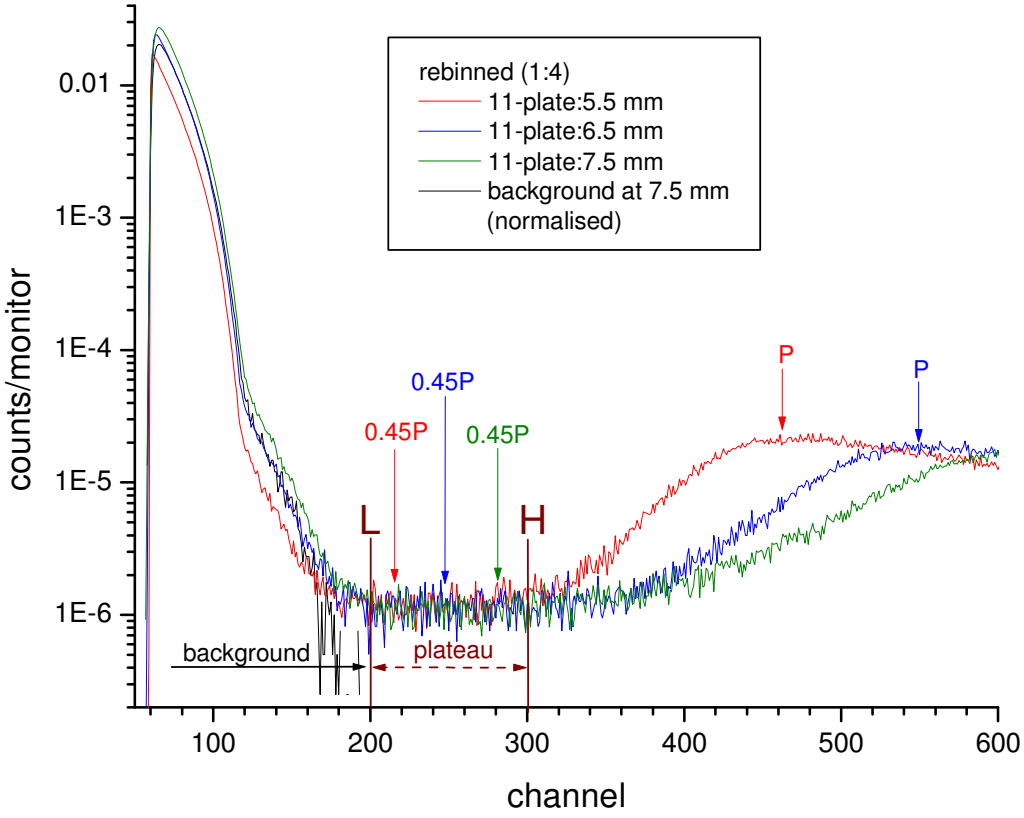

Figure 16: The low energy part of Figure 15, with the limits of the used plateau. The measured background distribution (runs 19, 20) is also displayed, rescaled to the alpha peaks of runs 14, 17, 18.

For these measurements a more systematic analysis was applied, comparing two different approaches in fitting the region below threshold to reproduce the full fission spectrum.
In detail, the two examined methods are:

1. C=0.45P, flat distribution in plateau y = Av = constant

As described earlier, the threshold is determined as C = 0.45P, and the distribution is extended horizontally from C to zero pulse height. The results of this method are shown in Table 11.

run	P	L	H	C=0.45P	Av	$Y_A/(Y+Y_A)$	$(Y+Y_A)$/monitor	$(Y+Y_A+Y_B)$/monitor
14	1848	800	1200	832	7.5(1)	3.4(1) %	$7.81(2)\cdot10^{-3}$	$8.36(2)\cdot10^{-3}$
17	2196	800	1200	988	4.6(1)	3.7(1) %	$7.80(2)\cdot10^{-3}$	$8.35(2)\cdot10^{-3}$
18	2488	800	1200	1120	7.3(1)	4.1(1) %	$7.79(2)\cdot10^{-3}$	$8.35(2)\cdot10^{-3}$

Table 11: Configuration test analysis results for foil 11, assuming a threshold of 0.45P and a flat plateau. The channel numbers refer to the original 8192 channel spectrum.

The three configurations show excellent agreement in terms of total yield values $(Y+Y_A+Y_B)$/monitor, with a standard deviation of 0.09%.
The average fraction $Y_A/(Y+Y_A)$ is 3.7(1) %.

2. C = (L+H)/2, linear fit of plateau y = a·x + b

In this case the threshold C is positioned at the centre of the plateau, and the distribution in the plateau region is fitted with the linear function: yield = a·(channel) + b between L and H.
The number Y_A is calculated from the relation: $Y_A = (a/2)C^2 + bC$.
This method gives the values of Table 12:

run	L	H	C	a	b	$Y_A/(Y+Y_A)$	$(Y+Y_A)$/monitor	$(Y+Y_A+Y_B)$/monitor
14	800	1200	1000	$3.5\cdot10^{-3}$	4.1	3.1(8) %	$7.74(6)\cdot10^{-3}$	$8.29(7)\cdot10^{-3}$
17	800	1200	1000	$1.1\cdot10^{-4}$	4.5	4(2) %	$7.8(2)\cdot10^{-3}$	$8.4(2)\cdot10^{-3}$
18	800	1200	1000	$-2.5\cdot10^{-4}$	7.6	3.7(6) %	$7.80(5)\cdot10^{-3}$	$8.35(6)\cdot10^{-3}$

Table 12: configuration test analysis results, assuming a threshold of C = (L+H)/2 and a linear fit of the plateau.

The standard deviation of the $(Y+Y_A+Y_B)/monitor$ values of Table 12 is 0.4%, and the differences from the corresponding results of Table 11 are in the order of 0.3%.
The average fraction $Y_A/(Y+Y_A)$ in this case is 0.035(21).

The most important feature of the above analysis is the exceptional agreement between the total fission yields for all three configurations. This suggests that the separation between the UF_4 foil and the electrode is practically unrelated to the resulting total fission rate.

Another significant attribute is the excellent agreement between the two techniques in the values of the total fission rate $(Y+Y_A+Y_B)/monitor$, in spite of the differences (average 9.3%) between the corresponding fractions $Y_A/(Y+Y_A)$.

The first method shows a slight advantage due to the lower uncertainties and the higher consistency between the three measurements, but both approaches seem satisfactory for reproducing the full fission spectrum.

The details of the uncertainty calculations for the above datasets made with the two methods are presented in Table 13 (cases 1, 2).
In addition, a more comprehensive analysis of the effects of the applied plateau limits was made by various shifts in the channels C, L and H (Table 13, cases 3-5).

In detail, the following test cases are presented in Table 13:

- The distribution in the plateau and below threshold is constant b=Av and
  1. C = 0.45P, L = 800, H = 1200
- The plateau and the distribution below threshold are fitted linearly with the relation: counts = a·(channel) + b, and
  2. C = (L+H)/2, L = 800, H = 1200
  3. C = 0.45P, L = 800, H = 1200
  4. C = (L+H)/2, L = 800, H = 1000
  5. C = (L+H)/2, L = 1000, H = 1200

The uncertainty of Y_A is calculated by the relation:

$$u^2(Y_A) = \left[\frac{u(a)}{2}C^2\right]^2 + [u(b)C]^2 + \left[\frac{u(a)}{2}C^2\right][u(b)C]C_{ab}$$

The offset for all spectra in this experiment is considered 0.
The uncertainties u(a), u(b) of a, b and the correlation coefficient C_{ab} are provided directly by the fitting programs.

case	L	H	C	a x10^{-3}	u(a) x10^{-3}	b	u(b)	C_{ab}	Y_A	u(Y_A)
Run 14										
1	800	1200	832			7.5	0.1		6272	118
2	800	1200	1000	3.5	1.2	4.1	1.2	0.14	5817	1406
3	800	1200	832	3.5	1.2	4.1	1.2	0.14	4599	1130
4	800	1000	900	2.2	3.3	9.1	2.9	-0.05	9068	2926
5	1000	1200	1100	6.6	3.6	0.6	4.0	0.13	4694	4983
Run 17										
1	800	1200	988			4.6	0.1		4590	115
2	800	1200	1000	0.1	1.0	4.5	2.3	0.01	4592	2388
3	800	1200	988	0.1	1.0	4.5	2.3	0.01	4537	2358
4	800	1000	900	2.3	2.9	2.6	1.0	0.06	3243	1516
5	1000	1200	1100	-0.9	2.7	5.6	2.6	-0.02	5631	3329
Run 18										
1	800	1200	1120			7.3	0.1		8175	148
2	800	1200	1000	-0.3	1.2	7.5	1.2	-0.01	7425	1286
3	800	1200	1120	-0.3	1.2	7.5	1.2	-0.01	8299	1476
4	800	1000	900	3.6	3.0	3.2	3.3	0.09	4372	3242
5	1000	1200	1100	2.7	2.8	4.3	3.1	0.06	6351	3884

Table 13: Data analysis results and uncertainty calculations for the configuration test runs, examining 5 examples of different initial plateau settings.

case	$\frac{u(Y_A)}{Y_A}$	Y	$Y+Y_A$	$Y_A/(Y+Y_A)$	$(Y+Y_A+Y_B)$/monitor x10^{-3}	$\frac{u(Y+Y_A+Y_B)}{Y+Y_A+Y_B}$	deviation
Run 14							
1	1.9%	180866	187138	3.4(1) %	8.36(2)	0.2%	-0.07%
2	24.2%	179701	185518	3.1(8) %	8.29(7)	0.8%	0.79%
3	24.6%	180866	185465	2.5(6) %	8.28(5)	0.7%	0.82%
4	32.3%	180420	189488	5(2) %	8.5(1)	1.6%	-1.33%
5	106.1%	178960	183654	3(3) %	8.2(2)	2.7%	1.79%
Run 17							
1	2.5%	118842	123432	3.7(1) %	8.35(2)	0.3%	-0.02%
2	52.0%	118770	123362	4(2) %	8.4(2)	2.0%	0.04%
3	52.0%	118842	123379	4(2) %	8.4(2)	1.9%	0.02%
4	46.7%	119239	122482	3(1) %	8.3(1)	1.3%	0.75%
5	59.1%	118304	123935	5(3) %	8.4(2)	2.7%	-0.43%
Run 18							
1	1.8%	193365	201540	4.1(1)%	8.35(2)	0.2%	0.09%
2	17.3%	194204	201629	3.7(6)%	8.35(6)	0.7%	0.05%
3	17.8%	193365	201664	4.1(7)%	8.35(6)	0.8%	0.03%
4	74.1%	194944	199316	2(2)%	8.3(1)	1.6%	1.20%
5	61.2%	193515	199866	3(2)%	8.3(2)	2.0%	0.92%

Table 13 (continued from previous page). The last column gives the standard deviation of the values $(Y+Y_A+Y_B)$ for each separate case.

The comparison of cases 1 and 2 shows systematically lower uncertainties involved in the first method (flat plateau) for calculating Y_A. Otherwise, the two techniques largely coincide and give an average fraction of fissions below threshold of 3.6%.

Regarding case 3, where the linear fit method is employed with the C=0.45P threshold, the resulting total fission yields and related uncertainties are generally closer to those of case 2. Nonetheless there is excellent agreement with both the first two cases, which confirms that the channel 0.45P is a good choice for threshold, even when it is not located very close to the centre of the plateau (i.e. run 18).

For the last two cases, where the linear fit is applied to the lower (case 4) and upper (case 5) half of the plateau respectively, as expected the involved uncertainties are generally higher. Nevertheless, the total fission rates $(Y+Y_A+Y_B)/monitor$ are still in very good agreement with the first three calculations, and do not involve more than 2.7% uncertainty.
This is especially encouraging, since it allows for reliable results even for spectra where the plateau limits are difficult to define precisely.

A notable feature of Table 13 is that in spite of the very high uncertainties involved in some of the calculated Y_A values, these are not reflected to the final total fission rates $(Y+Y_A+Y_B)$/ monitor. As cases 1-3 show, with the initial plateau limits and either of the two methods, the uncertainty $u(Y+Y_A+Y_B)/(Y+Y_A+Y_B)$ is no higher than 2%, with an average value of 0.8%.

In all the following, only the flat plateau method with C=0.45P is used to calculate Y_A.

b) Double-sided deposit (#8)

During the configuration test of the single-sided foil, the double-sided deposit #8 remained unchanged, measuring neutrons with E_n=2.5 MeV. The amplitude distributions for the three runs are shown in Figure 18, and the data analysis results in Table 14.
In the current analysis a common plateau between channels 900-1300 was used for all 3 runs.

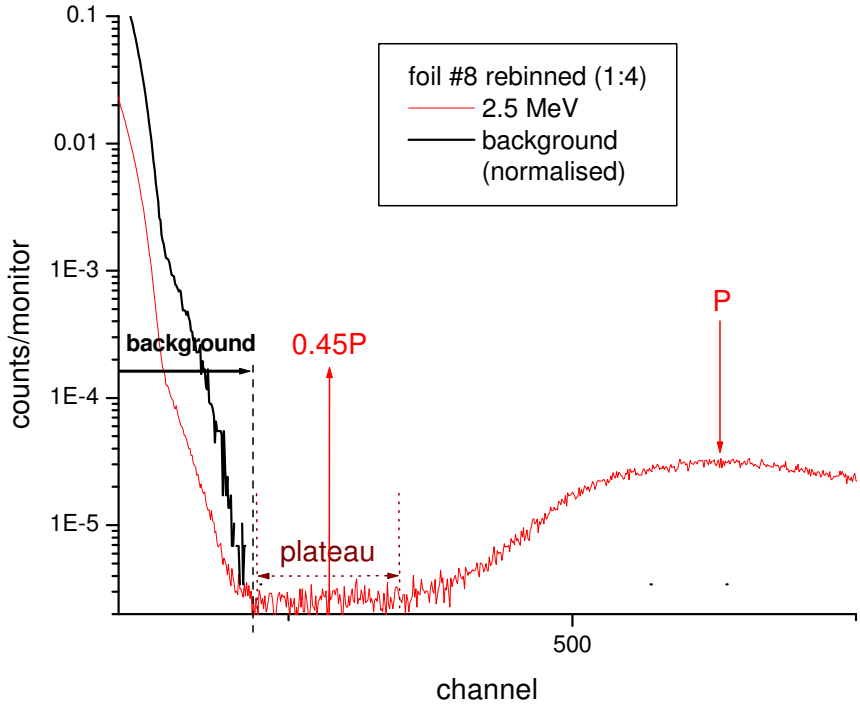

Figure 17: The pulse height distribution for foil #8 at E_n=2.5 MeV and background (from runs 19, 20).

run	Peak/plateau ratio	$Y_A/(Y+Y_A)$	$(Y+Y_A+Y_B)$/monitor
14	12.3	4.89(6) %	$1.655(3)\cdot10^{-2}$
17	11.8	4.75(7) %	$1.652(3)\cdot10^{-2}$
18	12.6	4.81(5) %	$1.649(3)\cdot10^{-2}$

Table 14: Data analysis results for foil #8 during the configuration test runs 14, 17 and 18.

The resulting total fission rates agree very well (deviation 0.2%), although there is an obvious difference in Figure 18 between the distribution of run 14 and those of runs 17, 18.

The first three cycles of run 14 were rejected to eliminate any effects from possible incomplete flushing of the chamber - however, the consistency of the foil 11 data for all three runs makes this assumption rather unlikely.
The stability of the system against the monitor counter was also checked and confirmed for all used cycles.
It appears more probable that the ADC settings for foil #8 were modified at some point after run 14 and before the start of run 17, which created this shift in the spectrum.

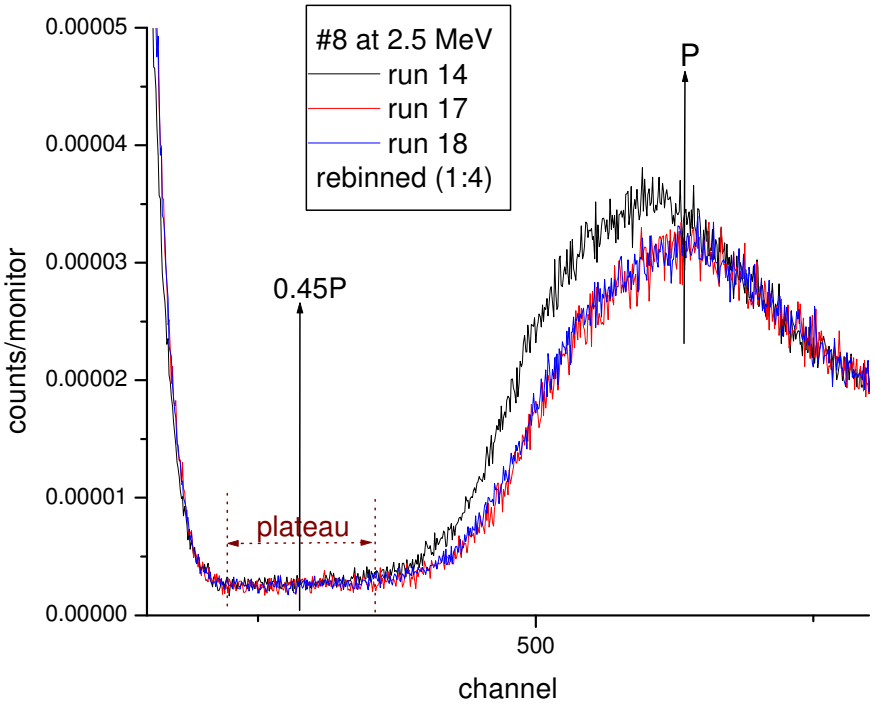

Figure 18: Amplitude distributions per monitor count of deposit #8 for runs 14, 17, 18.

In comparison to the E_n=1.25 MeV distribution (Figure 19), the higher fission rates of the current measurements are to be expected, since the neutron-induced fission cross-section of ^{235}U increases with neutron energy. ENDF VIIB gives $\sigma_{(n,f)}$=1.19 b at E_n=1.25 MeV and $\sigma_{(n,f)}$=1.26 b at E_n=2.5 MeV.

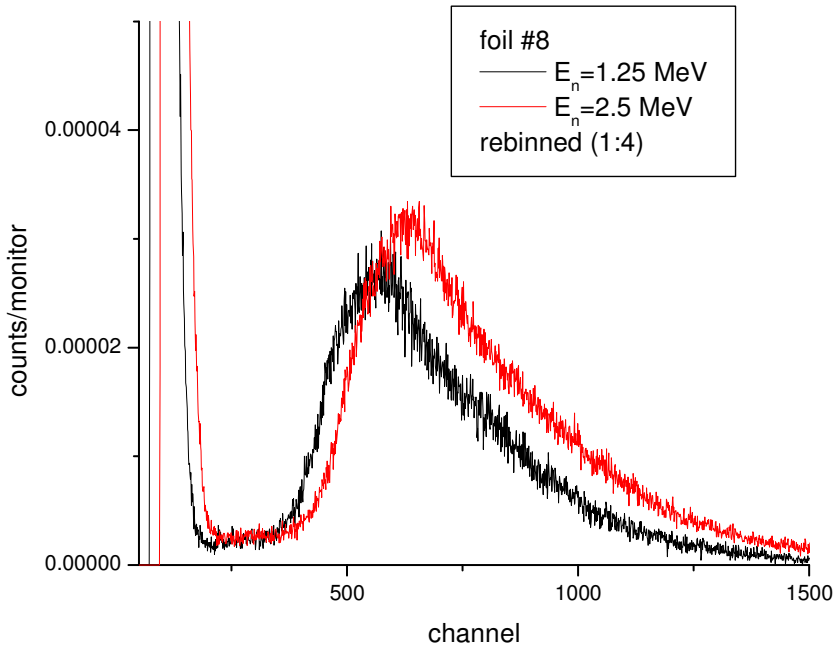

Figure 19: comparison of the spectra of deposit #8 for neutron energies 1.25 MeV and 2.5 MeV.

iv) Distance test

The number of neutrons/cm^2 N detected by a $^{235}UF_4$ deposit is deduced from the total number of fissions ($Y+Y_A+Y_B$) in the chamber by the expression:

$$N = \frac{Y + Y_A + Y_B}{\sigma_{(n,f)} \cdot A(^{235}U)}$$

where A(^{235}U) the number of ^{235}U atoms in the deposit and $\sigma_{(n,f)}$ the neutron-induced fission cross section of ^{235}U at this energy. The corresponding neutron flux is given by N divided with the chamber's efficiency.
The related rates presented here correspond to the above numbers per monitor count.

When expressing the measured neutron rates in relation to the distance from the source, an additional correction is needed to account for several geometrical and physical features of the experimental setup.
Here the correction accounts for the extended surface of the foil and incorporates the angle dependence of the fluence, the ^{235}U(n,f) cross section and a 5% inhomogeneity of the deposit.

For simplicity in the calculations this correction is applied on the distance R of the deposits from the neutron source, and the corrected distance R' equals:

$$R' = \frac{R}{1 - \sqrt{1655.84/R^2}}.$$

a) Single-sided deposits (#9, #11)

The pulse height distributions of foils #9 and #11 for the distance test runs are shown in Figures 20, 21.
Since the same chamber configuration was used, all spectra are expected to have identical characteristics when it comes to the positions of the fission peak and the plateau. It is also helpful to use the same analysis settings for a more direct comparison between measurements.

Figure 20 shows all distributions plotted together and rescaled by the factors shown in the parentheses. The spectra appear to coincide, although the low-amplitude detail (bottom graph) shows a visible increase in the tail of the alpha peak with the distance from the source. This is expected, since the fraction of the background increases with distance, but it requires additional attention in defining L.

Each distribution was considered separately and the average peak and threshold channels were found to adequately describe all (Figure 21). The channels L=800, H=1200, P=2218 and C=1000 (in 8192-channel spectra) were used in all the analysis.

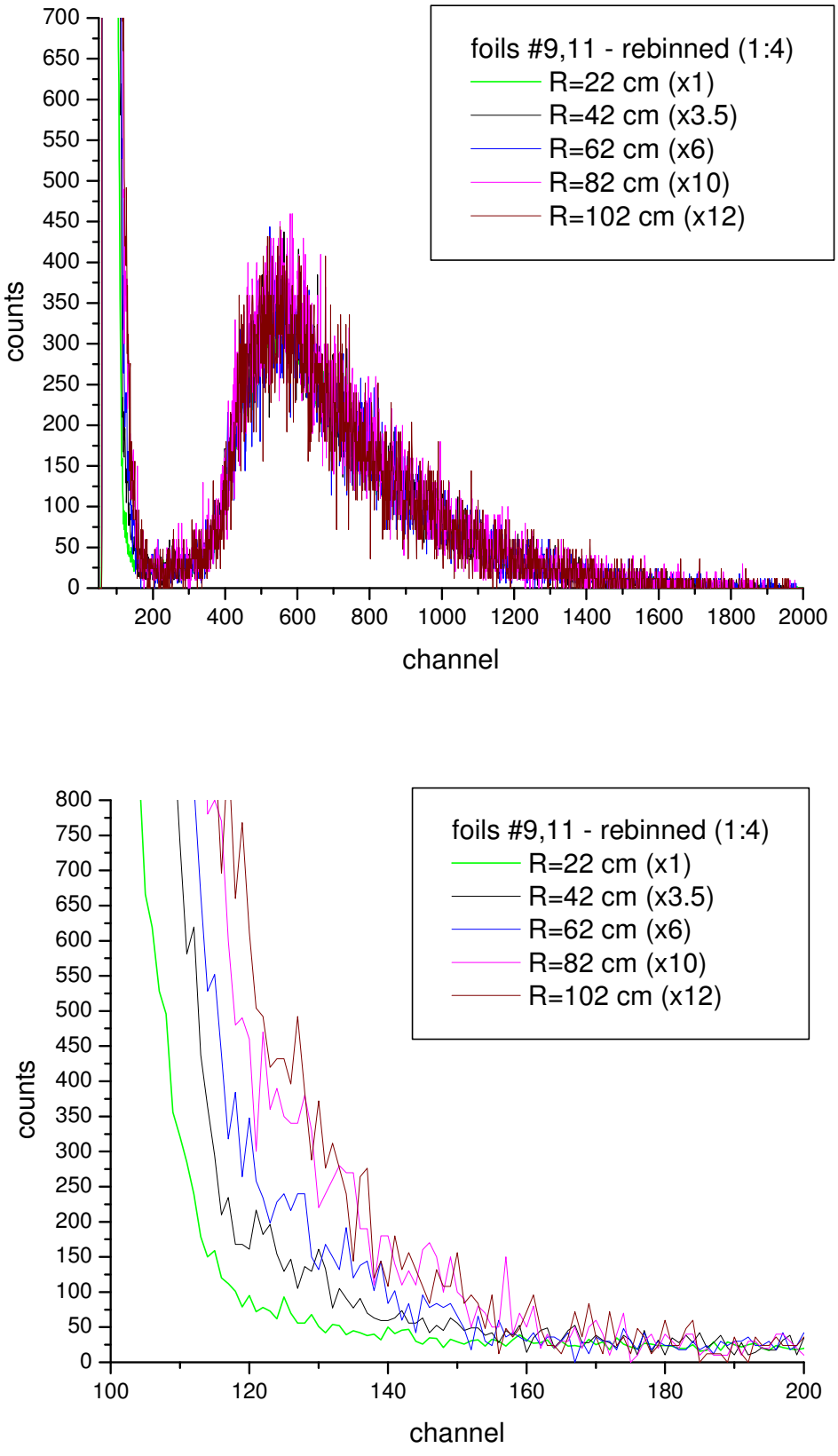

Figure 20: Amplitude distributions of foils #9, 11 for the distance test runs. The channel axis is rebinned (1:4) and all spectra have been rescaled by the indicated factors to coincide. Bottom: detail of the top graph, showing the lower part of the plateau and the variation of the tail of the alpha peak.

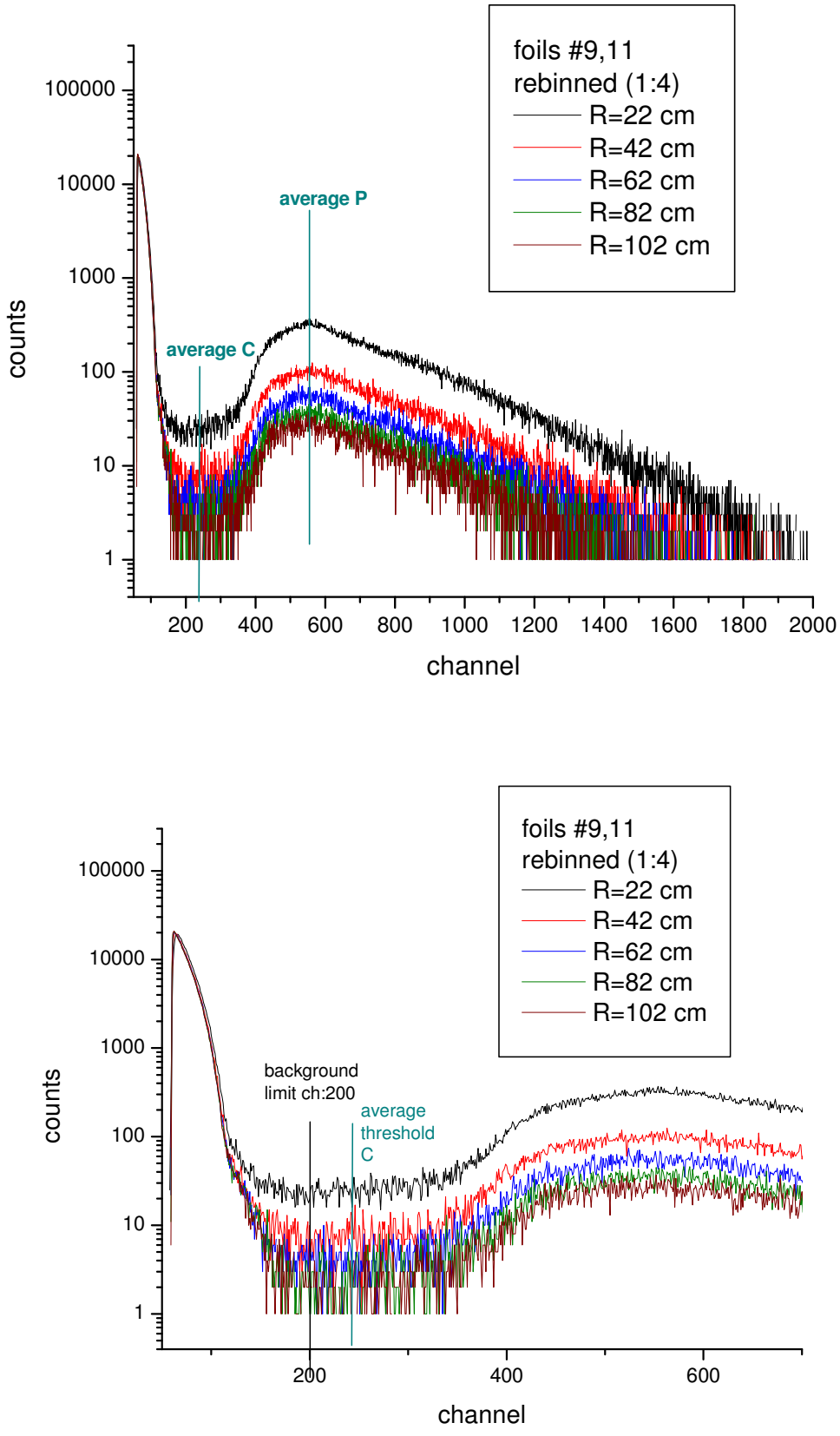

Figure 21: Amplitude distributions of foils #9, #11 for the distance test runs, and the average peak (P) and threshold (C) channels used in the analysis. Bottom: detail of the top graph showing the lower amplitudes, the applied threshold C and the background limit.

The analysis results are shown in Table 15.
The second and third columns of the Table show the distances between the centre of the neutron source and the centre of the collecting electrode (Figure 7) between foils 9 and 11.

run	R (cm)	R' (cm)	Peak/plateau	$Y_A/(Y+Y_A)$	$(Y+Y_A+Y_B)$/monitor	(neutrons/cm^2)/monitor
21	99.9	100.0	13.2	4.3(1) %	$1.70(3)\cdot10^{-2}$	145.1(3)
27	22.3	22.7	13.2	4.4(1) %	$1.8(5)\cdot10^{-1}$	1492(4)
28	41.7	41.9	11.3	4.2(2) %	$5.9(3)\cdot10^{-2}$	499(2)
29	62.3	62.4	13.4	4.02) %	$3.1(2)\cdot10^{-2}$	263(2)
32	101.9	102.0	16.0	3.6(3) %	$1.6(1)\cdot10^{-2}$	139(1)
33	81.6	81.7	15.0	4.0(4) %	$2.1(2)\cdot10^{-2}$	178(1)

Table 15: Data analysis results for the distance test of foils #9, 11 of FC300.

The measurements give good peak/plateau ratios for all spectra and very low uncertainties in the resulting total yield values.
The average fraction $Y_A/(Y+Y_A)$ is 4.1(5) %, in agreement with the value 3.7(1)% that resulted from the configuration measurements (Table 11). The average of all the related values calculated with the flat plateau method is 4.0(5) %.

The measured neutron rates are plotted against the corrected distance R' in Figure 22.

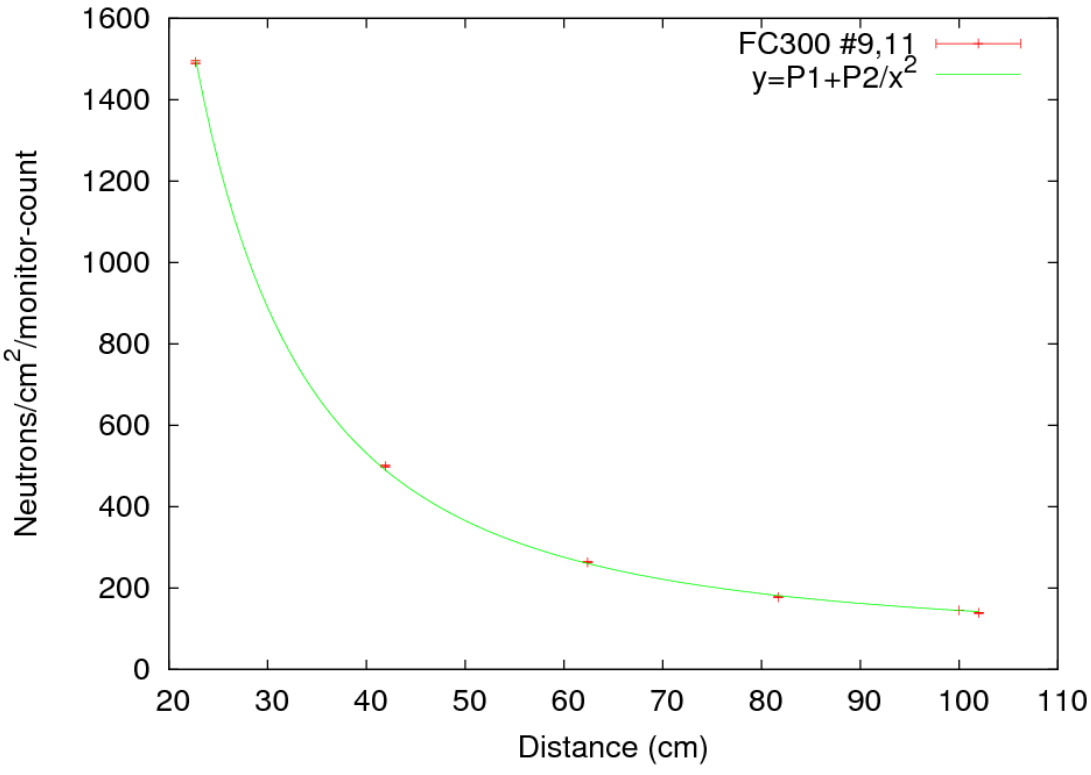

Figure 22: :easured neutron rates for #9, #11 with respect to distance from the source.

Fitting this dataset with the function $y = P_1 + P_2/x^2$, where y: detected neutron rate, x: distance from source in cm, gives the parameters of Table 16.

P_1	$u(P_1)$	P_2	$u(P_2)$	C_{12}	Reduced χ^2
71.4	1.1	735672	5821	-0.7	8.6

Table 16: Fit parameters for the data of Table 15 with the function $y= P_1 + P_2/x^2$. C_{12} is the correlation coefficient of the fit.

Although the $1/r^2$ rule is respected and a good fit is achieved, two important features emerge:

- The parameter P_1 is unexpectedly large, indicating a high background component in the measured neutron field.
- The parameter P_2, which is a measure of the neutron source strength, is also very high compared to that measured by the PRT.
  Using the PRT value as a reference (neutron fluence of 661935.7 neutrons/srad per monitor count), the efficiency of deposits #9, #11 is calculated as 111%.
  Since the PRT is a well calibrated instrument regularly used for reference measurements, this inconsistency can only be related to the fission chamber data.

b) Double-sided deposit (#8)

Deposit #8 had the wrong configuration of Figure 7 during the distance tests.
Because of this, an additional difficulty appears in defining correctly the peak channel for these distributions, and therefore the thresholds C=0.45P.
Fortunately this problem is counteracted by the very wide and well-defined plateaus of the spectra (Figure 23). By choosing the highest point of the fission area as channel P, channel 0.45P was always found to be located near the middle of the plateau and above the background limit (Figures 23-25).

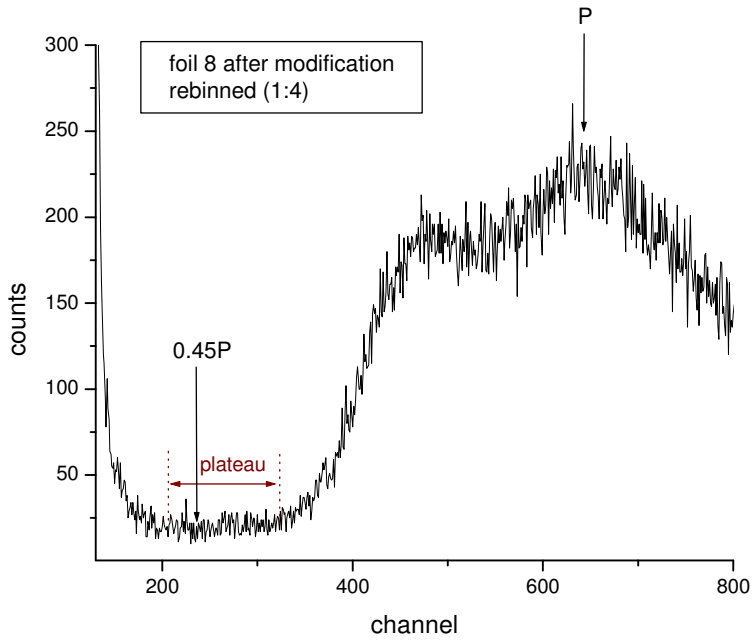

Figure 23: Amplitude distribution of foil #8 with the wrong configuration of Figure 7.

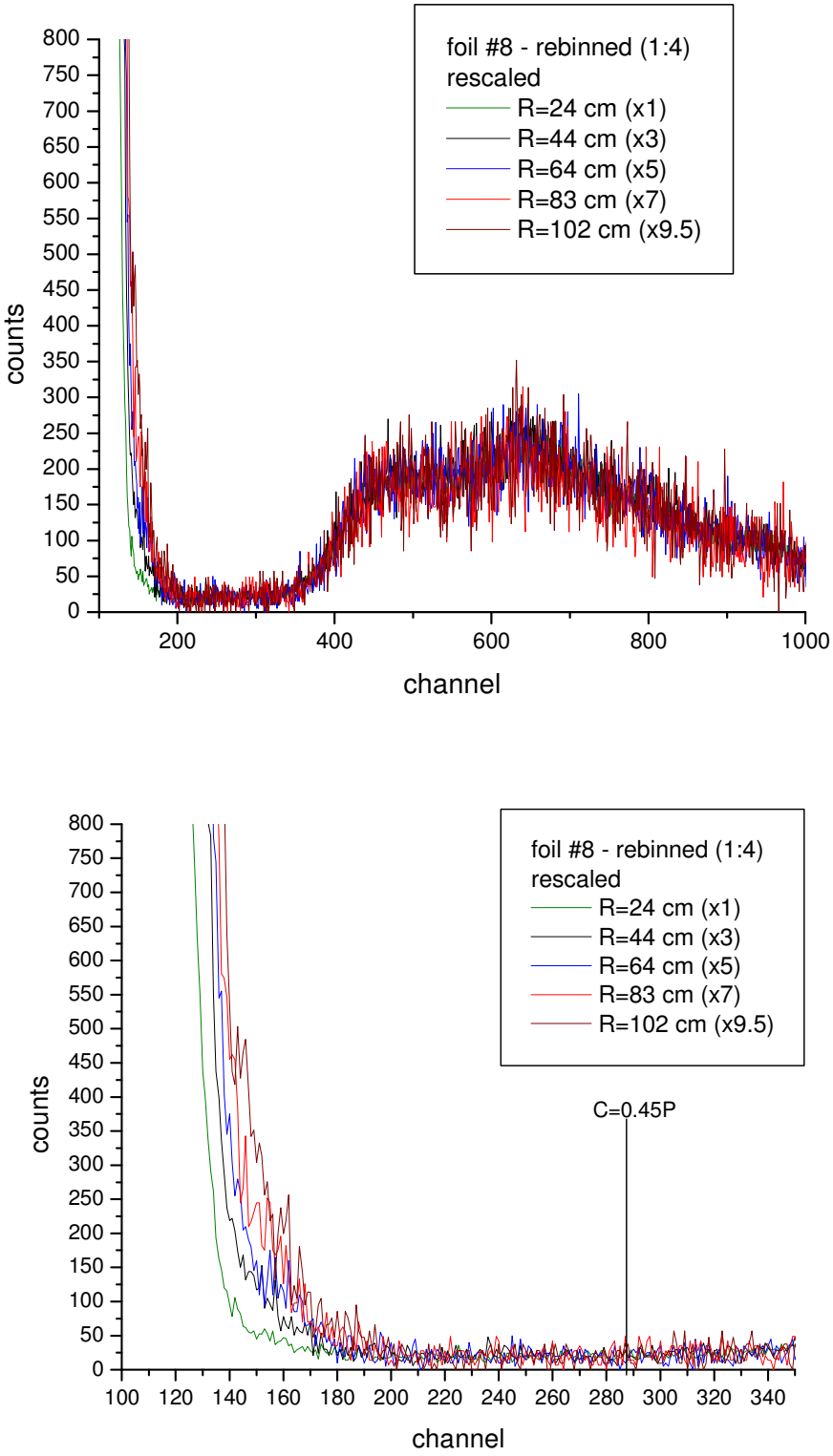

Figure 24: Amplitude distributions of foil #8 for the distance test runs. The spectra have been rescaled by the indicated factors to coincide. Bottom: detail of the top graph, showing the lower part of the plateau and the variation of the tail of the alpha peak. The applied threshold is indicated.

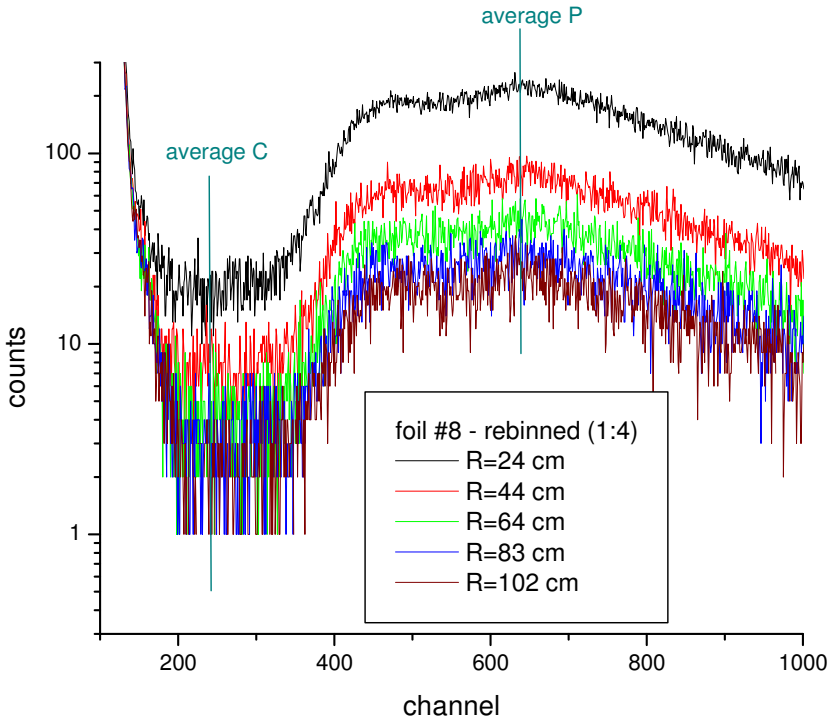

Figure 25: Amplitude distributions of foil #8 for the distance test runs, and the average peak (P) and threshold (C) channels used in the analysis.

The common plateau limits used in the analysis were L=900, H=1350, C=1148 (in the 8192-channel spectrum). The results are shown in Table 17.

run	R (cm)	R' (cm)	Peak/plateau	$Y_A/(Y+Y_A)$	$(Y+Y_A+Y_B)$/monitor	(neutrons/cm^2)/monitor
21	101.6	101.7	11.0	5.0(1) %	$1.664(3)\cdot10^{-2}$	141.9(3)
27	24.1	24.4	10.9	4.9(1) %	$1.46(4)\cdot10^{-1}$	1242(4)
28	43.4	43.6	12.5	5.2(2) %	$5.41(3)\cdot10^{-2}$	462(2)
29	64.0	64.1	12.3	4.8(2) %	$2.94(2)\cdot10^{-2}$	251(2)
32	103.6	103.7	13.4	4.7(3) %	$1.62(1)\cdot10^{-2}$	138(1)
33	83.3	83.4	10.5	5.7(3) %	$2.09.(2)\cdot10^{-2}$	178(1)

Table 17: Data analysis results for the distance test runs of foil #8 of FC300.

The effect of the double-humped peak appears to be reflected on the peak/plateau ratio, which is 14% lower than that of deposits #9, #11. Otherwise, the wrong configuration of #8 does not seem to present any perceptible complications in achieving reasonable results from the data. The average fraction $Y_A/(Y+Y_A)$ is 5.0(5) %. This value remains unchanged when including the results of Table 14.

Fitting the neutron rates of Table 17 with the relation (neutron rate) = $P_1 + P_2/R'^2$ (Figure 26) gives the parameters of Table 18:

P_1	$u(P_1)$	P_2	$u(P_2)$	C_{12}	Reduced χ^2
74.2	1.8	703990	1013	-0.7	22.65

Table 18: Fit parameters for the data of Table 17 with the function $y= P_1 + P_2/x^2$.

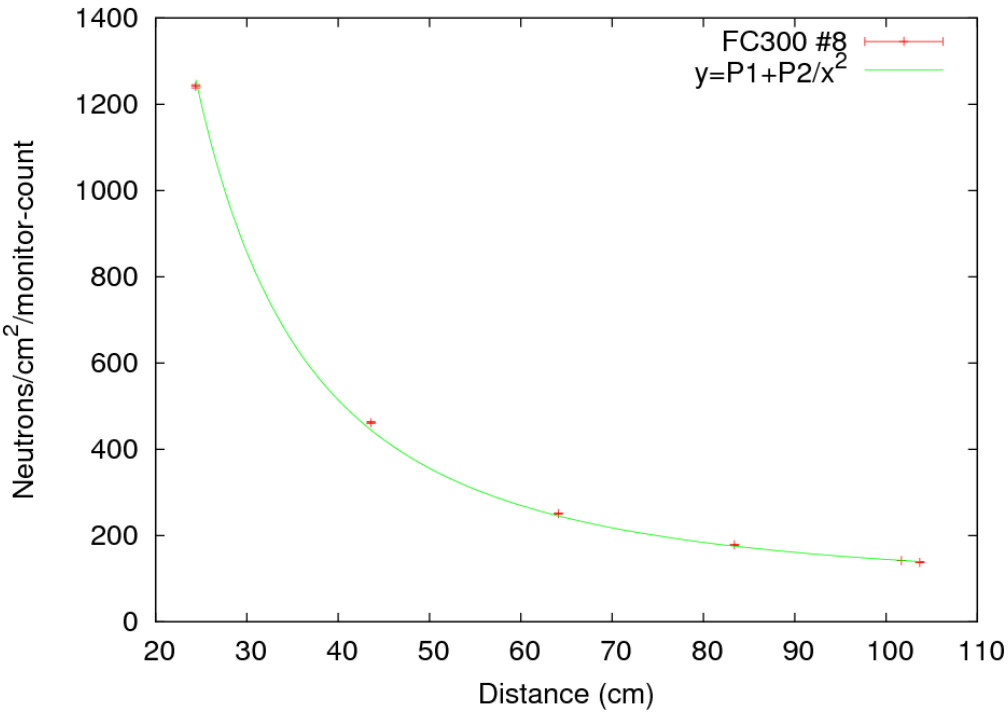

Figure 26: Measured neutron rates for deposit #8 with relation to the distance from the source.

In this case the fit is not as good as for foils #9, #11, however the same conclusions apply. There is a large background component P_1 that differs from that of #9, #11 by only 4%, while the comparison with the PRT data gives a neutron detection efficiency of 106%.

v) Neutron background measurement

The most suitable measurement to shed light on the high neutron background indicated by the above fits is the shadow bar test of runs 30-32.

The paraffin block placed in front of the chamber is considered to completely shield the chamber from the source neutrons.
To measure the effect of the paraffin brick alone, the distributions of run 30 (brick on the support, in front of FC300) were subtracted from those of run 31 (only the support in front of the chamber). The results were then compared to those of run 32 (fission chamber only). All three measurements were taken at the same distance from the source.

The acquired amplitude distributions for runs 30-32 are displayed in Figure 27.

In the data analysis the same thresholds and plateau limits were used for each deposit. The results are shown in Table 19.

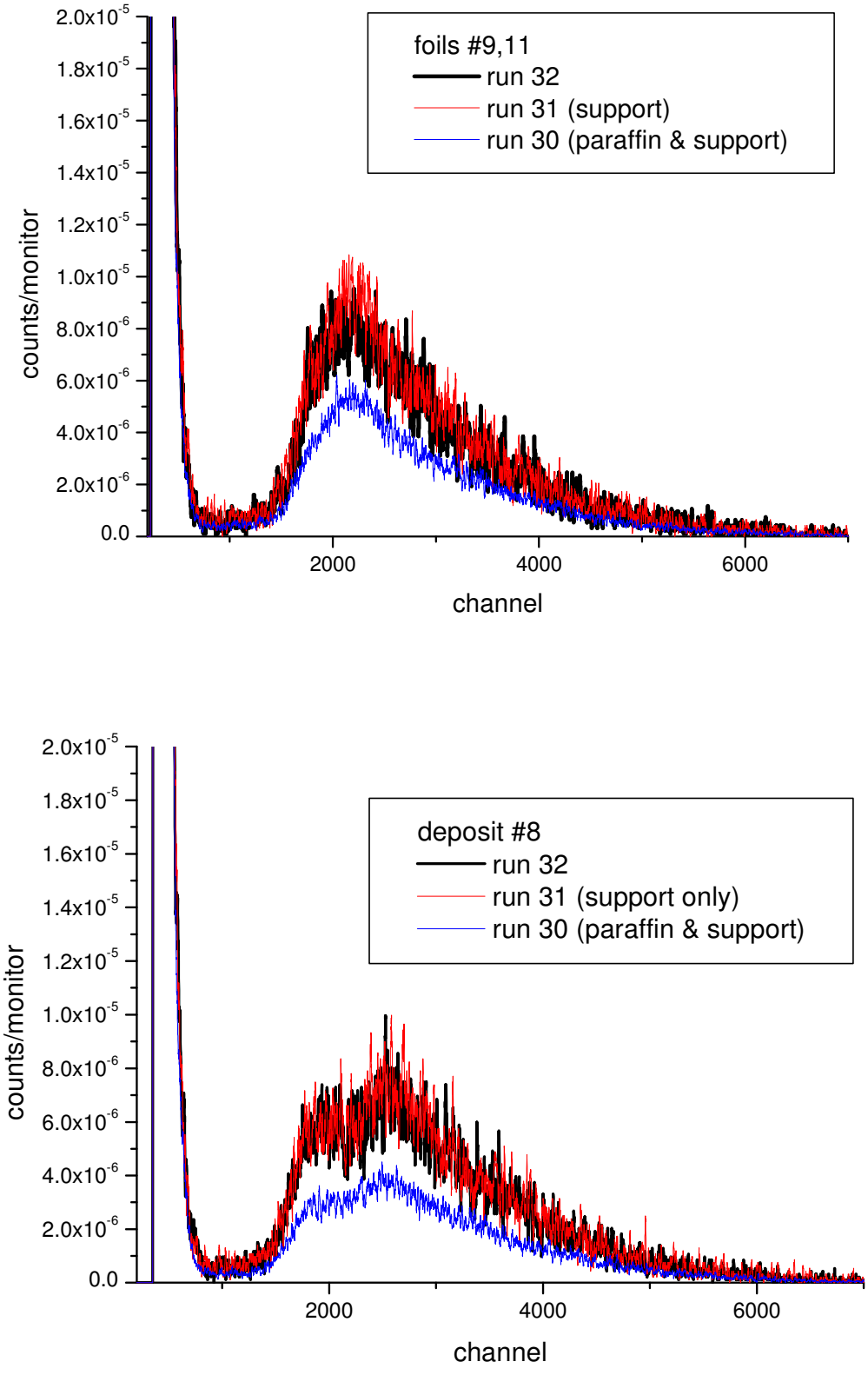

Figure 27: Amplitude distributions of foils #9,11 (top) and #8 (bottom) for the neutron background measurement runs. The spectra have been smoothed (10-point adjacent averaging) for a clearer display.

deposit	$(Y+Y_A+Y_B)$/monitor				Background
	Run 32 No shadow bar	**Run 30** Paraffin & support	**Run 31** Support only	Background only	
#9,11	$1.63(1)\cdot10^{-2}$	$1.04(1)\cdot10^{-2}$	$1.78(2)\cdot10^{-2}$	$7.42(7)\cdot10^{-3}$	45.5(6) %
#8	$2.09(2)\cdot10^{-2}$	$8.76(5)\cdot10^{-3}$	$1.70(2)\cdot10^{-2}$	$8.23(9)\cdot10^{-3}$	39.4(5) %

Table 19: Data analysis results for the neutron background measurements of FC300. The last two columns show the clean background (effect of paraffin block only) in counts per monitor and as a fraction of the measured total yield of run 32, respectively.

From the fit parameters of Tables 16, 18, the background for the conditions of run 32 can be calculated by applying the relation (neutron rate) = $P_1 + P_2/R'^2$. This was found to be 50.2(9) % for foils #9, #11 and 42(1) % for foil #8.

Considering that the current background measurement only constitutes a rough estimation, there is reasonable agreement with the values of Table 19. In any case these runs confirm the existence of a very large background component contained in the acquired FC300 data.

B. FC 200m

i) E_n=1.25 MeV measurements

The pulse height distributions and analysis results for the E_n=1.25MeV measurements of FC200 are shown in Figure 28 and Table 20 respectively.

In the case of FC200 the plateau is neither as flat nor as wide as for FC300. Nevertheless the value 0.45P is located roughly in the middle of the region between the alpha and fission peaks so it is again chosen as a threshold. The same plateau limits were used for both runs.

There are no alpha background measurements for FC200.

run	R (cm)	Peak/plateau ratio	$Y_A/(Y+Y_A)$	$(Y+Y_A+Y_B)$/monitor
1	105.2	7.62	8.7(4) %	$4.07(3)\cdot10^{-2}$
2	101.3	7.32	8.7(3) %	$4.01(2)\cdot10^{-2}$

Table 20: Data analysis results for FC200 at neutron energy 1.25 MeV. R denotes the distance between the neutron source and the centre of the chamber.

As can also be seen in Figure 28, the peak/plateau ratio is acceptable but relatively low, and a higher fraction of fission fragments is below threshold than for FC300.
These differences are anticipated because of the more complex field structure of FC200.

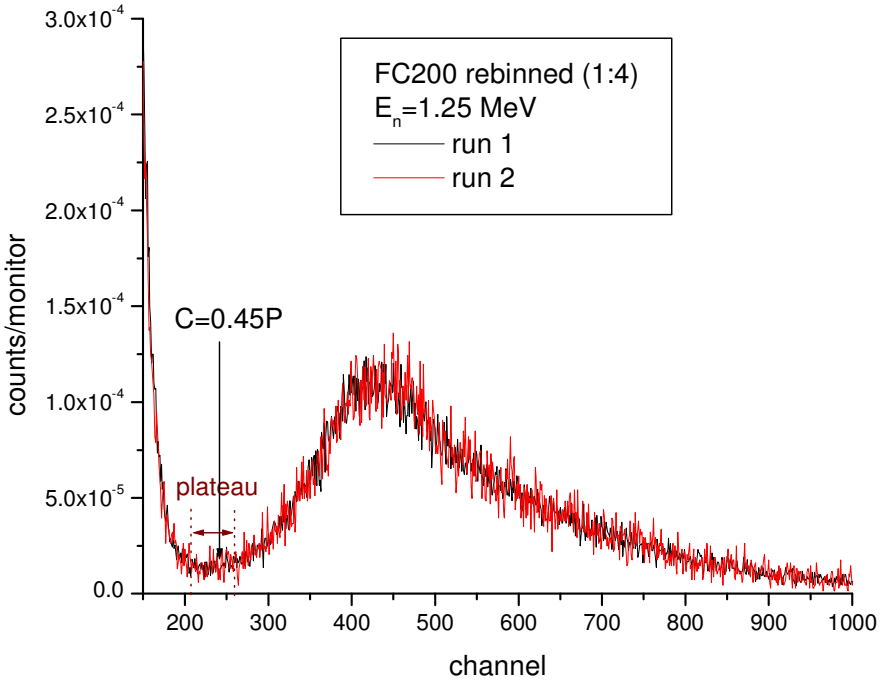

Figure 28: Rebinned (1:4) amplitude distributions of FC200 at neutron energy 1.25 MeV.

ii) Distance test

The amplitude distributions acquired with FC200 at different distances from the neutron source are shown in Figure 29.

Common plateau limits were used for all runs (except run 12, where a higher pulse height plateau was required) and the threshold was placed at channel 0.54P.
This difference between run 12 and the subsequent runs relates to the chamber being connected to different ADCs.

The data analysis results are shown in Table 21 and give an average fraction of fission fragments below threshold of 7.3(4) %.

run	R (cm)	R' (cm)	Peak/plateau	$Y_A/(Y+Y_A)$	$(Y+Y_A+Y_B)$/monitor	(neutrons/cm^2)/monitor
12	101.9	101	8.01	8.4(1) %	$5.16(7)\cdot10^{-2}$	135.7(2)
34	22.1	22.5	8.01	6.7(1) %	$4.53(8)\cdot10^{-1}$	1190(2)
35	41.4	41.6	8.26	6.6(1) %	$1.65(5)\cdot10^{-1}$	435(1)
36	61.6	61.7	7.78	7.1(2) %	$9.13(4)\cdot10^{-2}$	240(1)
39	101	101.1	6.44	7.7(4) %	$5.1(4)\cdot10^{-2}$	133(1)

Table 21: Data analysis results for the distance variation test of FC200.

Fitting the above data with the function $y= P_1 + P_2/x^2$ gives the following parameters:

P_1	**u(P_1)**	**P_2**	**u(P_2)**	**C_{12}**	**Reduced χ^2**
80.4	3.2	571141	1420	-0.6	188.7

Table 22: Fit parameters for the data of Table 21 with the function $y= P_1 + P_2/x^2$.

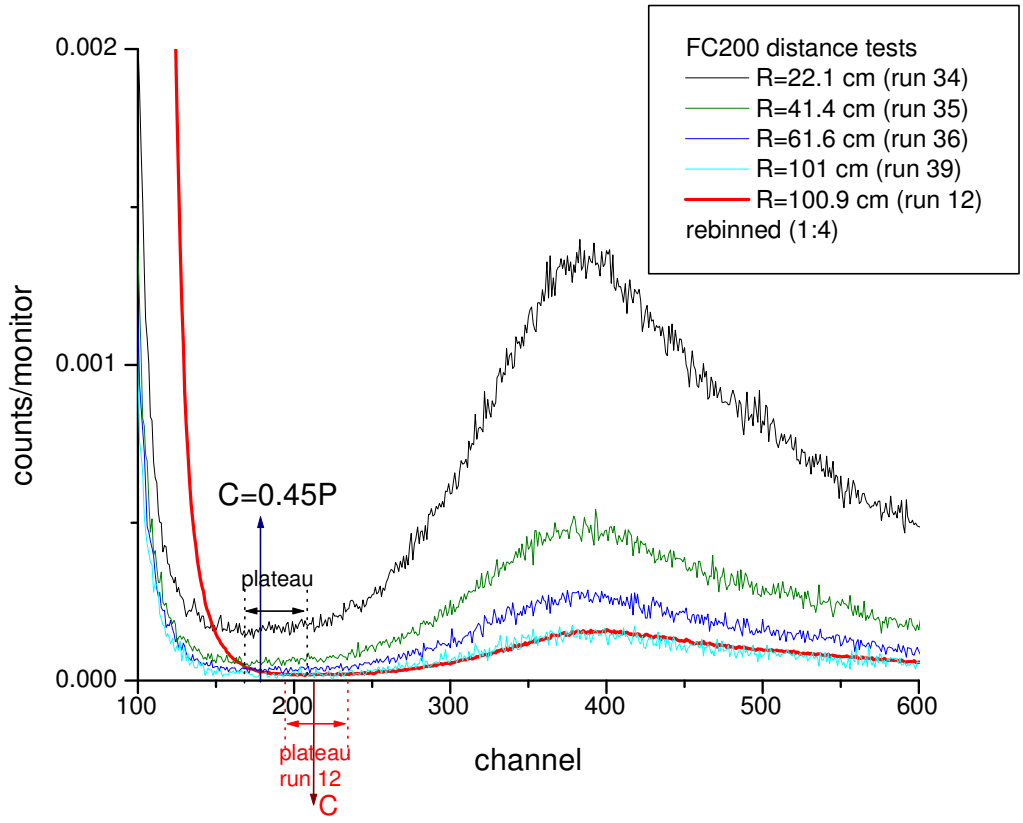

Figure 29: Rebinned (1:4) amplitude distributions of FC200 for the distance variation tests at E_n= 2.5 MeV.

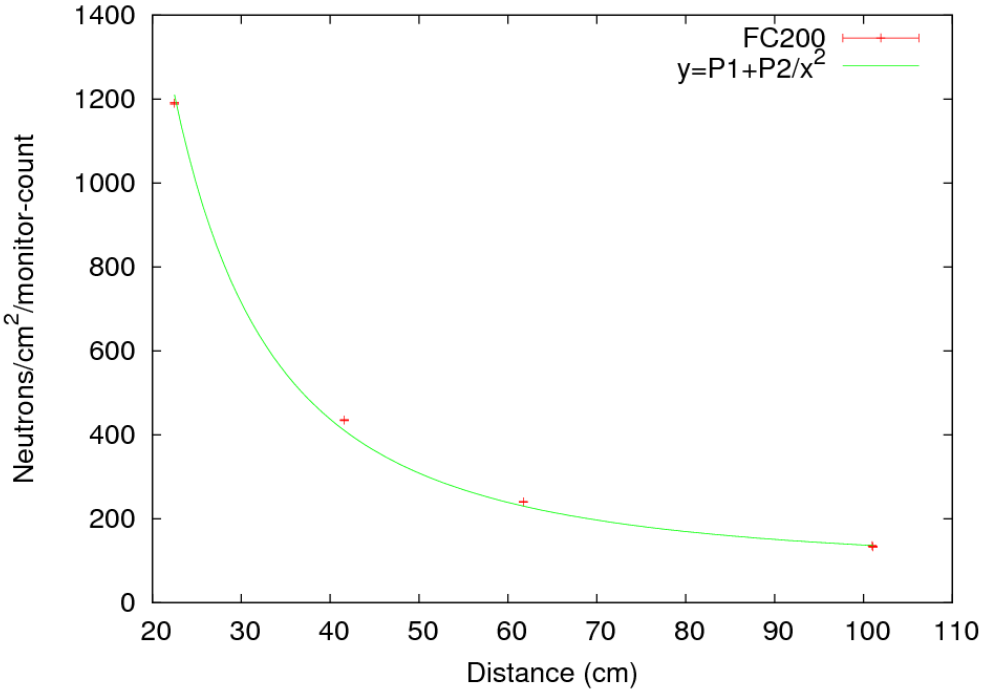

Figure 30: Measured neutron rates for FC200 with relation to the distance from the source.

/Although the obtained fit is very bad, the pattern of the large background component P_1 is repeated for FC200.

While this feature seriously restricts the reliability of all the acquired fission chamber data, it confirms that the effect is not caused by a FC300 failure, but is a systematic error and must be sought in the general experimental conditions.

The comparison with the PRT measurement gives an efficiency of 86.3% for FC200.

iii) Neutron background measurement

The shadow bar measurements (Figure 31) gave the values of Table 23.

$(Y+Y_A+Y_B)$/monitor				Background
Run 39 No shadow bar	**Run 37** Paraffin & support	**Run 38** Support only	Background only	
$5.07(4)\cdot10^{-2}$	$3.35(2)\cdot10^{-2}$	$5.68(4)\cdot10^{-2}$	$2.33(2)\cdot10^{-2}$	45.9(6) %

Table 23: Data analysis results for the neutron background measurements of FC200.

The resulting fraction of the background contained in the total fission yield compares well with the values of Table 19 (FC300).
From all three measurements, the average measured background at about 1 m from the neutron source constitutes 44(1) % of the fission spectra.

The relation (neutron rate) = $P_1 + P_2/R'^2$ with the fit parameters of Table 22 results in a much higher background of 59(3) %. Given the poor goodness of the fit, such deviation is not unexpected.

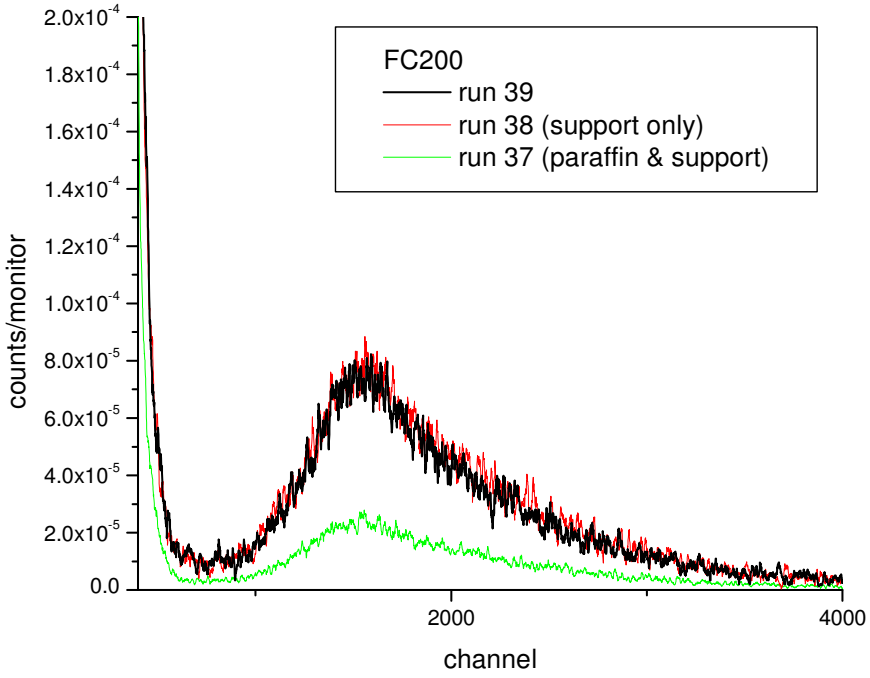

Figure 31: Amplitude distributions of FC200 for the neutron background measurement runs.

3. CONCLUSIONS

The acquired data were compromised by the existence of a large background component in the order of 45%, which is included in all the fission spectra of the tested chambers. Consequently the accuracy of the measured absolute neutron rates is questionable and no acceptable efficiency values were achieved.
The elimination of this background from the fission spectra is vital in order to obtain reliable results and the experimental methodology needs to be revised for any future efficiency measurements.

In spite of this setback, some useful conclusions can be drawn from the relative neutron rates measured during the various tests of the current experiment.

Firstly, the examination of different configurations of the UF_4 deposits and the corresponding electrodes showed that the total fission yield remains consistent with exceptional accuracy for different separation distances.
Furthermore, the #8 deposit data proved that reliable results are possible even for unequal collection distances in the configuration.

The methods for reproducing the full fission spectrum were reviewed in detail and were found to produce consistent total fission yields with remarkably small uncertainties, in the order of 0.8%. Both techniques were found to be successful also for less well-defined distributions, introducing acceptable uncertainties (<3%) even for approximate plateau limits.

Finally, in spite of the high level of background in the data, the measured neutron rates generally adhere to the $1/r^2$ rule with respect to the distance r from the neutron source.

4. REFERENCES

[1] L.-C. Mihailescu PhD thesis, IRMM publications, 2007
[2] J. C. Thiry report, IReS Strasbourg, 2008
[3] M. Stanoiu, private communication
[4] ENDF VIIB
[5] D. B. Gayther, Metrologia 27 (1990) 221-231
[6] Budtz-Jørgensen, NIM A236 (1985) 630-640

European Commission

EUR 25208 EN – Joint Research Centre – Institute for Reference Materials and Measurements
Title: Uncertainties and covariances for inelastic scattering data
Author(s): A. Plompen and A. Negret, editors
Luxembourg: Publications Office of the European Union
2011 – 126 pp. – 21.0 x 29.7 cm
EUR – Scientific and Technical Research series – ISSN 1831-9424
ISBN 978-92-79-23072-1
doi:10.2787/58803

Abstract
In the present report we collect several contributions concerning the correctness, uncertainties and covariances of data obtained with the Germanium Array for Inelastic Neutron Scattering (GAINS) which is installed at the GELINA neutron time-of-flight facility. Both inelastic scattering cross sections and uncertainties and covariances for nuclear data are of great current interest as they feature prominently in uncertainty estimates for key parameters of reactor systems [3]. It is for this reason that a task of the European Collaborative Project Accurate Nuclear Data for nuclear Energy Sustainability (ANDES) is devoted to uncertainties and covariances of inelastic scattering data obtained with GAINS. This report is written in evidence of a milestone (M1.6) of that project. It also provides evidence for a deliverable (6.04) of the work programme 2011 of Action 51402 Nuclear data for radioactive waste management and safety of new reactor developments (ND MINWASTE) of the JRC-IRMM.

The mission of the JRC is to provide customer-driven scientific and technical support for the conception, development, implementation and monitoring of EU policies. As a service of the European Commission, the JRC functions as a reference centre of science and technology for the Union. Close to the policy-making process, it serves the common interest of the Member States, while being independent of special interests, whether private or national.

LA-NA-25208-EN-N

ISBN 978-92-79-23072-1